U.S. DEPARTMENT OF COMMERCE
National Technical Information Service

PB-295 386

Further Studies of Regional Diffusion Modeling in the Northern Great Plains

Systems Applications, Inc, San Rafael, CA

Prepared for

Environmental Protection Agency, Denver, CO Region VIII

Mar 79

United States
Environmental Protection
Agency

Region 8
1860 Lincoln Street
Denver, Colorado 80295

EPA-908/1-78-005
FEBRUARY 1979
FINAL

Air

PB 295386

EPA

FURTHER STUDIES OF REGIONAL DIFFUSION MODELING IN THE NORTHERN GREAT PLAINS

REPRODUCED BY
NATIONAL TECHNICAL
INFORMATION SERVICE
U. S. DEPARTMENT OF COMMERCE
SPRINGFIELD, VA. 22161

BIBLIOGRAPHIC DATA SHEET	1. Report No. EPA-908/1-78-005	2.	3. Recipient's Accession No. PB295386
4. Title and Subtitle Further Studies of Regional Diffusion Modeling in the Northern Great Plains			5. Report Date March, 1979 6.
7. Author(s) Mei-Kao Liu, Michael Wojcik			8. Performing Organization Rept. No.
9. Performing Organization Name and Address Systems Applications, Inc 950 Northgate Drive San Rafael, CA 94903			10. Project/Task/Work Unit No. EF78-88R - EF79-40 11. Contract/Grant No. 68-01-3591
12. Sponsoring Organization Name and Address Region VIII Air Branch U.S. Environmental Protection Agency 1860 Lincoln Street Denver, CO 80295			13. Type of Report & Period Covered Final 14.

15. Supplementary Notes
See also PB-285 980/AS Development of a Regional Air Pollution Model and Its Application to the Northern Great Plains.

16. Abstracts In a previous study, a Regional Air Pollution Model was developed to simulate the effect of emissions from major point sources on air quality over long distances. This model was subsequently applied to the Northern Great Plains to assess the regional impact of existing and proposed energy developments in that area. This report continues that study by investigating methods for characterizing wind field and mixed layer diffusivity in mesoscale air quality modeling. After a review of pertinent theoretical and observational studies, the geostrophic wind and a scheme first proposed by Smagorinsky(1963) for horizontal eddy diffusivities were selected. A bicubic spline fit was used to interpolate the geopotential height data needed for implementation of this scheme. This method was used to compute the wind fields and horizontal diffusivities for the three time periods studied in the previous efforts, and the Regional Air Pollution Model was subsequently exercised using the new meteorological data.

17. Key Words and Document Analysis. 17a. Descriptors
Atmospheric diffusion
Air pollution
Mathematical models
Atmospheric models
Sulfates
Geostrophic wind
Coal deposits - exploitation

17b. Identifiers/Open-Ended Terms
Path of pollutants
Northern Great Plains Region (United States)
Regional Air Pollution Study
Low sulfur coal

17c. COSATI Field/Group

18. Availability Statement	19. Security Class (This Report)	21. No. of Pages
Distribution unlimited.	UNCLASSIFIED	125
	20. Security Class (This Page) UNCLASSIFIED	22. Price A06 MF A01

FORM NTIS-35 (REV. 10-73) ENDORSED BY ANSI AND UNESCO. THIS FORM MAY BE REPRODUCED USCOMM-DC 8265-P74

EPA-908/1-78-005

Final Report

FURTHER STUDIES OF REGIONAL DIFFUSION MODELING IN THE NORTHERN GREAT PLAINS

by

Mei-Kao Liu
Michael Wojcik

Systems Applications, Incorporated
950 Northgate Drive
San Rafael, California 94903

Contract No. 68-01-3591

EF78-88R - EF79-40

March 1979

Prepared for

Donald Henderson
Project Officer

Environmental Protection Agency
Region VIII
1860 Lincoln Street
Denver, Colorado 80295

DISCLAIMER

This report has been reviewed by the U.S. Environmental Protection Agency, Region VIII, and approved for publication. Mention of trade names or commercial products does not constitute endorsement or recommendation for use.

This document is available to the public through the National Technical Information Service, Springfield, Virginia 22151.

ABSTRACT

This report describes the continuation of a project devoted to the assessment of air quality impacts on a regional scale. In the previous study, a Regional Air Pollution Model was developed and a series of numerical experiments were carried out to test the sensitivity of the model (Liu and Durran, 1977). The sensitivity studies showed that wind distribution and horizontal eddy diffusivities in the mixed layer are critical meteorological parameters.

Further work on improving the processing of meteorological data for the Regional Air Pollution Model indicated that the geostrophic wind relationship provides the most appropriate basis for calculating the wind field in the mixed layer. Implementing this relationship required construction of the geopotential height field. The best method tested for constructing this height field is a bicubic spline fit of geopotential height data. For the horizontal eddy diffusivities, a parameterization scheme first proposed by Smagorinsky (1963) was selected after an extensive literature review. In that scheme the horizontal diffusivity is assumed to be proportional to the magnitude of velocity deformation.

The Regional Air Pollution Model was then exercised for the Northern Great Plains using the new methodology for processing meteorological data. The simulation impacts of SO_2 emissions from existing and proposed energy developments were compared with the results from earlier work. Although the conclusions of the original report concerning maximum concentrations remain essentially unaltered, significant change was observed in the configurations of the computed concentration isopleth. The weak-wind spring scenario still produced the highest SO_2 and sulfate concentrations. For estimated 1986 SO_2 emissions, three-hour-average SO_2 concentrations were as high as 100 $\mu g\ m^{-3}$ near large point sources but rarely exceeded

8 $\mu g\ m^{-3}$ 100 kilometers downwind. The sensitivity of calculated sulfate concentrations to SO_2-to-sulfate conversion rates was also tested in the present study. A low conversion rate (0.3 percent per hour) generated negligible sulfate concentrations even for the worst case. However, a 1 percent per hour conversion rate produced moderate sulfate buildup, with concentrations reaching 6 $\mu g\ m^{-3}$, a level that has been considered as marginal in causing visibility reduction (Trijonis and Yuan, 1978; Charlson, Waggoner, and Thielke, 1979).

CONTENTS

DISCLAIMER ii

ABSTRACT iii

LIST OF ILLUSTRATIONS vi

LIST OF TABLES xii

I INTRODUCTION 1

II SUMMARY AND CONCLUSIONS 3

III A REVIEW OF MESOSCALE TRANSPORT AND DIFFUSION 5

A. Review of Pertinent Studies 5

B. Parameterization of Horizontal Eddy Diffusivity 12

IV CHARACTERIZATION OF MESOSCALE TRANSPORT AND DIFFUSION 14

A. Bilinear Interpolation 15

B. Fitting of the Poisson Equation 17

C. Bicubic Spline Fit 27

V SENSITIVITY OF THE TRANSPORT AND DIFFUSION CHARACTERIZATION SCHEME 35

VI ANALYSIS OF THE RESULTS 49

A. Analysis of the Effect of the New Characterization Scheme 62

B. Air Quality Analysis 63

1. Spring Scenario 63
2. Winter Scenario 63
3. Summer Scenario 66

C. Sensitivity Study of the SO_2/SO_4 Conversion Rate 66

APPENDIX: SIMULATION RESULTS 72

REFERENCES 110

ILLUSTRATIONS

1	Energy Spectrum for Atmospheric Flows	6
2	Empirical Relationship for Horizontal Plume Spread on the Mesoscale	8
3	The Development of Clusters Initially of the Form ABCDEF at Each Level to Clusters A'B'C'D'E'F' 18 Hours Later	11
4	850-mb Weather Map for 1700 MST on 30 January 1976	16
5	Bilinearly Interpolated Geopotential Height Field (m)	18
6	Zonal Wind Field Generated from Bilinearly Interpolated Geopotential Height Data (m sec^{-1})	19
7	Meridional Wind Field Generated from Bilinearly Interpolated Geopotential Height Data (m sec^{-1})	20
8	Geopotential Height Field (m) Based on the Solution of the Laplace Equation After 25 Iterations	22
9	Geopotential Height Field (m) Based on the Solution of the Laplace Equation After 125 Iterations	23
10	Geopotential Height Field (m) Based on the Solution of the Laplace Equation After 150 Iterations	24
11	Zonal Wind Field (m sec^{-1}) Generated from Geopotential Heights Based on the Solution of the Laplace Equation After 150 Iterations	25
12	Meridional Wind Field (m sec^{-1}) Generated from Geopotential Heights Based on the Solution of the Laplace Equation After 150 Iterations	26
13	Geopotential Height Field (m) Based on the Solution of the Poisson Equation with Prescribed Forcing Functions	28
14	Bicubic Spline Fit of Geopotential Height Data (m)	31
15	Zonal Wind Field (m sec^{-1}) Generated by a Bicubic Spline Fit of Geopotential Height Data	32
16	Meridional Wind Field (m sec^{-1}) Generated by a Bicubic Spline Fit of Geopotential Height Data	33

17 Wind Vectors Generated by a Bicubic Spline Fit of Geopotential Height Data 34

18 850-mb Weather Map for 500 MST on 27 January 1976 36

19 850-mb Weather Map for 1700 MST on 28 January 1976 37

20 850-mb Weather Map for 500 MST on 30 January 1976 38

21 Bicubic Spline Fit of Geopotential Height Data (m) for 500 MST on 27 January 1976 39

22 Bicubic Spline Fit of Geopotential Height Data (m) for 1700 MST on 28 January 1976 40

23 Bicubic Spline Fit of Geopotential Height Data (m) for 500 MST on 30 January 1976 41

24 Wind Vectors Generated by a Bicubic Spline Fit of Geopotential Height Data for 500 MST on 27 January 1976 42

25 The Computed Horizontal Eddy Diffusivity (in 10^4 m^2 sec^{-1}) for 500 MST on 27 January 1976 43

26 Wind Vectors Generated by a Bicubic Spline Fit of Geopotential Height Data for 1700 MST on 28 January 1976 44

27 The Computed Horizontal Eddy Diffusivity (in 10^4 m^2 sec^{-1}) for 1700 MST on 28 January 1976 45

28 Wind Vectors Generated by a Bicubic Spline Fit of Geopotential Height Data for 500 MST on 30 January 1976 46

29 The Computed Horizontal Eddy Diffusivity (in 10^4 m^2 sec^{-1}) for 500 MST on 30 January 1976 47

30 Wind Vectors Generated by a Bicubic Spline Fit of Geopotential Height Data for 1700 MST on 4 April 1976 50

31 Wind Vectors Generated by a Bicubic Spline Fit of Geopotential Height Data for 1700 MST on 5 April 1976 51

32 Wind Vectors Generated by a Bicubic Spline Fit of Geopotential Height Data for 1700 MST on 6 April 1976 52

33 Wind Vectors Generated by a Bicubic Spline Fit of Geopotential Height Data for 500 MST on 9 July 1975 53

34 Wind Vectors Generated by a Bicubic Spline Fit of Geopotential Height Data for 500 MST on 10 July 1975 54

35 Wind Vectors Generated by a Bicubic Spline Fit of Geopotential Height Data for 500 MST on 11 July 1975 55

36 Comparison of SO_2 Concentration Fields ($\mu g\ m^{-3}$) for Case 1: 500 to 800 MST on 5 April 1976 56

37 Comparison of SO_2 Concentration Fields ($\mu g\ m^{-3}$) for Case 1: 1700 to 2000 MST on 5 April 1976 57

38 Comparison of SO_2 Concentration Fields ($\mu g\ m^{-3}$) for Case 1: 800 to 1100 MST on 6 April 1976 58

39 Comparison of SO_2 Concentration Fields ($\mu g\ m^{-3}$) for Case 2: 500 to 800 MST on 5 April 1976 59

40 Comparison of SO_2 Concentration Fields ($\mu g\ m^{-3}$) for Case 2: 1700 to 2000 MST on 5 April 1976 60

41 Comparison of SO_2 Concentration Fields ($\mu g\ m^{-3}$) for Case 2: 800 to 1100 MST on 6 April 1976 61

42 SO_2 Concentration Fields ($\mu g\ m^{-3}$) for Case 5 (Revised Scheme): 1700 to 2000 MST on 27 January 1976 64

43 SO_2 Concentration Fields ($\mu g\ m^{-3}$) for Case 5 (Revised Scheme): 2000 to 2300 MST on 28 January 1976 64

44 SO_2 Concentration Fields ($\mu g\ m^{-3}$) for Case 5 (Revised Scheme): 1400 to 1700 MST on 29 January 1976 65

45 SO_2 Concentration Fields ($\mu g\ m^{-3}$) for Case 6 (Revised Scheme): 200 to 500 MST on 10 July 1975 67

46 SO_2 Concentration Fields ($\mu g\ m^{-3}$) for Case 6 (Revised Scheme): 500 to 800 MST on 11 July 1975 67

47 SO_2 Concentration Fields ($\mu g\ m^{-3}$) for Case 6 (Revised Scheme): 1400 to 1700 MST on 11 July 1975 68

48 Concentration Fields ($\mu g\ m^{-3}$) for Case 3 (Revised Scheme): 800 to 1100 MST on 6 April 1976 69

49 Concentration Fields ($\mu g\ m^{-3}$) for Case 4 (Revised Scheme): 800 to 1100 MST on 6 April 1976 71

A-1 SO_2 and SO_4 Concentrations for Case 1: 1700 to 2000 MST on 4 April 1976 74

A-2 SO_2 and SO_4 Concentrations for Case 1: 200 to 500 MST on 5 April 1976 75

A-3 SO_2 and SO_4 Concentrations for Case 1: 1100 to 1400 MST on 5 April 1976 76

A-4 SO_2 and SO_4 Concentrations for Case 1: 2000 to 2300 MST on 5 April 1976 77

A-5 SO_2 and SO_4 Concentrations for Case 1: 500 to 800 MST on 6 April 1976 78

A-6 SO_2 and SO_4 Concentrations for Case 1: 1400 to 1700 MST on 6 April 1976 79

A-7 SO_2 and SO_4 Concentrations for Case 2: 1700 to 2000 MST on 4 April 1976 80

A-8 SO_2 and SO_4 Concentrations for Case 2: 200 to 500 MST on 5 April 1976 81

A-9 SO_2 and SO_4 Concentrations for Case 2: 1100 to 1400 MST on 5 April 1976 82

A-10 SO_2 and SO_4 Concentrations for Case 2: 2000 to 2300 MST on 5 April 1976 83

A-11 SO_2 and SO_4 Concentrations for Case 2: 500 to 800 MST on 6 April 1976 84

A-12 SO_2 and SO_4 Concentrations for Case 2: 1400 to 1700 MST on 6 April 1976 85

A-13 SO_2 and SO_4 Concentrations for Case 3: 1700 to 2000 MST on 4 April 1976 86

A-14 SO_2 and SO_4 Concentrations for Case 3: 200 to 500 MST on 5 April 1976 87

A-15 SO_2 and SO_4 Concentrations for Case 3: 1100 to 1400 MST on 5 April 1976 88

A-16 SO_2 and SO_4 Concentrations for Case 3: 2000 to 2300 MST on 5 April 1976 89

A-17 SO_2 and SO_4 Concentrations for Case 3: 500 to 800 MST on 6 April 1976 90

A-18 SO_2 and SO_4 Concentrations for Case 3: 1400 to 1700 MST on 6 April 1976 91

A-19 SO_2 and SO_4 Concentrations for Case 4: 1700 to 2000 MST on 4 April 1976 92

A-20 SO_2 and SO_4 Concentrations for Case 4: 200 to 500 MST on 5 April 1976 93

A-21 SO_2 and SO_4 Concentrations for Case 4: 1100 to 1400 MST on 5 April 1976 94

A-22 SO_2 and SO_4 Concentrations for Case 4: 2000 to 2300 MST on 5 April 1976 95

A-23 SO_2 and SO_4 Concentrations for Case 4: 500 to 800 MST on 6 April 1976 96

A-24 SO_2 and SO_4 Concentrations for Case 4: 1400 to 1700 MST on 6 April 1976 97

A-25 SO_2 and SO_4 Concentrations for Case 5: 1700 to 2000 MST on 27 January 1976 98

A-26 SO_2 and SO_4 Concentrations for Case 5: 200 to 500 MST on 28 January 1976 99

A-27 SO_2 and SO_4 Concentrations for Case 5: 1100 to 1400 MST on 28 January 1976 100

A-28 SO_2 and SO_4 Concentrations for Case 5: 2000 to 2300 MST on 28 January 1976 101

A-29 SO_2 and SO_4 Concentrations for Case 5: 500 to 800 MST on 29 January 1976 102

A-30 SO_2 and SO_4 Concentrations for Case 5: 1400 to 1700 MST on 29 January 1976 103

A-31 SO_2 and SO_4 Concentrations for Case 6: 1700 to 2000 MST on 9 July 1975 104

A-32 SO_2 and SO_4 Concentrations for Case 6: 200 to 500 MST on 10 July 1975 105

A-33 SO_2 and SO_4 Concentrations for Case 6: 1100 to 1400 MST on 10 July 1975 106

A-34 SO_2 and SO_4 Concentrations for Case 6: 2000 to 2300 MST on 10 July 1975 107

A-35 SO_2 and SO_4 Concentrations for Case 6: 500 to 800 MST on 11 July 1975 108

A-36 SO_2 and SO_4 Concentrations for Case 6: 1400 to 1700 MST on 11 July 1975 109

TABLES

1 850-mb Geopotential Height Data for 1700 MST on 30 January 1976 17

2 List of the Computer Simulations 49

I INTRODUCTION

In a previous study, under Contract 68-01-3591 with the U.S. Environmental Protection Agency (EPA), a Regional Air Pollution Model was developed to simulate the effect of emissions from major point sources on air quality over long distances (Liu and Durran, 1977). This model was subsequently applied to the Northern Great Plains to assess the regional impact of existing and proposed energy developments in that area. A series of numerical experiments were also carried out to test the sensitivity of the model. It was found that the wind field and horizontal eddy diffusivities in the mixed layer are not only two of the most critical parameters in the model, but also the most difficult to characterize quantitatively. A decision was thus made to extend the scope of work to include an investigation of the best method for characterizing the wind field and diffusivities in the mixed layer.

In the Regional Air Pollution Model, provisions have also been made to treat the first-order reaction between SO_2 and sulfate. When an estimated 0.3 percent per hour conversion rate for SO_2 to sulfate was used, the predicted sulfate concentrations were found to be on the order of a few micrograms per cubic meter--not significantly above the background levels. Recent studies, however, appear to indicate that sulfate concentrations on the order of 10 $\mu g\ m^{-3}$ may significantly affect visibility (Trijonis and Yuan, 1978; Charlson, Waggoner, and Thielke, 1979). Thus, a set of calculations using a realistic but higher value for the rate of conversion of SO_2 to sulfate was in order.

This report delineates the work completed under the extension of this contract. Chapter II presents a brief summary and the conclusions drawn from this study. Chapter III reviews previous studies on mesoscale horizontal eddy diffusivity, and Chapter IV describes a methodology for characterizing the mesoscale transport and diffusion. Chapter V discusses the

sensitivity of the Regional Air Pollution Model predictions to the proposed methodology. Finally, Chapter VI analyzes the air quality impact predicted on the basis of the new set of model calculations.

II SUMMARY AND CONCLUSIONS

In this study, methods for characterizing wind flow and horizontal diffusion in mesoscale air quality modeling were examined. After a review of pertinent theoretical and observational studies, the geostrophic wind and a scheme first proposed by Smagorinsky (1963) for horizontal eddy diffusivities were selected. A bicubic spline fit was used to interpolate the geopotential height data needed for implementation of this scheme. This method was used to compute the wind fields and horizontal diffusivities for the three time periods studied in the previous efforts, and the Regional Air Pollution Model was subsequently exercised using the new meteorological data.

The shapes of the new concentration isopleths for both SO_2 and sulfate differ considerably from those of the original simulation. The differences are due primarily to the implementation of a smooth geostrophic wind field in the mixing layer instead of the straightforward interpolation of the wind in the previous study. The new prescription for horizontal diffusivity and more realistic mixing heights also account for some of the differences observed.

Despite these differences, however, the original conclusions remain essentially unaltered. A scenario representative of the winter, characterized by low mixing depths and high winds, still produced the lowest concentrations. The mixing depths for the summer scenario are approximately twice as high as in the spring scenario, combined with considerably weaker winds, leading to moderate levels of pollutant concentrations. According to the computer simulations, the spring scenario, characterized by low winds and medium mixing depths, represents the worst case of the three scenarios for regional impact. Maximum three-hour SO_2 concentrations for this case were found to be on the order of 100 $\mu g\ m^{-3}$ using the 1986 emissions.

Assuming a 1 percent per hour SO_2-to-sulfate conversion rate, the maximum computed sulfate concentrations are 6 $\mu g\ m^{-3}$, a level that has been considered as marginal in affecting visibility degradation.

III A REVIEW OF MESOSCALE TRANSPORT AND DIFFUSION

To select and adapt an appropriate scheme for characterizing mesoscale atmospheric motions and diffusion, the study team first reviewed the pertinent theoretical and observational studies. This review is summarized below, followed by a description of the scheme selected for the present project.

A. REVIEW OF PERTINENT STUDIES

As shown in Figure 1, which presents the characteristics of the energy spectrum, atmospheric motion covers a wide spectrum of phenomena, ranging from the smallest scales associated with viscous dissipation to planetary waves. The transport and dispersion of pollutants thus strongly depends on its length scale in relation to the scales of turbulent motion or the eddy size. Eddies much larger than the pollutant scale will transport it as a whole, whereas eddies of the same size will deform it through wind shear across the cloud, and eddies smaller than the cloud will disperse it. The turbulent energy is primarily concentrated in large-scale air motion. As a pollutant cloud disperses, its size increases, and therefore, the turbulent motion that is of the same scale increases in energy. The manner in which a cloud of pollutants interacts with eddies of equal and different scale greatly affects the value of the horizontal eddy diffusivity.

Randerson (1972) analyzed the dispersion of a single nuclear debris cloud and plotted its horizontal width σ_y as a function of travel time t. He then calculated the horizontal eddy diffusivity, K_H, according to the simple formula discussed by Taylor (1921):

$$K_H = \frac{\sigma_y^2}{2t} \quad .$$

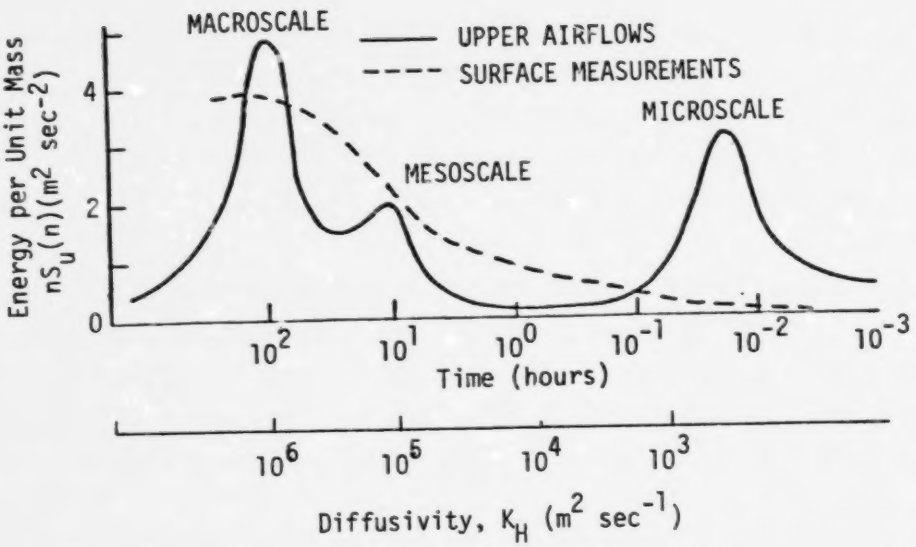

Sources: Murgatroyd (1969) for upper airflows.
van der Hoven (1957) for surface measurements.

FIGURE 1. ENERGY SPECTRUM FOR ATMOSPHERIC FLOWS

Randerson's results are representative of observed mesoscale K_H values presented in a survey by Bauer (1973). Together with an upper and lower bound proposed by Hage et al. (1966), the results of Randerson's observations are presented in Figure 2. All of the observational studies surveyed found three distinct stages of dispersion. For travel times less than 1 hour and greater than 10 to 12 hours, K_H was approximately constant. Diffusion accelerated during the intermediate travel time, which is the range of interest in regional-scale studies. Horizontal diffusivity was found to vary from 10^3 to 10^5 m^2 sec^{-1} with $K_H \propto \sigma_y^{1.17\pm0.05}$. As Figure 2 suggests, K_H can vary by a factor of 10 from Randerson's values at a given travel time.

The observational studies indicated that horizontal diffusivity varies greatly and exhibits a definite scale dependence. However, the rate of diffusion is not explained entirely by its scale dependence; there is also variability in K_H at a given travel time, indicating that atmospheric conditions play an important part in diffusion.

Diffusion can also be studied by analyzing the trajectory of hypothetical particles in a given flow field. Either a series of particles can be released from a fixed point at set time intervals, or a cluster of particles can be released at the same time. The second approach is most similar to pollutant dispersion. Statistical analysis of particle velocities and separation distances can reveal the characteristics of large-scale diffusion. The Lagrangian reference frame of trajectory studies is the center of mass of the particle. Mesoscale models divide the region of interest into cells and then examine dispersion with respect to the cell from a Eulerian reference frame.

How applicable are Lagrangian studies to Eulerian models? In a comparison of Lagrangian and Eulerian statistics, Kao and Bullock (1964) analyzed the dispersion of the endpoints of particles initiated at regular intervals at a fixed point at the 500 mb-level. The velocity fluctuations with time with respect to the center of mass along each trajectory were computed. The fluctuations along one trajectory were connected with those of the others to form a long time series. The same statistical analysis was carried out at a fixed point, and the Lagrangian

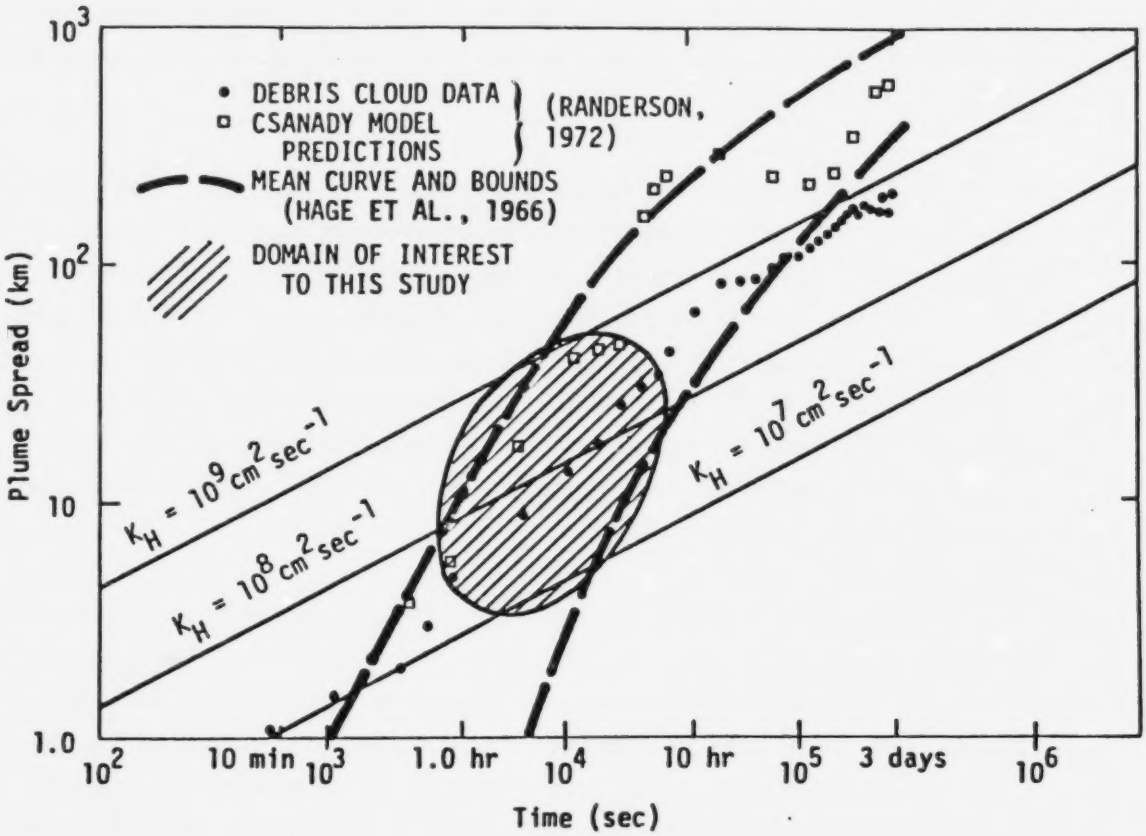

Source: Randerson (1972).

FIGURE 2. EMPIRICAL RELATIONSHIP FOR HORIZONTAL PLUME SPREAD ON THE MESOSCALE

and Eulerian energy spectra were then computed and were found to have identical statistics. As in Figure 1, turbulent energy was concentrated in large-scale motions, with the Eulerian energy peak at a slightly larger scale. The ratio of Lagrangian to Eulerian time scales was comparable. Although the study was carried out for the mid-troposphere, motions at all levels are interconnected and similar. Thus, the results indicate that characteristics of diffusivity found in Lagrangian studies are applicable to Eulerian models.

Kao (1968) examined the statistical theory of particle dispersion. Working with a cluster of particles, he derived the equations governing the motion of particles relative to their center of mass, since this relative motion determines how particles disperse. He then related mean square relative separation to travel time and derived relations for large and small time. In the initial stage, diffusion is affected by turbulent motions of all scales. At larger travel times, dispersion of particles is primarily affected by turbulent motions of similar scales. Diffusion becomes constant at large times.

Using one year of data, Kao and Gain (1968) plotted the trajectories of a cluster of particles for travel times of 196 hours. The clusters were all released from the same point at three levels: 200, 500, and 850 mb. The power spectra and mean square separation distance for the zonal and meridional components were obtained, and yearly and seasonal results were analyzed. Only the 850-mb results are discussed here. The energy was found to be concentrated in the large-scale eddies with a greater maximum in the zonal component. The rate of dispersion increased with the size of the particle cluster, indicating that eddies of the same size as the cluster have the greatest impact on their dispersion. A seasonal variability in mean square separation distance showed that separation was greatest in the winter and smallest in the summer. The zonal component of mean square separation distance was found to be twice the meridional component.

Murgatroyd (1969) conducted an experiment on the dispersion of a cluster of particles of various sizes at the 300-, 700-, and 900-mb levels over an 18-hour period. The initial sizes and shapes of the various clusters, as well as their shapes 18 hours later, are shown in Figure 3. The clusters ranged in size from 100 to 1600 km in diameter. At the 900-mb level, deformation was the predominant means of dispersion for clusters of all sizes. Deformation, which is caused by eddies of the same scales as the cluster, increases with cluster size. Eddies of the same scale increase in energy with size. Murgatroyd derived a simple relation between relative cluster separation and deformation assuming that the velocity field was predominantly deformed. Using his results for cluster separation, he was able to reproduce the deformation field of the 900-mb level.

Kao and Henderson (1970) examined the importance of the shape of the wind field and dispersion at the 500-mb level. Clusters of particles were released at various positions in the wind field during the summer and winter. The shape of the wind field was found to influence diffusion strongly. Horizontal diffusivity was greatest near the jet stream, where shear was the strongest. Dispersion was the weakest near the center of a high, where the flow is weak and uniform. The zonal horizontal diffusivity was at times an order of magnitude greater than meridional diffusivity.

In summary, observations indicate that diffusion is strongly scale dependent; horizontal eddy diffusivity increases with the scale of interest in the horizontal direction. A review of observational data also reveals that horizontal diffusivity can vary by an order of magnitude at a given length scale; on a regional scale it ranges in value from 10^3 to 10^5 m^2 sec^{-1}. Further studies show that the shape of the flow field greatly affects horizontal diffusivity and that diffusion is greater under strong shear conditions.

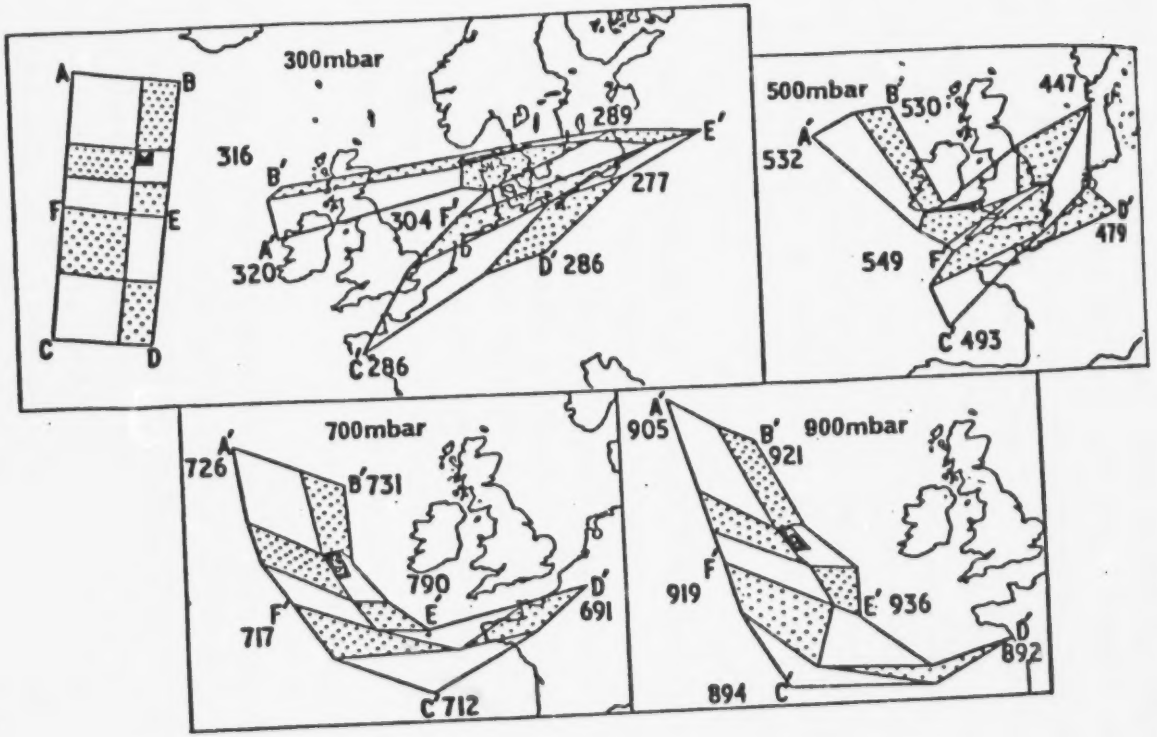

Source: Murgatroyd (1969).

FIGURE 3. THE DEVELOPMENT OF CLUSTERS INITIALLY OF THE FORM ABCDEF AT EACH LEVEL TO CLUSTERS A'B'C'D'E'F' 18 HOURS LATER

B. PARAMETERIZATION OF HORIZONTAL EDDY DIFFUSIVITY

Horizontal diffusivity predominantly depends on the length of scale and the strength of the shear of the wind flow. Although zonal diffusion is greater than meridional diffusion, diffusivity can be correlated with travel time or with length scale. Both approaches have been attempted. For example, by parameterizing cloud width as a function of an initial width and travel time, Walton (1973) was able to reproduce Randerson's data. This approach would have to be developed further to include the effect of wind shear. In contrast, Murgatroyd related cloud width directly to deformation, and he obtained good results. Smagorinsky (1963) parameterized horizontal diffusivity in terms of deformation in his general circulation model.

Statistical theory shows that after the initial stage, horizontal diffusion is affected most by eddies of the same scale. Turbulent energy, as revealed in statistical studies, is concentrated in large-scale motion. Combining the two results, we can conclude that the increase in horizontal diffusion with scale is due to the increase in turbulent energy with scale and that deformation is the primary form of diffusion.

Murgatroyd's work further exemplifies the importance of deformation beyond the initial diffusion stage. Therefore, the shape of the flow field, and in particular the amount of shear present, must be considered in determining horizontal diffusivity. In general, zonal shear is greater than meridional shear, and zonal diffusion is greater than meridional diffusion.

The observational and statistical studies summarized above show that the horizontal eddy diffusivity K_H is scale and shear dependent. To evaluate K_H realistically, one must take both of these effects into account. The theoretical framework of the present investigation is based on a treatise on numerical simulation of the atmospheric circulation by Smagorinsky (1963), who showed that nonlinear lateral diffusion can be

formulated on the basis of the Heisenberg (1948) similarity theory for turbulence in the equilibrium range. If this theory is applicable to the scale of interest to the present study, the following formula for the horizontal eddy diffusivity coefficient can be derived (assuming that density variations can be ignored):

$$K_H = \frac{5}{4} \cdot (\alpha\Delta)^2 \cdot |\mathrm{Def}| \quad ,$$

where Δ is the grid spacing and $|\mathrm{Def}|$ is the magnitude of the velocity deformation,

$$|\mathrm{Def}| = \left[\left(\frac{\partial v}{\partial x} + \frac{\partial u}{\partial y}\right)^2 + \left(\frac{\partial u}{\partial x} - \frac{\partial v}{\partial y}\right)^2\right]^{1/2} \quad .$$

The empirical coefficient, $\alpha \approx 0.28$, in this scheme was estimated from global-scale modeling studies.

In this study, this parameterization was applied to the Great Plains region and tested under various flow pattern conditions, adjusting the scheme for this application as necessary. The horizontal diffusion algorithm described above was then incorporated in the Regional Air Pollution Model.

IV CHARACTERIZATION OF MESOSCALE TRANSPORT AND DIFFUSION

To evaluate horizontal eddy diffusivity using the parameterization scheme suggested in the previous chapter, one must have a realistically smooth and continuous wind velocity field. Since only a limited number of data points are available, the generation of winds for all cells in a 120 x 100 grid model requires some form of interpolation. If the interpolation scheme allows discontinuities to exist in the field, subsequent discrepancies in the values of horizontal diffusivity will result.

In air quality modeling studies, wind data are normally collected and used to interpolate a wind field. But since the horizontal component of the wind is a two-dimensional vector, it is difficult to find an interpolation scheme that generates a field that is satisfactorily smooth. However, the components of the wind can be calculated from the gradient of geopotential height, Z, on a constant pressure surface using the geostrophic wind relationship:

$$u = -\frac{g}{f}\left(\frac{\partial Z}{\partial y}\right)_p \quad ,$$

$$v = \frac{g}{f}\left(\frac{\partial Z}{\partial x}\right)_p \quad ,$$

where g is the gravitational constant and f is the Coriolis parameter. Geopotential height fields are readily available from weather maps published by the National Weather Service.

Geopotential height is a scalar quantity. Therefore, in working with such height data, one needs to smooth only one field instead of the two components of the wind. Assuming that one can find a method that generates a smooth and continuous geopotential height field, the wind field resulting from the

geostrophic relations should also be smooth and continuous. The geopotential height interpolation techniques examined in this study are described below.

As shown in Figure 4, the test case used to study geopotential height interpolation methods consists of an 850-mb pressure contour map over a portion of the Northern Great Plains, with all of the calculated values for 1700 MST on 30 January 1976. This choice was based primarily on the convenience of available data for that example. The origin of the coordinates is in the lower left corner of the grid. The first contour on the left side of the grid has a geopotential height value of 1560 m, and geopotential height decreases toward the upper right-hand corner, where the contour line with the smallest value, 1380 m, is located. The dashed lines show the constant temperature contours. The geopotential height values extracted manually from the map and their location on the grid are shown in Table 1. From the 42 data points, a geopotential height field of 12,000 points was generated.

A. BILINEAR INTERPOLATION

The simplest interpolation scheme that can be used is bilinear interpolation. Values at each grid point were found by linearly interpolating a value for the point from data points in both the east-west and north-south directions and then equally weighing the resulting values to obtain a single solution. As shown in Figure 5, the resultant 850-mb height field exhibits a general shape similar to that in Figure 4. The effect of linear fitting between data points is also quite visible.

The zonal, u, and meridional, v, velocity components were computed using this height field, and the results shown in Figures 6 and 7 were obtained. Although the winds obtained generally have the proper direction and magnitude, sharp discontinuities appear near data points, and the contour lines have a physically unrealistic rectangular shape owing to the nature of bilinear interpolation. Thus, this technique was not suitable for the present project.

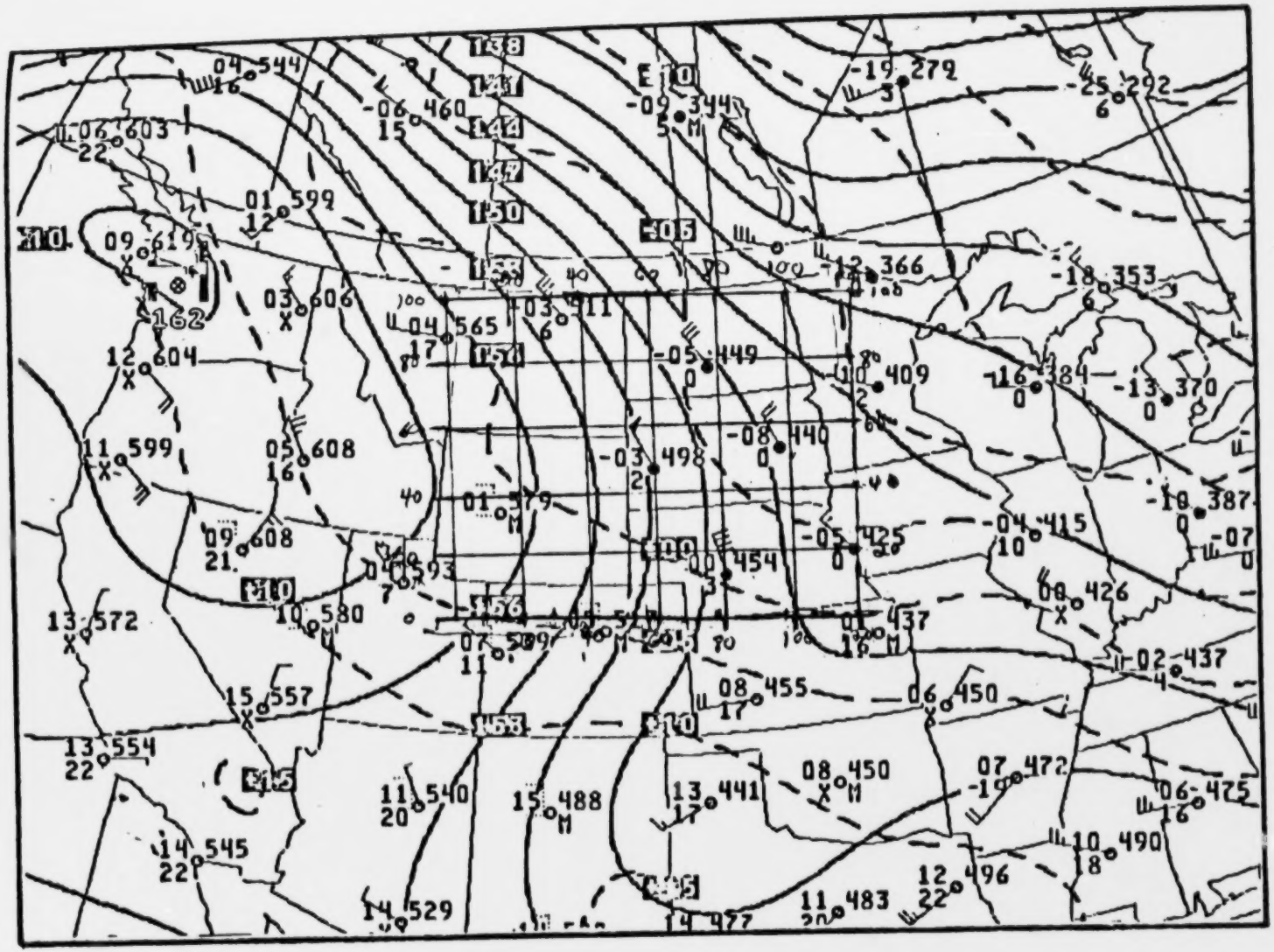

FIGURE 4. 850-mb WEATHER MAP FOR 1700 MST ON 30 JANUARY 1976

TABLE 1. 850-mb GEOPOTENTIAL HEIGHT DATA FOR 1700 MST ON 30 JANUARY 1976

j \ i	1	20	40	60	80	100	120
1	1565	1545	1520	1490	1465	1440	1435
20	1580	1560	1530	1495	1465	1440	1430
40	1585	1565	1535	1500	1460	1435	1420
60	1580	1560	1530	1485	1455	1430	1410
80	1575	1545	1515	1475	1440	1410	1395
100	1560	1530	1490	1450	1410	1385	1370

B. FITTING OF THE POISSON EQUATION

Next, a method first developed by Harris, Thomasell, and Welsh (1966) to analyze ocean temperatures was tested. That method requires the grid values to satisfy Poisson's equation:

$$\nabla^2 Z(i,j) = F(i,j) \quad ,$$

where Z is the interpolated grid value and F is a forcing function defining the shape of the field. The data points are taken to be interval boundary conditions.

To implement this scheme, the study team first used the bilinearly interpolated geopotential height field to generate the initial field. With the data points fixed, the geopotential height field Z was required to satisfy the Laplace equation:

$$\nabla^2 Z(i,j) = 0 \quad .$$

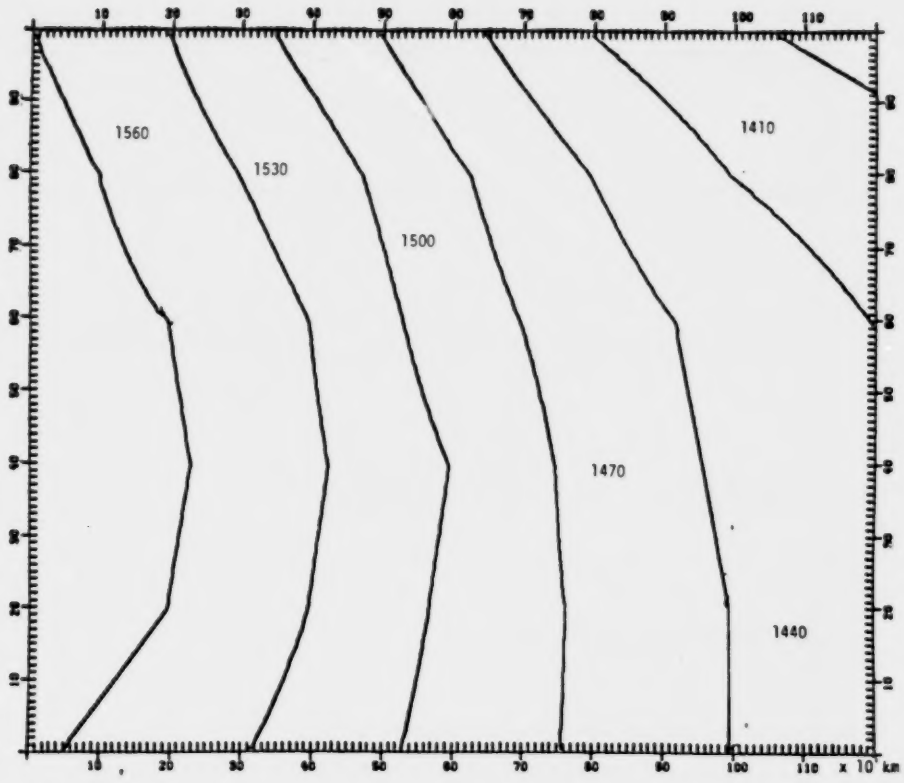

FIGURE 5. BILINEARLY INTERPOLATED GEOPOTENTIAL HEIGHT FIELD (m)

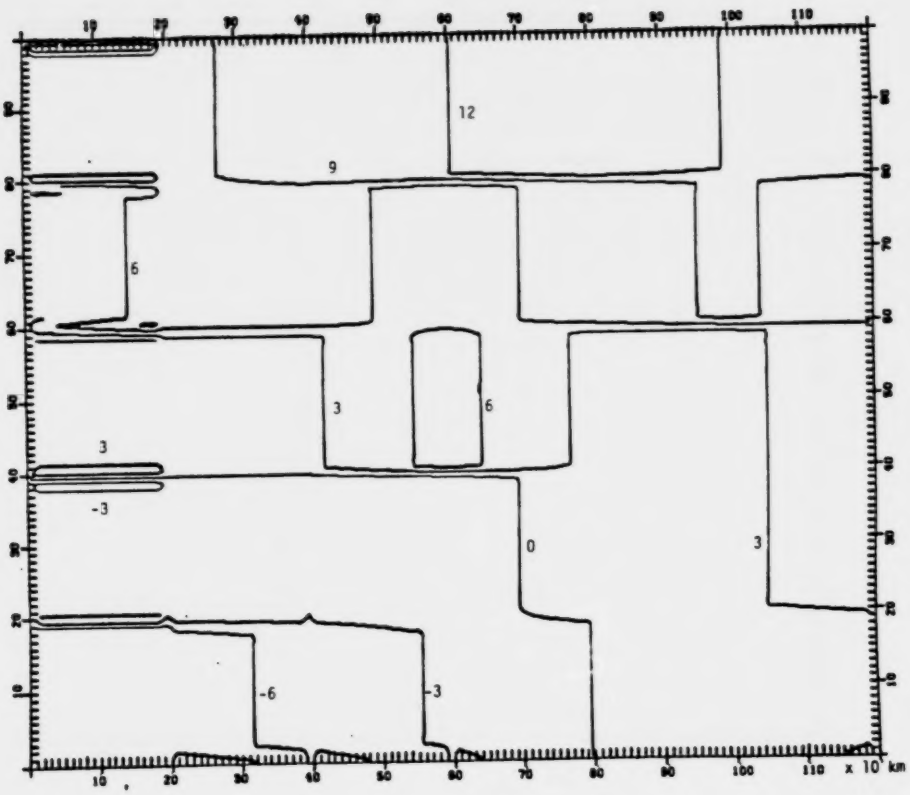

FIGURE 6. ZONAL WIND FIELD GENERATED FROM BILINEARLY INTERPOLATED GEOPOTENTIAL HEIGHT DATA (m sec^{-1})

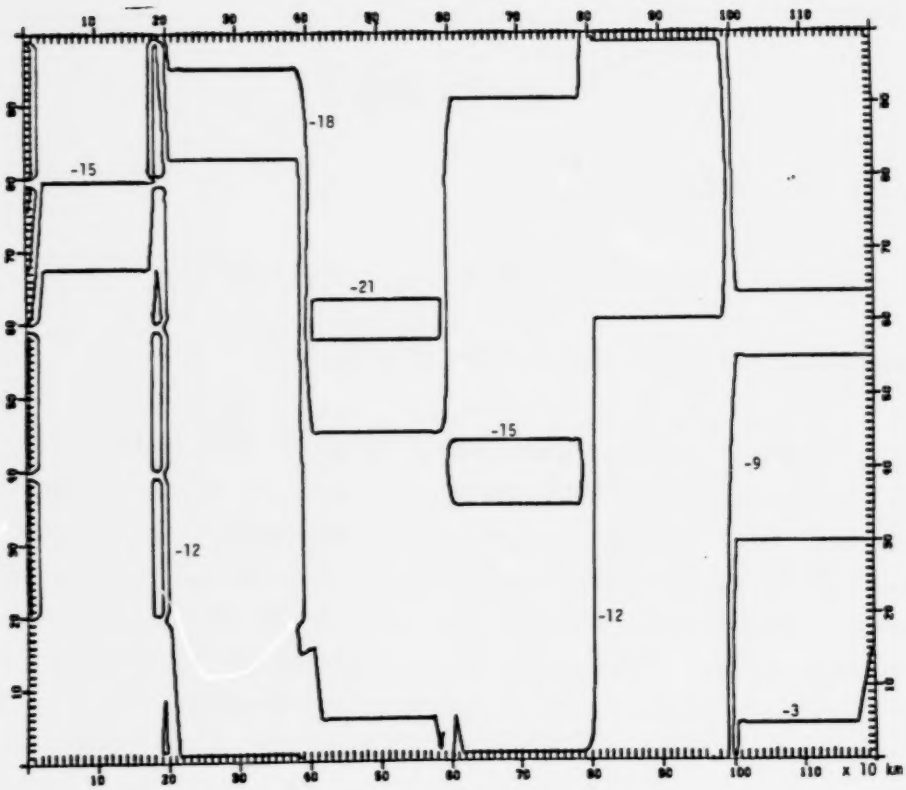

FIGURE 7. MERIDIONAL WIND FIELD GENERATED FROM BILINEARLY INTERPOLATED GEOPOTENTIAL HEIGHT DATA (m sec^{-1})

Then a simultaneous relaxation procedure was invoked in which the finite difference form of the second derivative at each nonboundary grid point was used with the residual to compute a new value:

$$\nabla^2 Z(i,j) = Z(i,j+1) + Z(i,j-1) + Z(i+1,j) + Z(i-1,j) - 4Z(i,j) \quad ;$$

then

$$R(i,j) = \nabla^2 Z(i,j) \quad ,$$

and for iteration n,

$$Z_n(i,j) = Z_{n-1}(i,j) + \alpha R_n(i,j) \quad ,$$

where α must be less than 0.5 for convergence.

The mapping of the geopotential height field based on the solution to the Laplace equation is plotted in Figures 8, 9, and 10 after 25, 125, and 150 iterations, respectively. Physically, the solution to the Laplace equation can be viewed as an elastic tent tightly stretched over poles (the data points), forming a smooth field with discontinuities at these points. The contour lines exhibited in Figure 8, 9, and 10 are smoother than those of the bilinearly interpolated field in Figure 5, except for the discontinuities around the data points. The resulting wind field is displayed in Figures 11 and 12, which clearly show the imposed constraint of keeping the data points fixed. Although the overall features of the wind field are physically more realistic, discontinuities around the data points still severely distort the velocity fields in Figures 11 and 12.

The second step of the procedure is generation of a forcing function that will allow modification of the shape of the tent and will thus, in effect, smooth the field around the data points. Using the solution of the Laplace equation found in the first step to generate the forcing

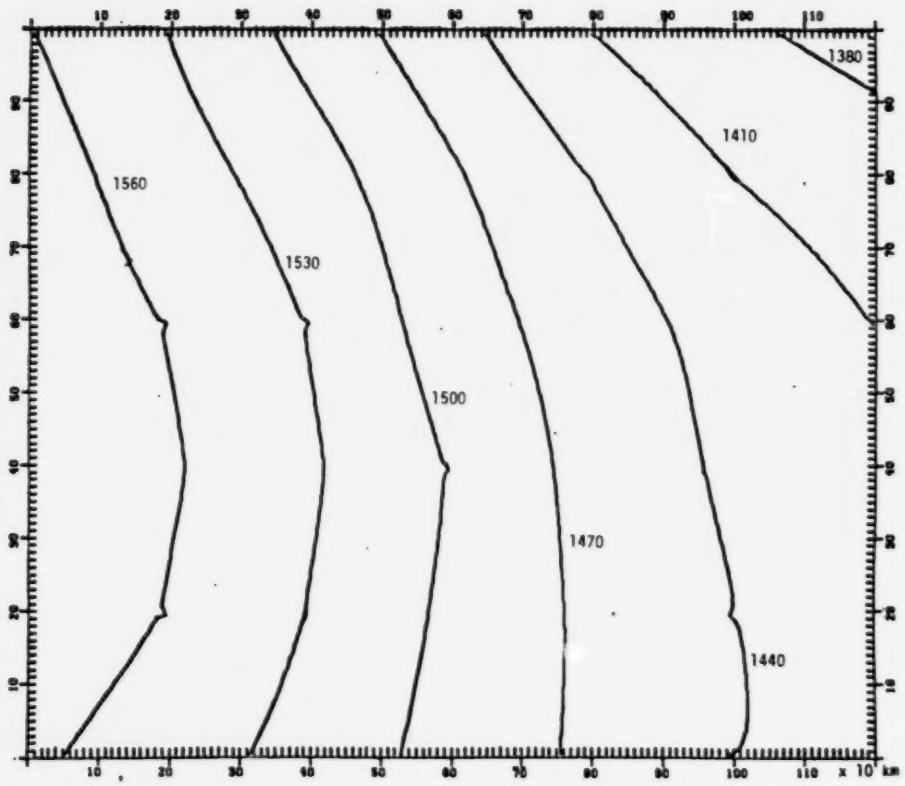

FIGURE 8. GEOPOTENTIAL HEIGHT FIELD (m) BASED ON THE SOLUTION OF THE LAPLACE EQUATION AFTER 25 ITERATIONS

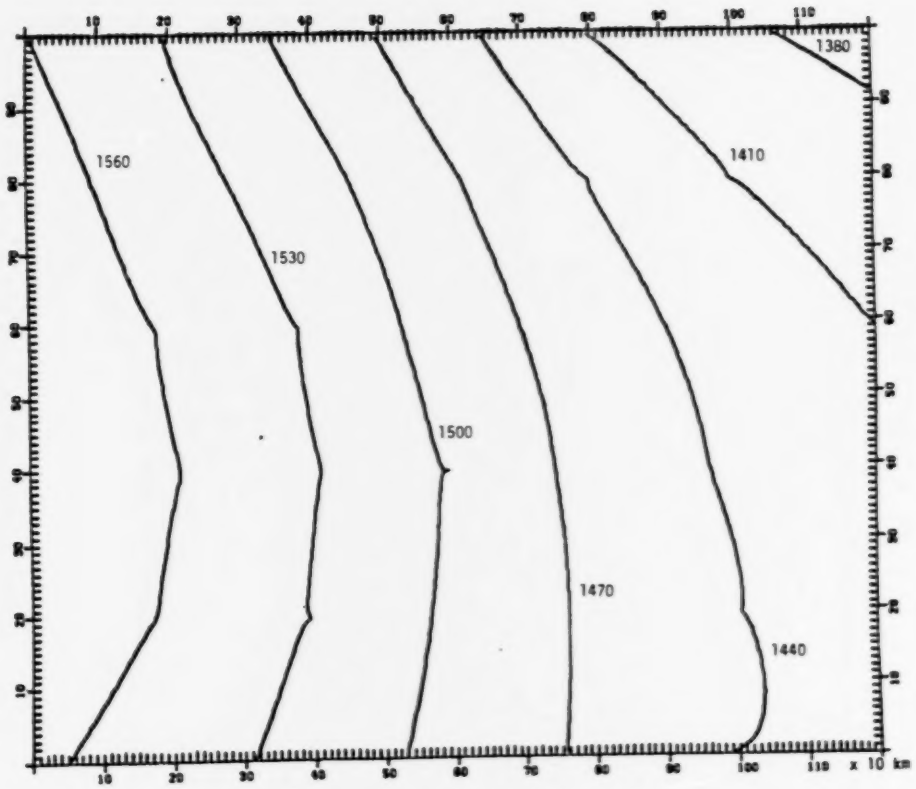

FIGURE 9. GEOPOTENTIAL HEIGHT FIELD (m) BASED ON THE SOLUTION OF THE LAPLACE EQUATION AFTER 125 ITERATIONS

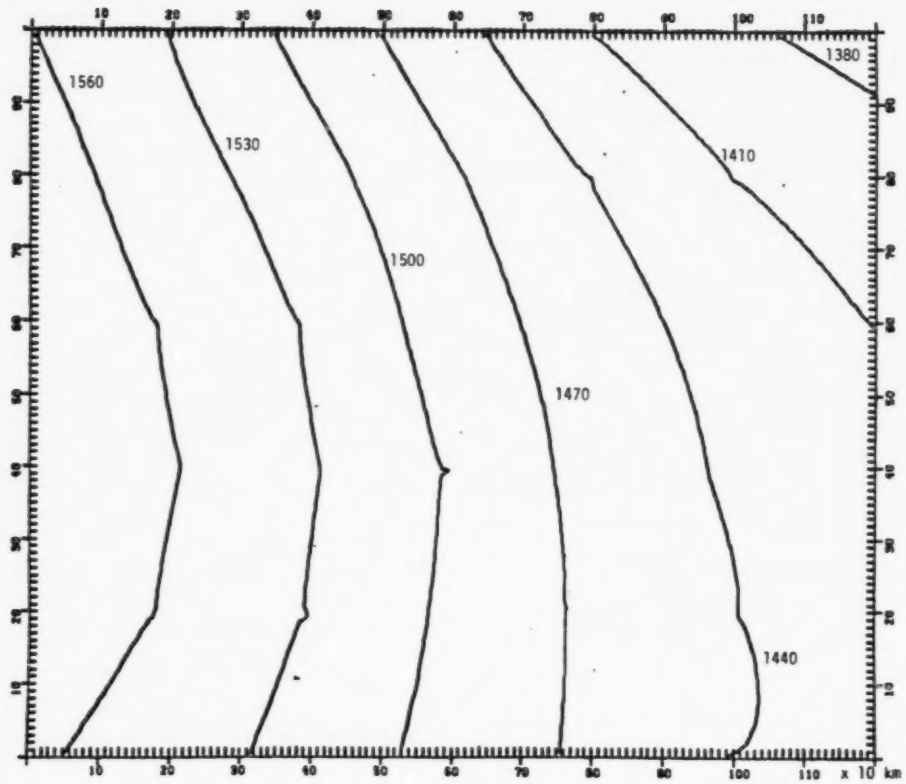

FIGURE 10. GEOPOTENTIAL HEIGHT FIELD (m) BASED ON THE SOLUTION OF THE LAPLACE EQUATION AFTER 150 ITERATIONS

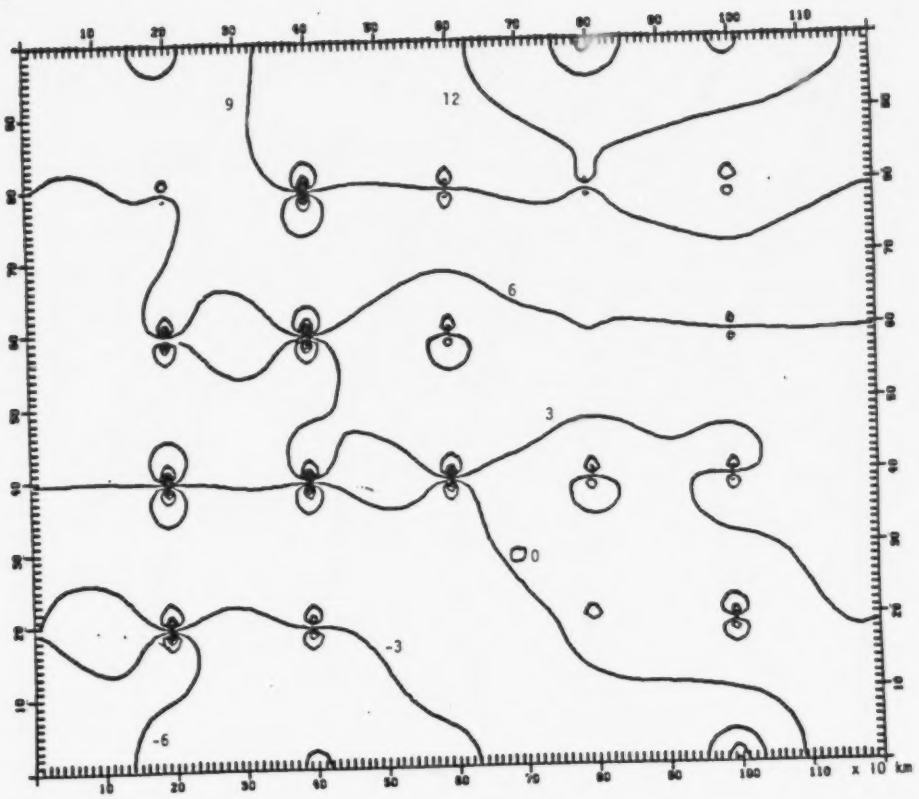

FIGURE 11. ZONAL WIND FIELD (m sec^{-1}) GENERATED FROM GEOPOTENTIAL HEIGHTS BASED ON THE SOLUTION OF THE LAPLACE EQUATION AFTER 150 ITERATIONS

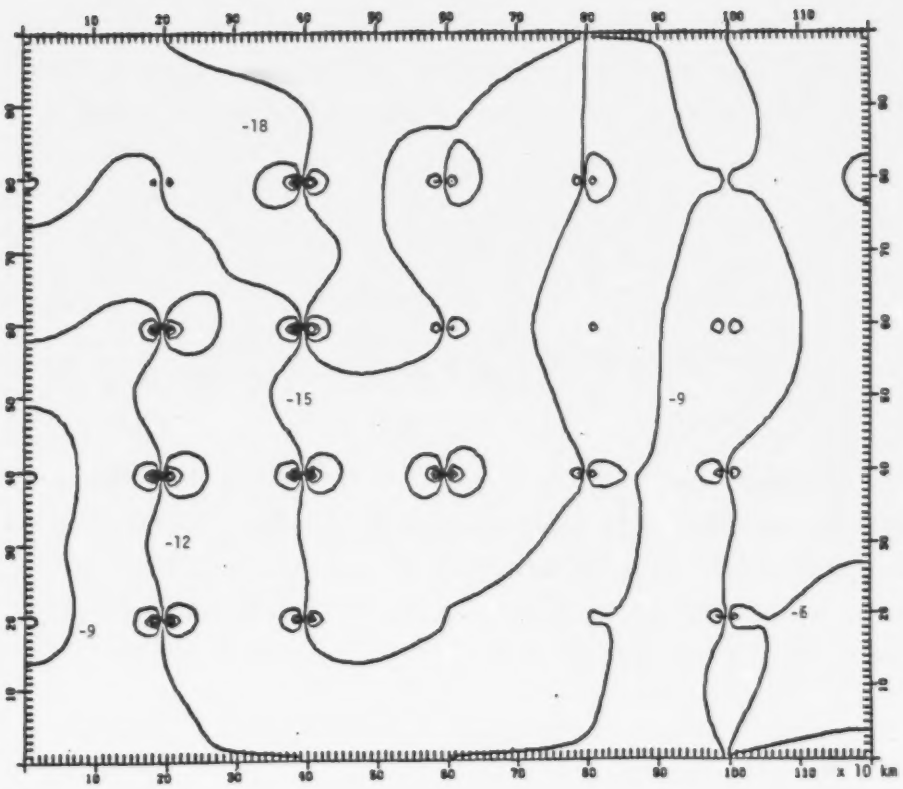

FIGURE 12. MERIDIONAL WIND FIELD (m sec^{-1}) GENERATED FROM GEOPOTENTIAL HEIGHTS BASED ON THE SOLUTION OF THE LAPLACE EQUATION AFTER 150 ITERATIONS

function, the study team computed the Laplace values around the data points and specified that the forcing function be zero elsewhere. The geopotential height fields for this case are shown in Figure 13. Apparently, the forcing functions were not strong enough to eliminate the discontinuities.

Consideration of the general shape of the geopotential height field and the resultant geostrophic wind field may provide some insight into the problem. The geopotential heights, which are on the order of 1500 m, vary only on the order of 100 m, approximately 7 percent, over a distance of 10^3 km. The resultant geostrophic wind can thus be estimated as:

$$u = \frac{g}{f}\left(\frac{\Delta Z}{\Delta x}\right)$$

$$\approx \frac{9.8}{10^{-4}}\left(\frac{10^2}{10^6}\right) \approx 10 \text{ m sec}^{-1} \quad ,$$

which is within the expected range of variations in wind speed. This result implies that accurately computing the wind field would then require determination of 1 m in geopotential height over a distance of 10 km. This value is only approximately 0.1 percent of the mean value for the geopotential height, and it is within the margin of error of the data points.

C. BICUBIC SPLINE FIT

The monotonic and small-amplitude characteristics of the geopotential height field that caused a problem in the Poisson solver algorithm render the geopotential height field ideal for a bicubic spline fit. Thus, an algorithm available at the Computer Center at Lawrence Berkeley Laboratory was used to test the feasibility of a spline fit.

Mathematically, the spline function is a piecewise cubic (third degree) polynomial passing through all data points and having continuous first and second derivatives. The spline can be viewed as a set of

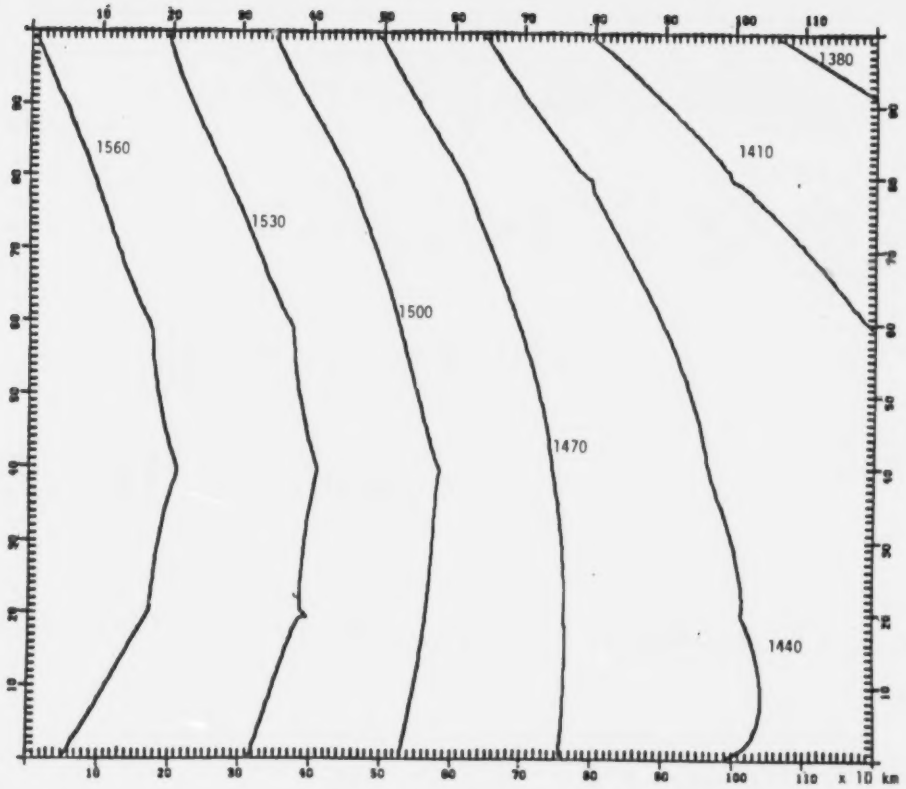

FIGURE 13. GEOPOTENTIAL HEIGHT FIELD (m) BASED ON THE SOLUTION OF THE POISSON EQUATION WITH PRESCRIBED FORCING FUNCTIONS

cubic equations, one equation for each interval between successive data points. The coefficients of the cubic equations are such that at any data point the equation for the left interval will yield the same values for the first and second derivatives, respectively, as will the equation for the right interval.

Given a set of N data points for which the coordinates (X_i,Y_i) and second derivatives (M_i) are known for every point (i = 1, 2, 3, ..., N), the interpolating spline function S(x) is defined as:

$$S(x) = \frac{1}{6} M_i \frac{(X_{i+1} - x)^3}{X_{i+1} - X_i} + \frac{1}{6} M_{i+1} \frac{(x - X_i)^3}{X_{i+1} - X_i}$$

$$+ \left[Y_i - \frac{1}{6} M_i (X_{i+1} - X_i)^2\right] \frac{X_{i+1} - x}{X_{i+1} - X_i}$$

$$+ \left[Y_{i+1} - \frac{1}{6} M_{i+1} (X_{i+1} - X_i)^2\right] \frac{x - X_i}{X_{i+1} - X_i} \quad ,$$

where i is such that $X_i \leq x \leq X_{i+1}$. The first and second derivatives are:

$$S'(x) = -\frac{M_i}{2} \frac{(X_{i+1} - x)^2}{X_{i+1} - X_i} + \frac{M_{i+1}}{2} \frac{(x - X_i)^2}{X_{i+1} - X_i}$$

$$+ \frac{Y_{i+1} - Y_i}{X_{i+1} - X_i} + \frac{1}{6} (M_i - M_{i+1})(X_{i+1} - X_i) \quad ,$$

$$S''(x) = M_i \left(\frac{X_{i+1} - x}{X_{i+1} - X_i}\right) + M_{i+1} \left(\frac{x - X_i}{X_{i+1} - X_i}\right) \quad .$$

Many compact and efficient algorithms are available for evaluating the coefficients M_i (DeBoor, 1962).

Specifying only the 42 data points, the study team produced the field shown in Figure 14. Since the gradients and shape appeared promising, zonal and meridional velocity components were calculated, as shown in Figures 15 and 16. With the exception of slightly erratic behavior at the boundaries, the field seems smooth. The computed wind vectors are presented in Figure 17, in which the lengths of the arrows are proportional to speed.

Since the bicubic spline fit appears to be the most suitable interpolation technique for the present study, it was used to generate the wind field from geopotential heights in the Regional Air Quality Model.

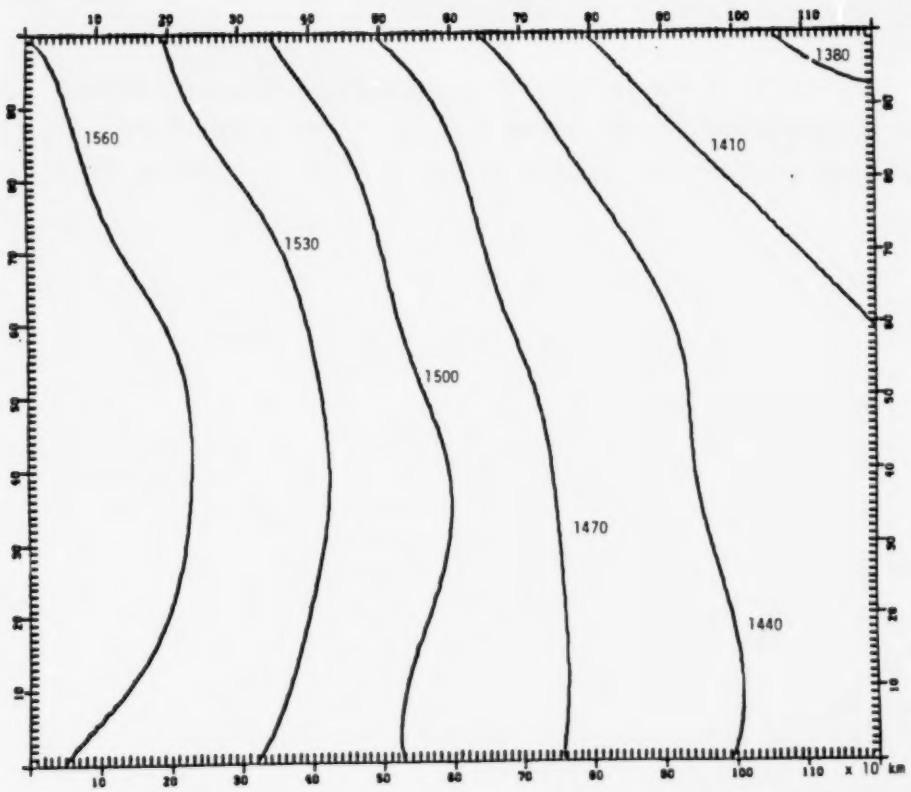

FIGURE 14. BICUBIC SPLINE FIT OF GEOPOTENTIAL HEIGHT DATA (m)

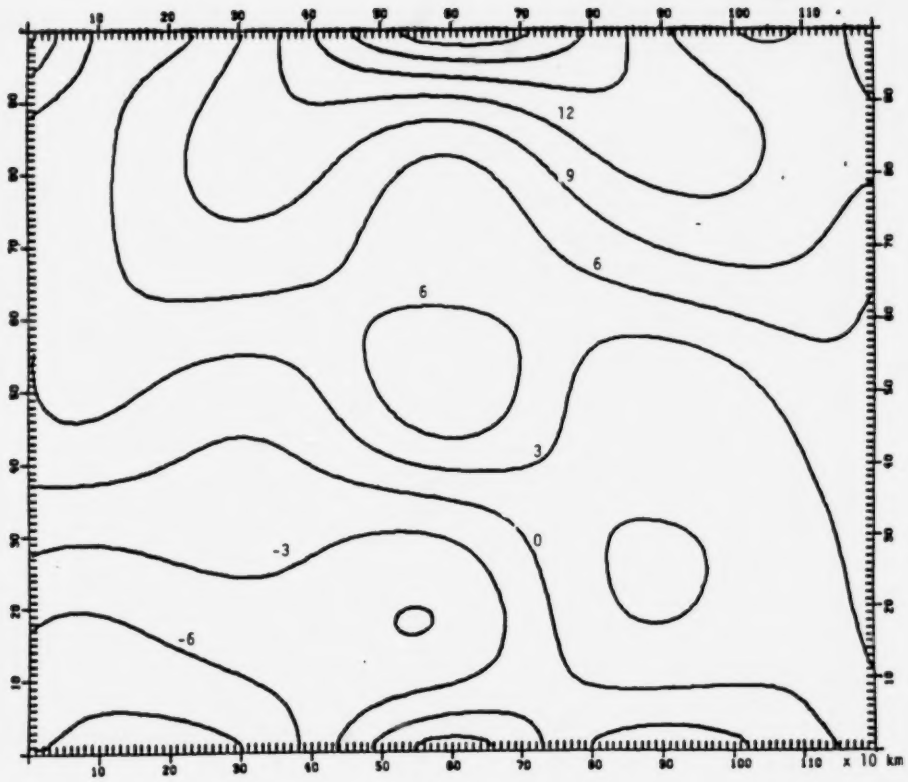

FIGURE 15. ZONAL WIND FIELD (m sec^{-1}) GENERATED BY A BICUBIC SPLINE FIT OF GEOPOTENTIAL HEIGHT DATA

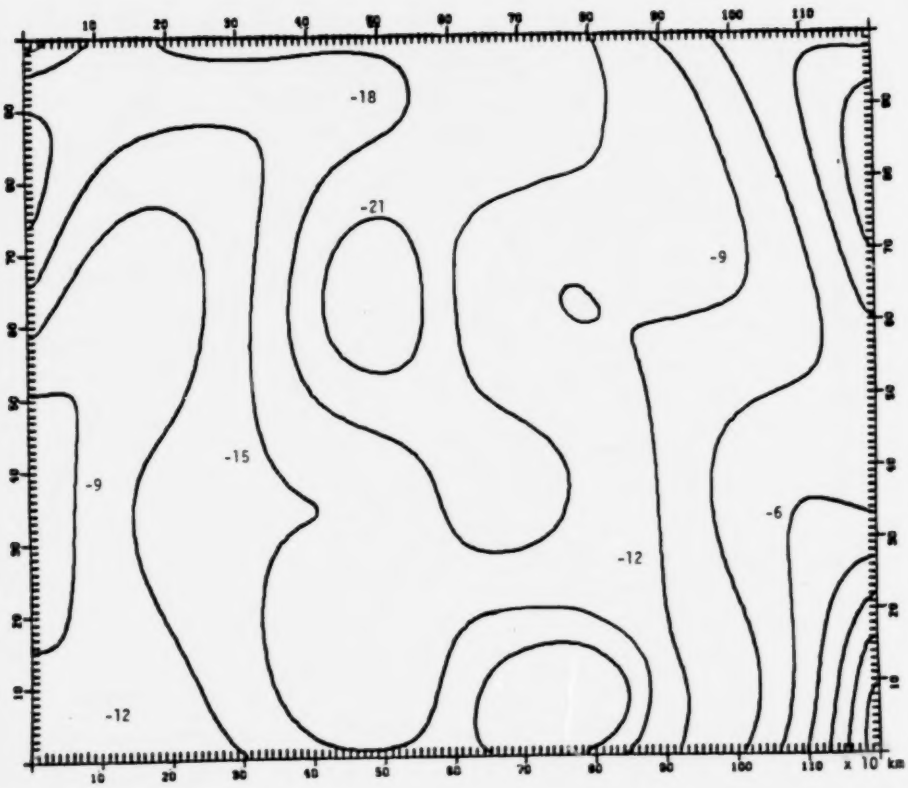

FIGURE 16. MERIDIONAL WIND FIELD (m sec^{-1}) GENERATED BY A BICUBIC SPLINE FIT OF GEOPOTENTIAL HEIGHT DATA

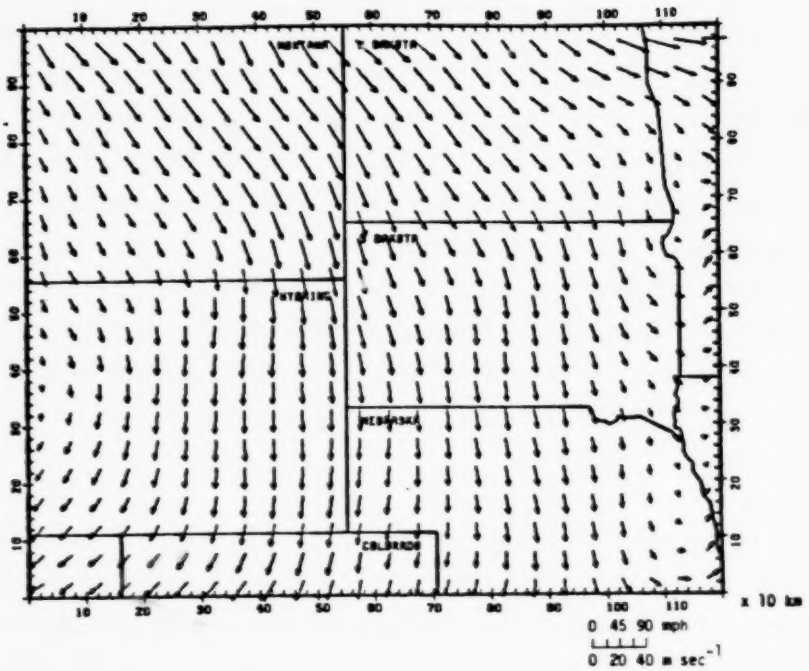

FIGURE 17. WIND VECTORS GENERATED BY A BICUBIC SPLINE FIT OF GEOPOTENTIAL HEIGHT DATA

V SENSITIVITY OF THE TRANSPORT AND DIFFUSION CHARACTERIZATION SCHEME

To test the sensitivity of the transport and diffusion characterization scheme described in the previous chapter, the study team recomputed the wind field and the diffusivity field for the three time periods studied under the original contract. The pertinent 850-mb weather maps were used in this exercise. As shown in Figures 18, 19, and 20, in the grid representing the Great Plains region overlaid on the maps, each cell contains 400 cells of the Regional Model. The geopotential height fields generated from the 42 data points extracted using the appropriate weather map and a bicubic spline fit are displayed in Figures 21, 22, and 23. Comparison of the interpolated height field contour lines with the weather maps shows that the spline fit scheme works equally well for three different types of wind flow patterns.

Figures 24 through 29 present sets of wind fields and horizontal eddy diffusivity fields, in which the former are represented graphically, and the latter (K_H) are represented by contour lines with values of 0.1×10^4 m^2 sec^{-1}, 0.5×10^4 m^2 sec^{-1}, and 1×10^4 m^2 sec^{-1}. In the original Regional Model, a constant value of 1×10^4 m^2 sec^{-1} was used for K_H. The velocity diagrams show that the three days studied have interesting and differing flow patterns.

For 27 January 1976, as shown in Figure 24, the curvature of the flow changes from top to bottom on the left side of the figure. Flow on the right side is weak and uniform. The effect of this change in curvature on the resulting value of K_H is shown in Figure 25. On the left side of the Great Plains region, horizontal diffusion is uniformly large, but K_H decreases by an order of magnitude on the right side of the region.

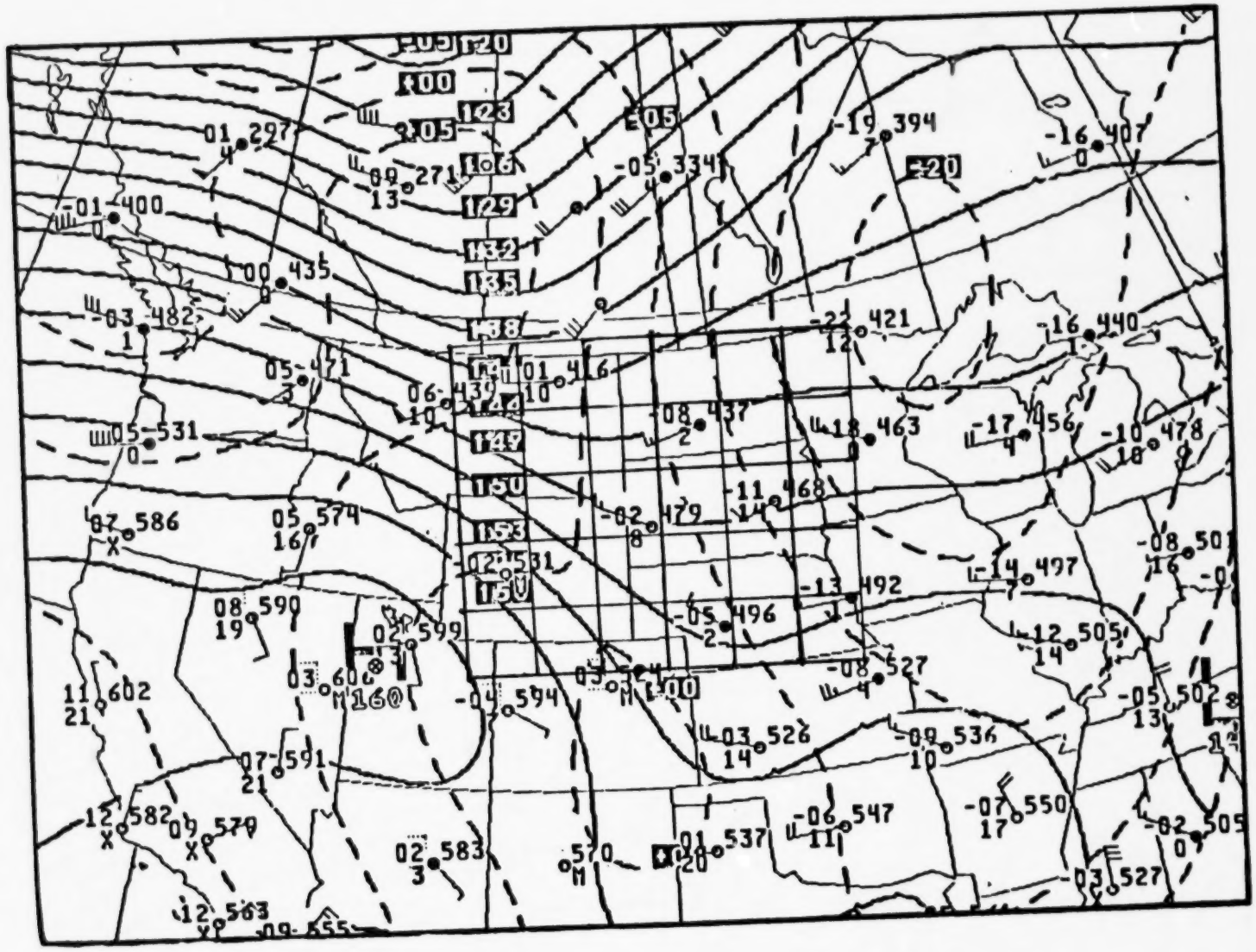

FIGURE 18. 850-mb WEATHER MAP FOR 500 MST ON 27 JANUARY 1976

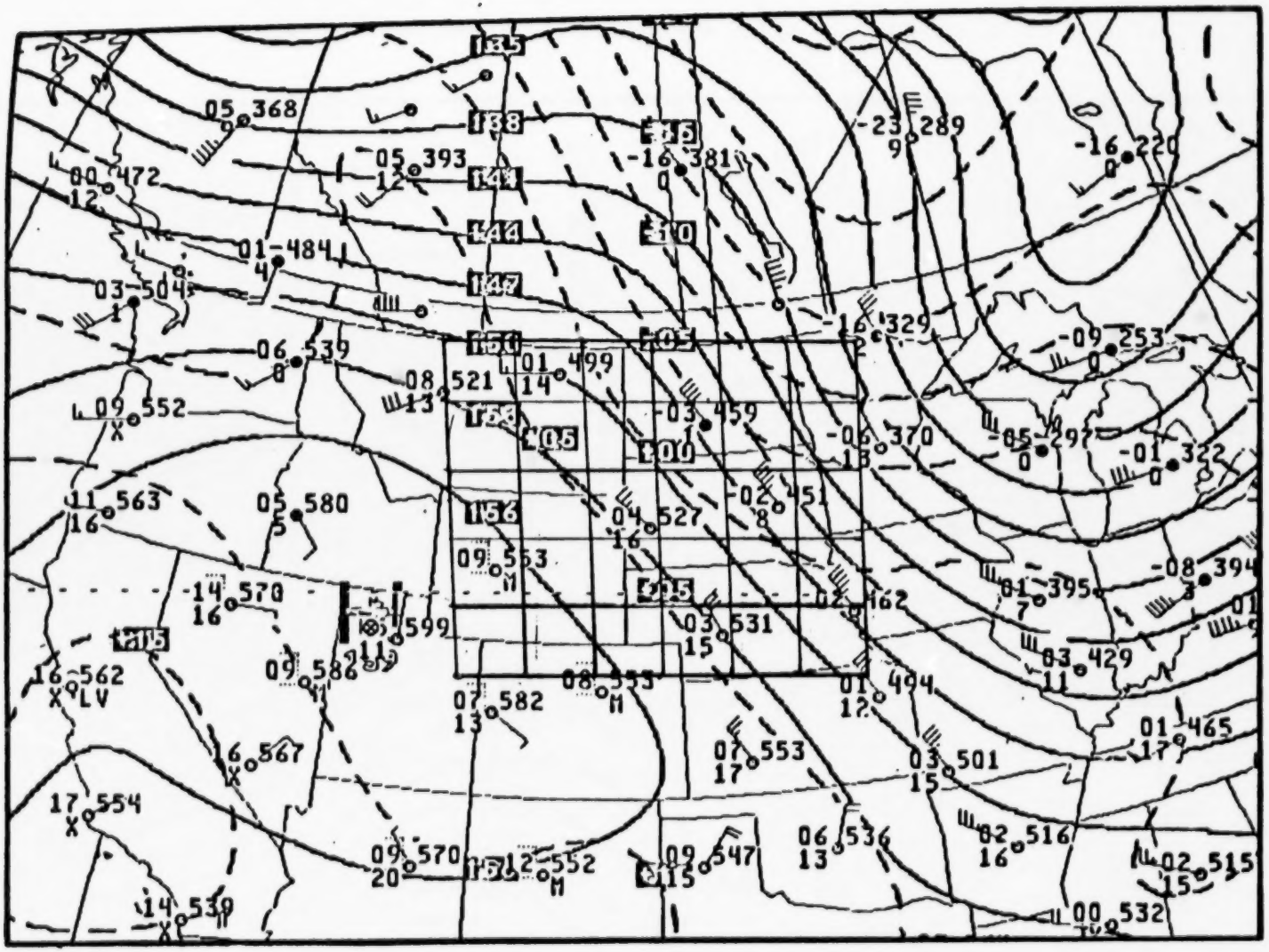

FIGURE 19. 850-mb WEATHER MAP FOR 1700 MST ON 28 JANUARY 1976

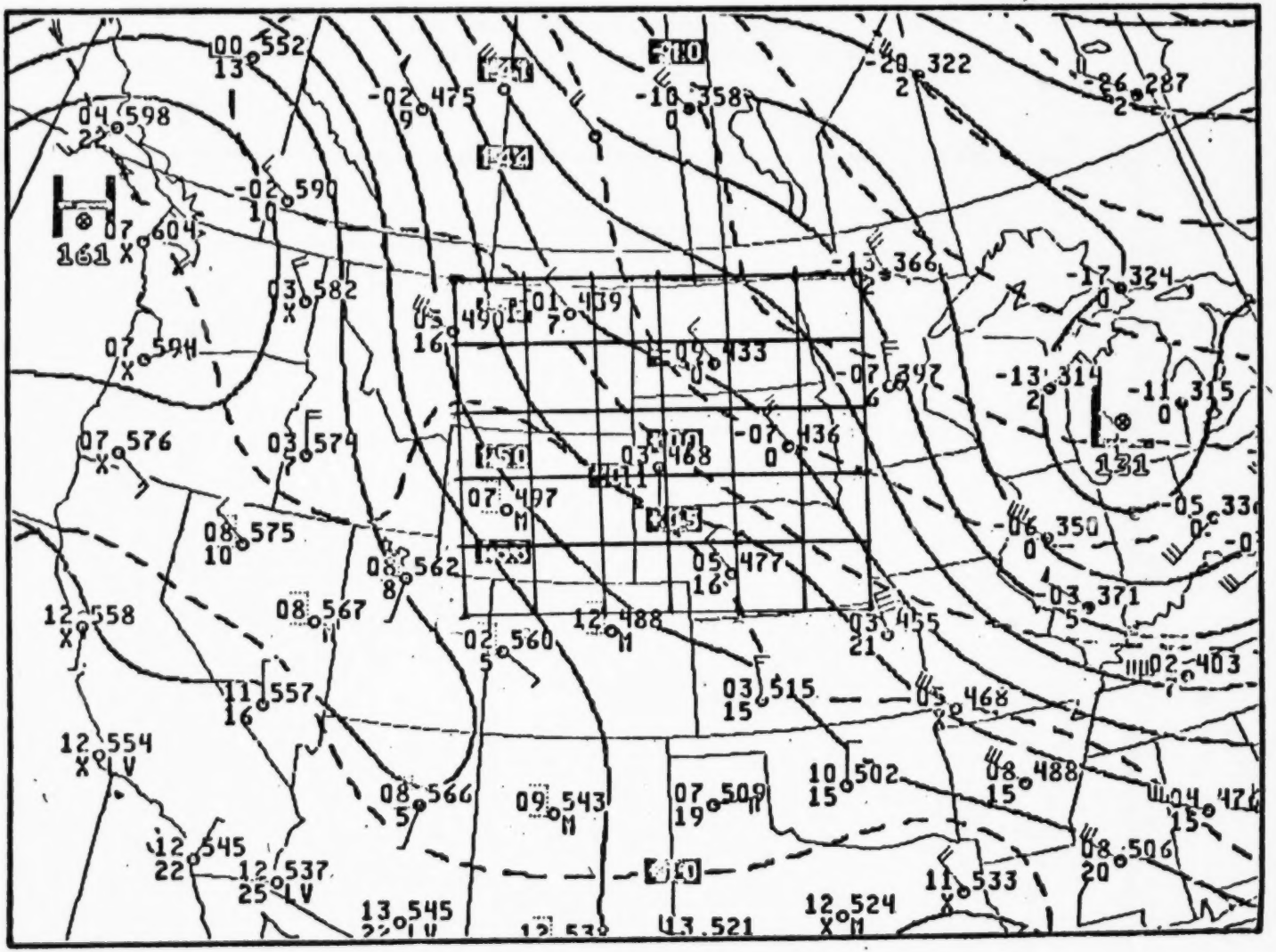

FIGURE 20. 850-mb WEATHER MAP FOR 500 MST ON 30 JANUARY 1976

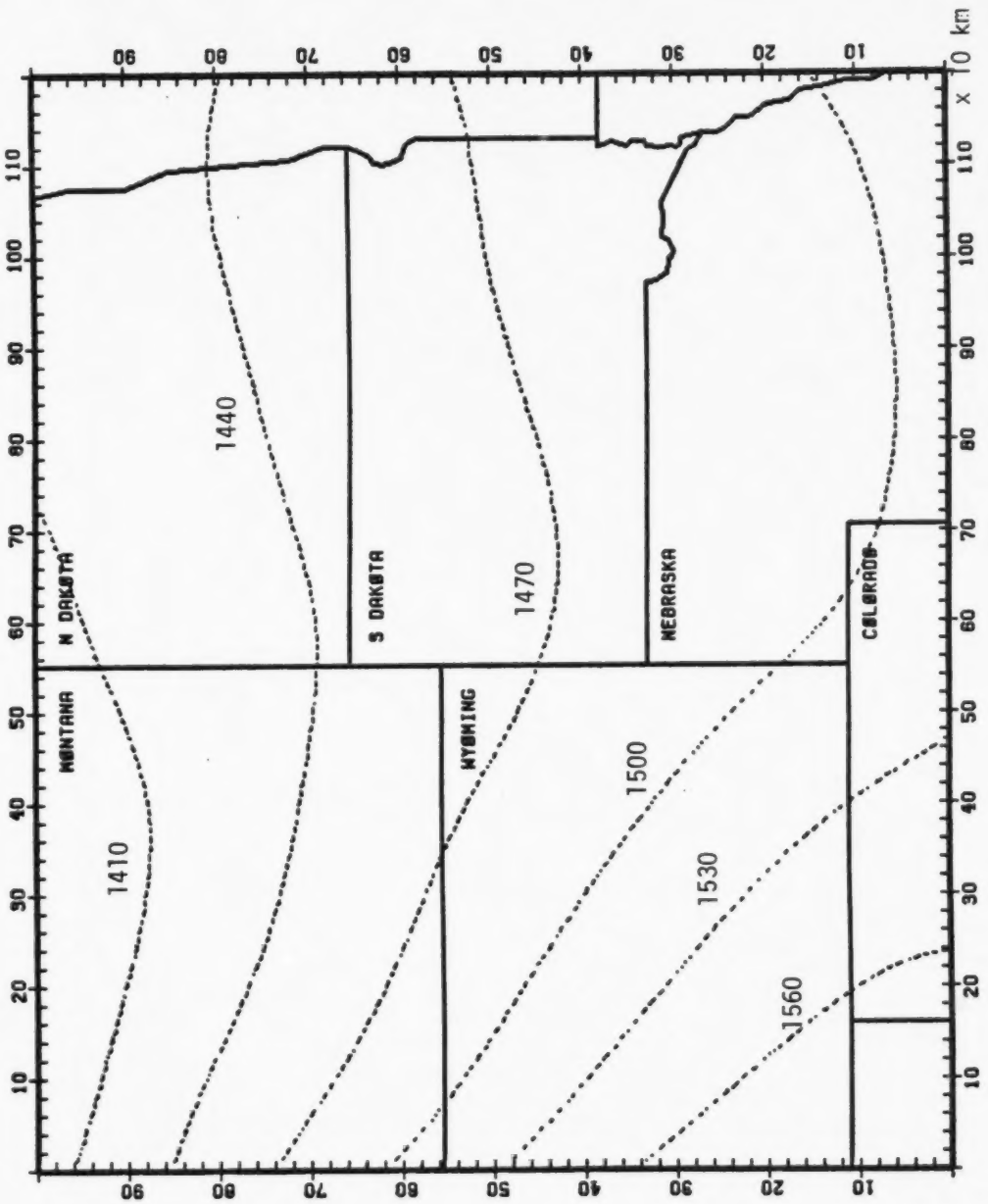

FIGURE 21. BICUBIC SPLINE FIT OF GEOPOTENTIAL HEIGHT DATA (m)
FOR 500 MST ON 27 JANUARY 1976

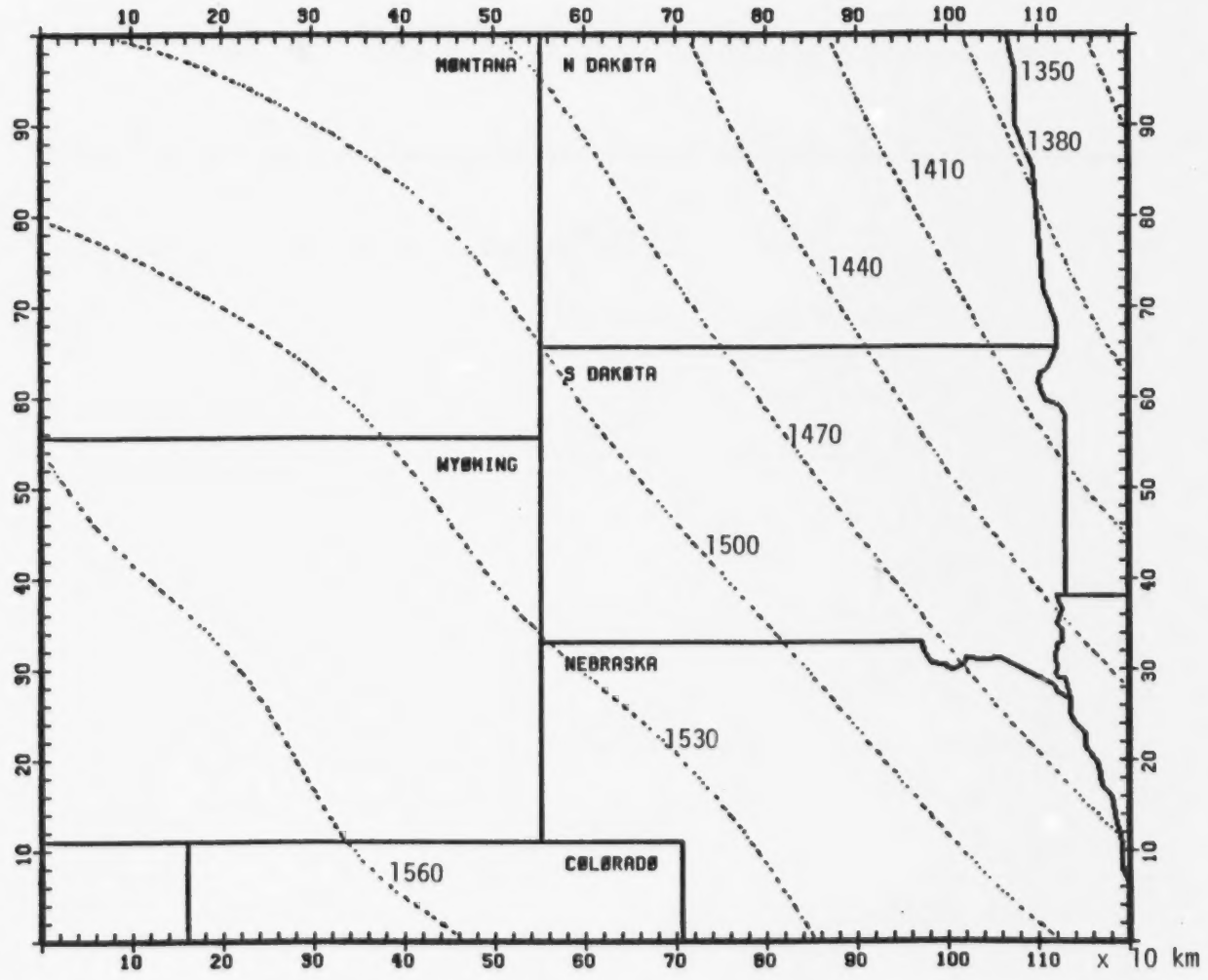

FIGURE 22. BICUBIC SPLINE FIT OF GEOPOTENTIAL HEIGHT DATA (m) FOR 1700 MST ON 28 JANUARY 1976

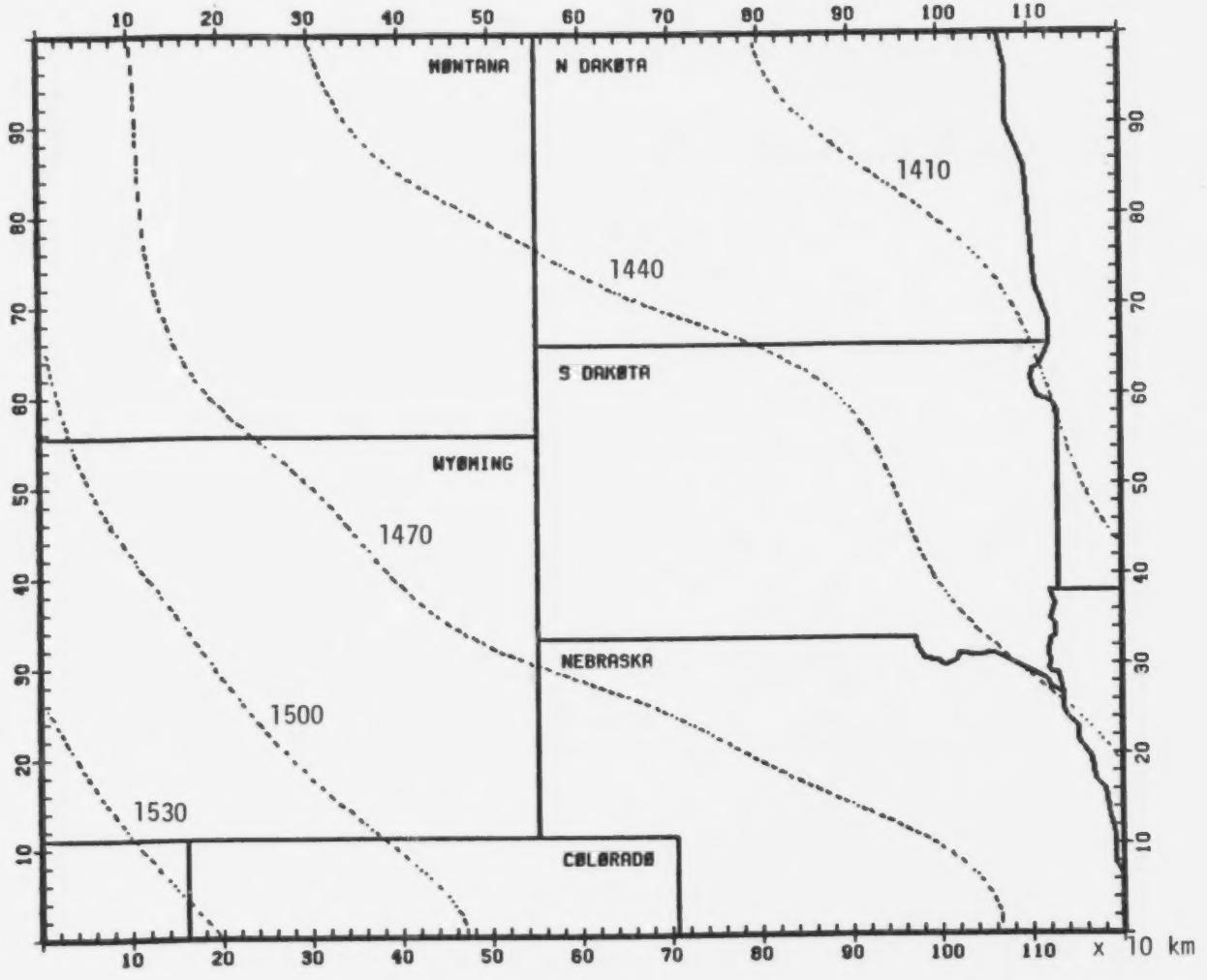

FIGURE 23. BICUBIC SPLINE FIT OF GEOPOTENTIAL HEIGHT DATA (m) FOR 500 MST ON 30 JANUARY 1976

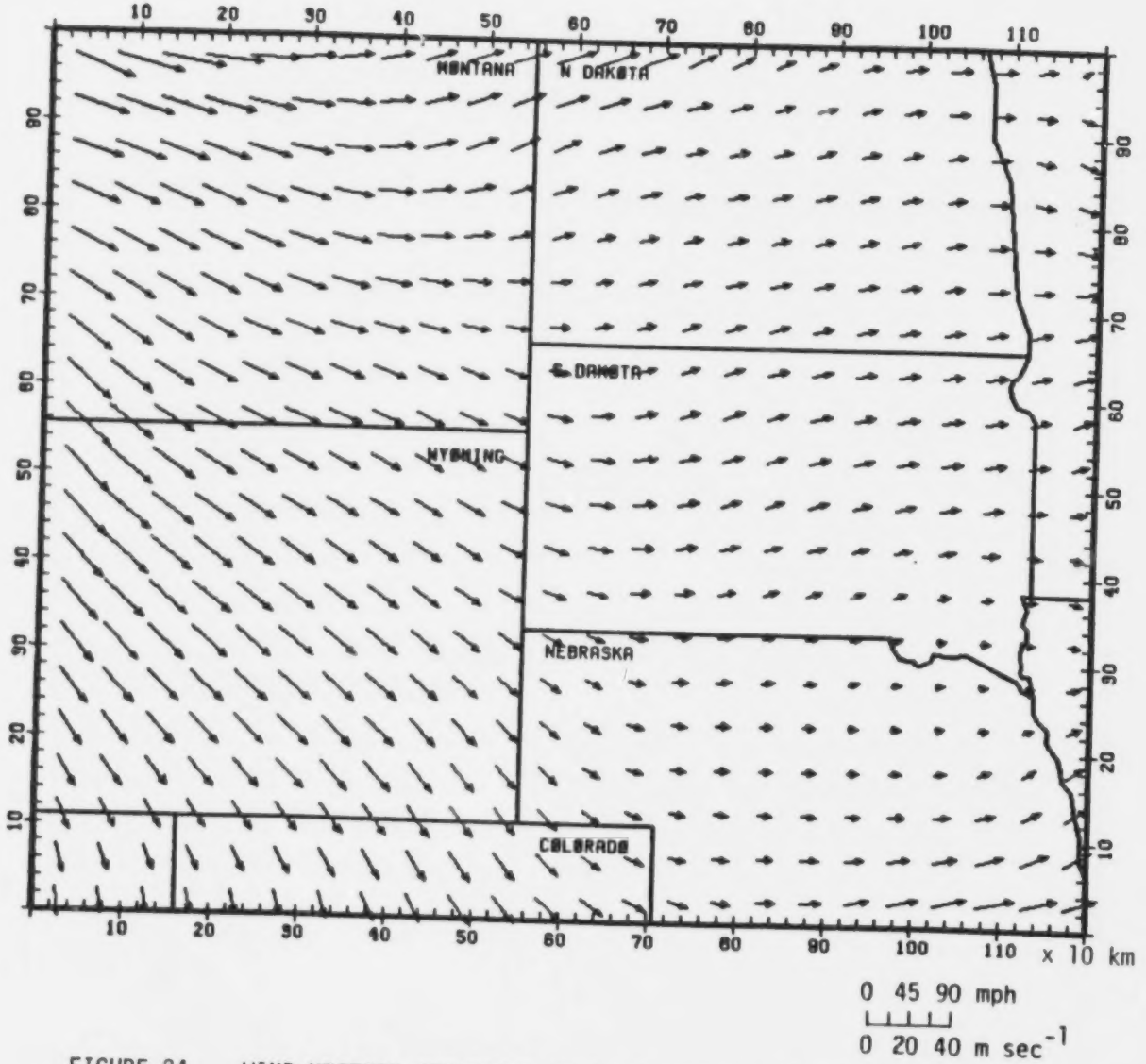

FIGURE 24. WIND VECTORS GENERATED BY A BICUBIC SPLINE FIT OF GEOPOTENTIAL HEIGHT DATA FOR 500 MST ON 27 JANUARY 1976

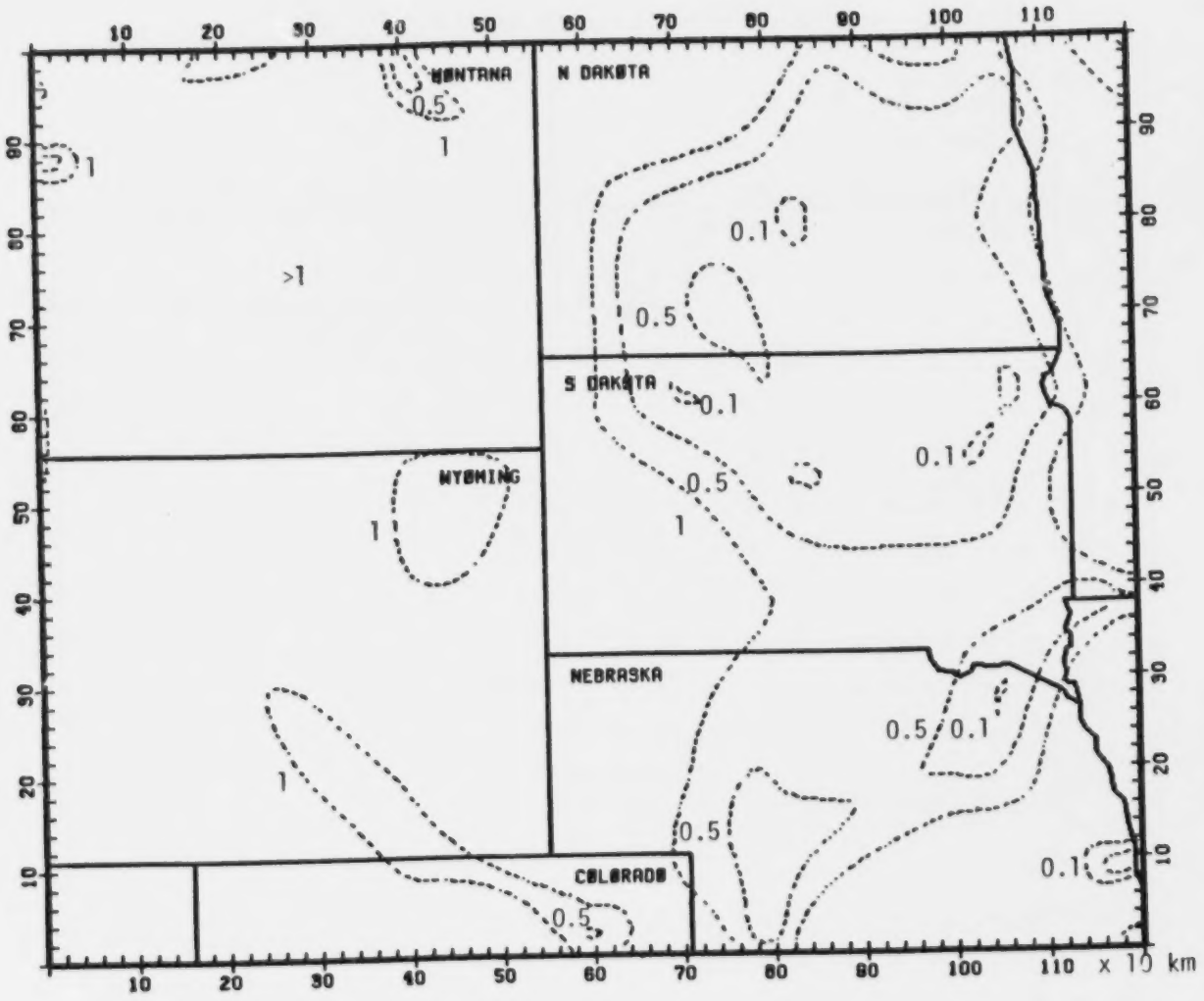

FIGURE 25. THE COMPUTED HORIZONTAL EDDY DIFFUSIVITY (IN 10^4 m^2 sec^{-1}) FOR 500 MST ON 27 JANUARY 1976

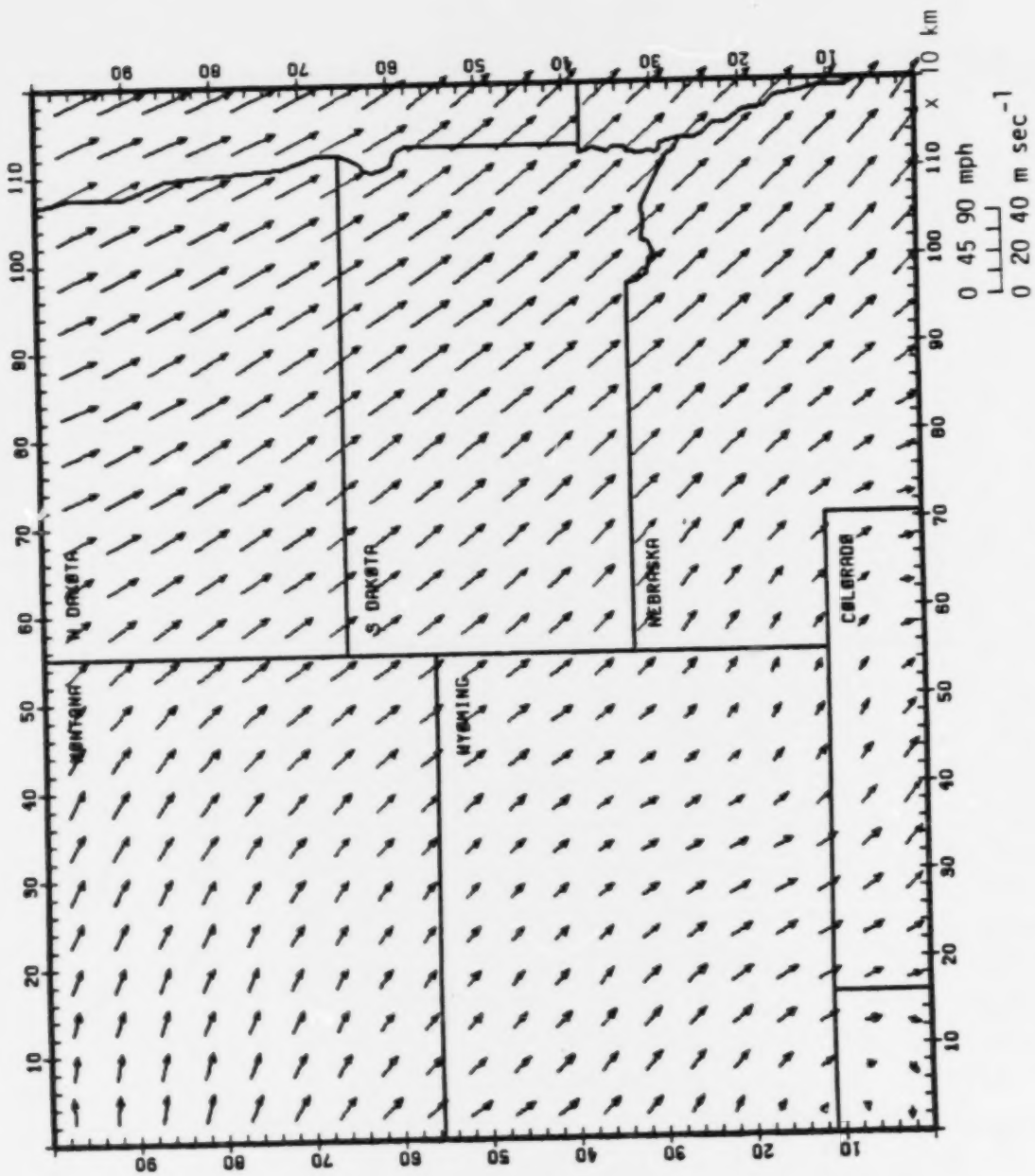

FIGURE 26. WIND VECTORS GENERATED BY A BICUBIC SPLINE FIT OF GEOPOTENTIAL HEIGHT DATA FOR 1700 MST ON 28 JANUARY 1976

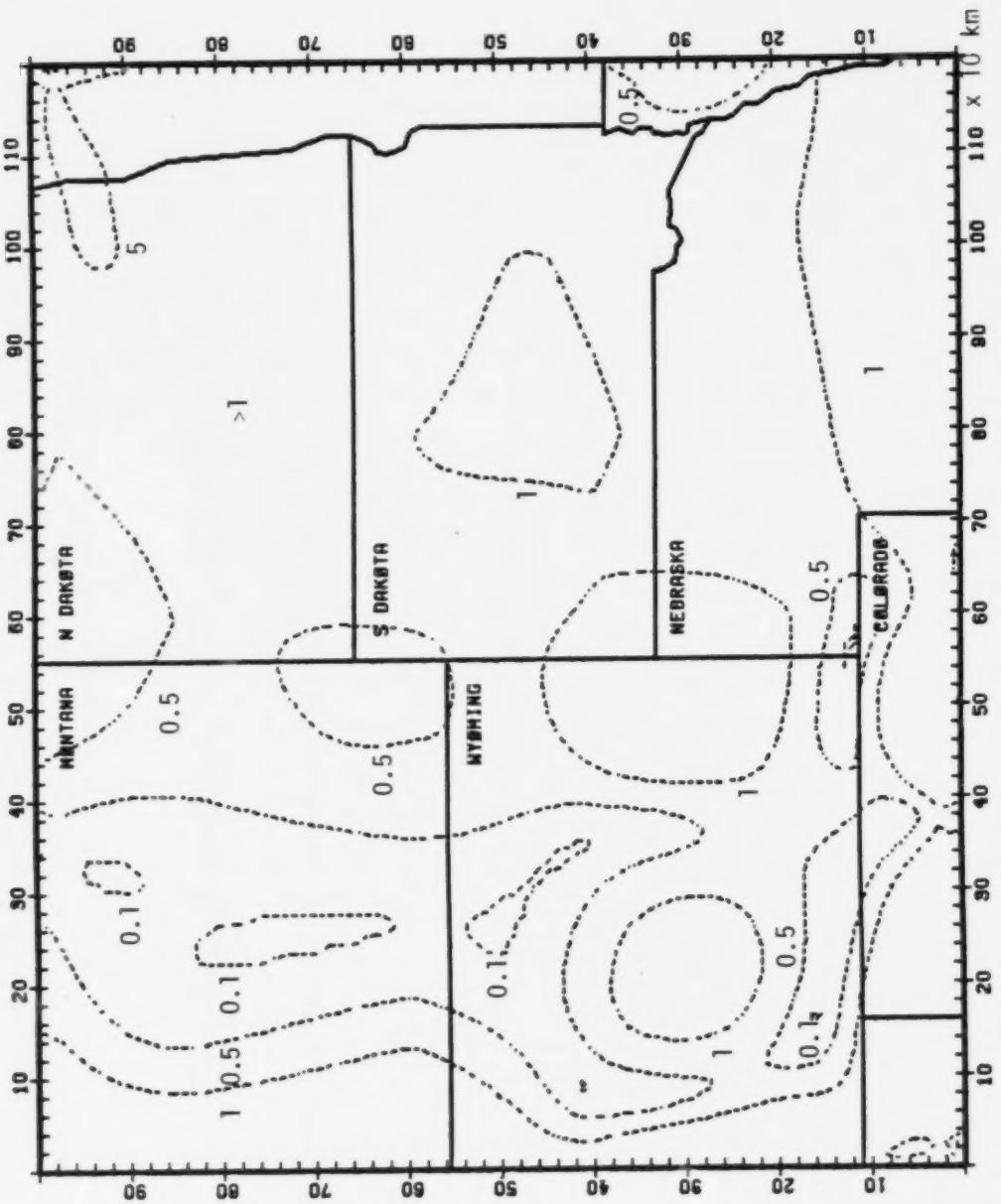

FIGURE 27. THE COMPUTED HORIZONTAL EDDY DIFFUSIVITY (IN 10^4 m^2 sec^{-1}) FOR 1700 MST ON 28 JANUARY 1976

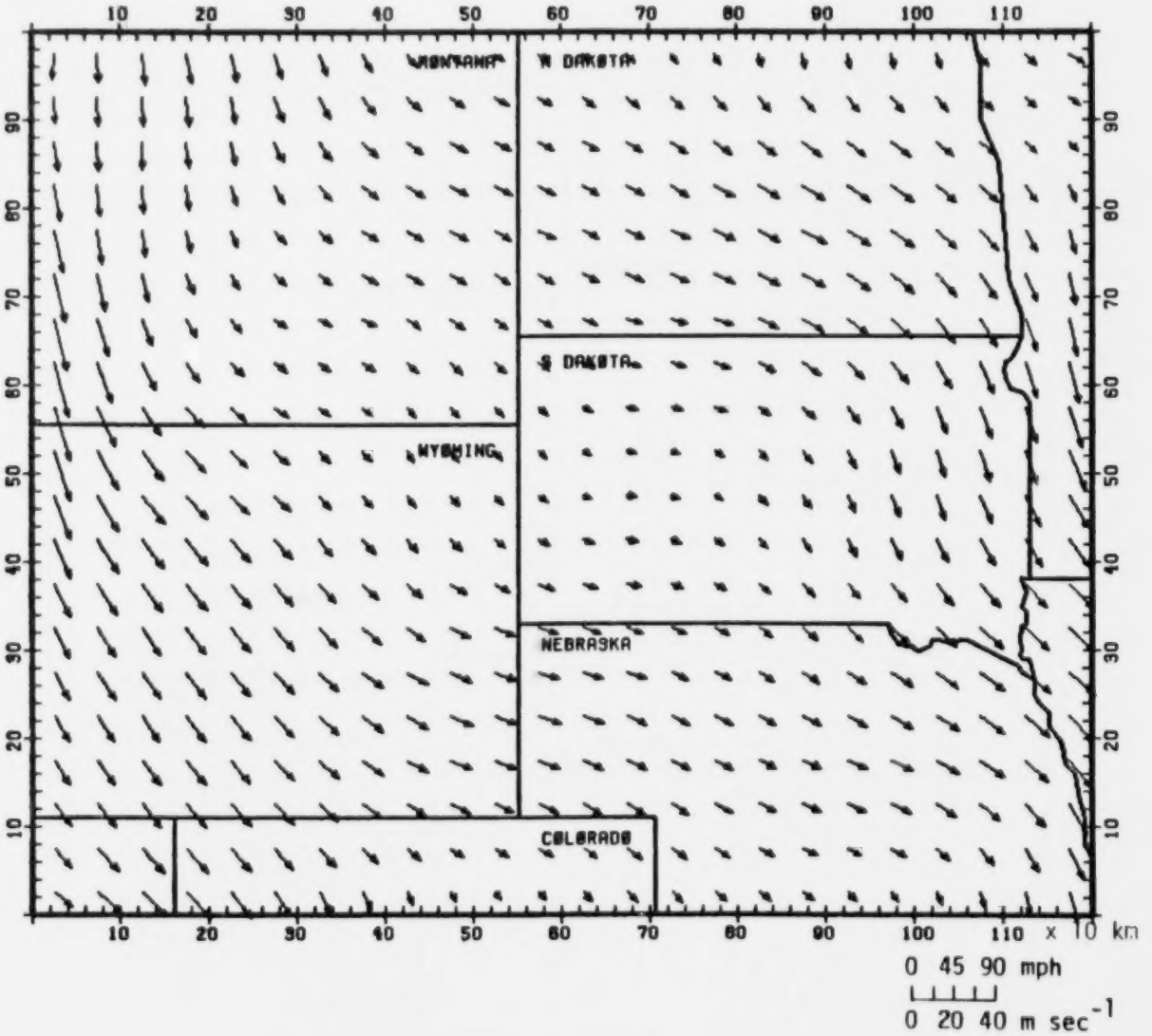

FIGURE 28. WIND VECTORS GENERATED BY A BICUBIC SPLINE FIT OF GEOPOTENTIAL HEIGHT DATA FOR 500 MST ON 30 JANUARY 1976

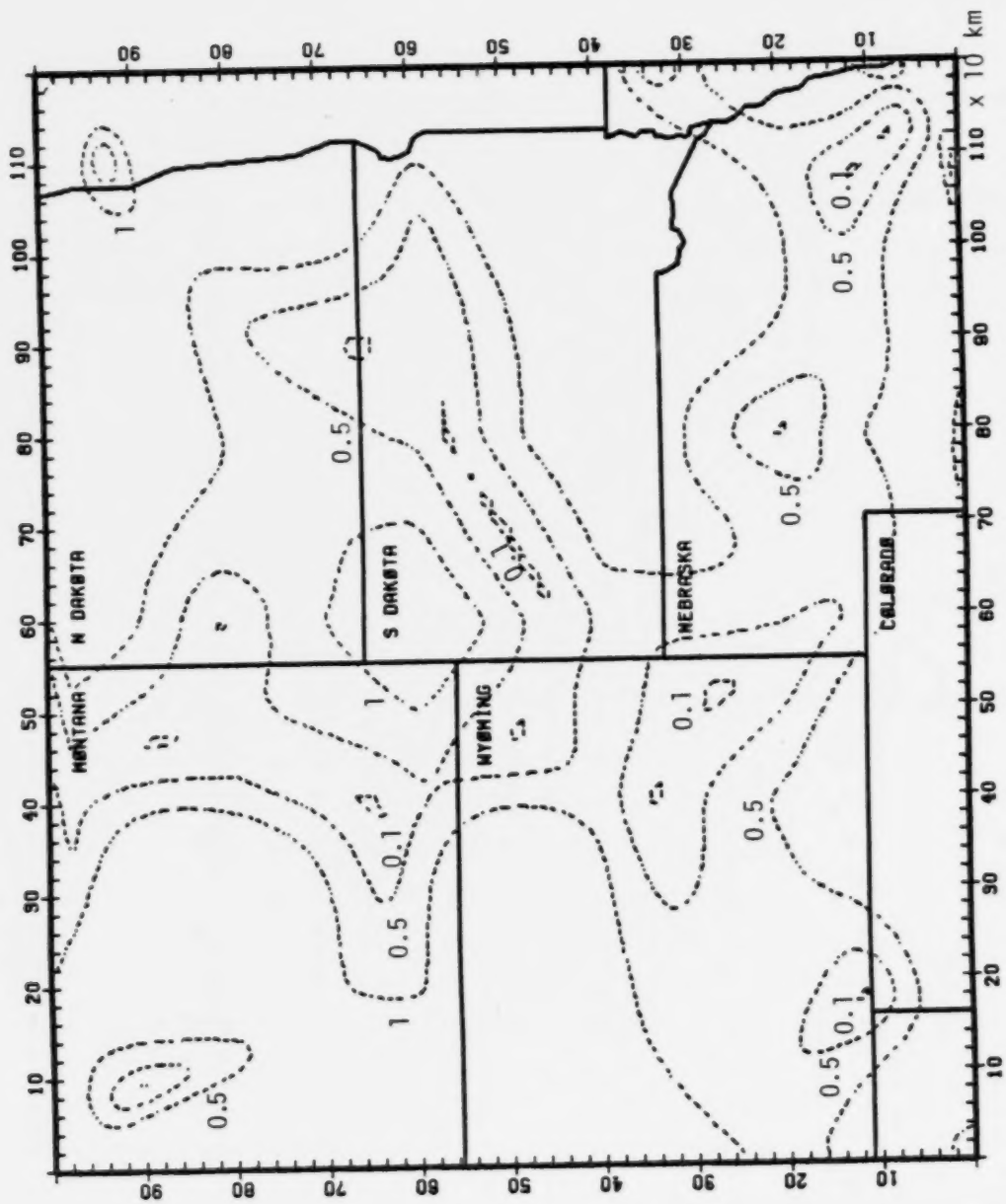

FIGURE 29. THE COMPUTED HORIZONTAL EDDY DIFFUSIVITY (IN 10^4 m^2 sec^{-1}) FOR 500 MST ON 30 JANUARY 1976

The 28 January 1976 example (Figures 26 and 27) was chosen because of the manner in which the flow increases from the lower left to the upper right corner of the region. The flow is relatively weak and uniform on the left side of the diagram. The shear caused by increasing wind speed results in high values of horizontal diffusivity in the upper right portion of the area.

The wind field for the final test case (30 January 1976), shown in Figure 28, indicates that the flow is quite weak and diffuse near the center of the region, resulting in a highly variable diffusion field. Although flow is weak in the center, it is divergent, thereby causing the maximum value of diffusion to be near the center of the region. Quite near the diffusion maximum the weak field is more uniform, and a K_H minimum occurs.

In adapting Smagorinsky's (1963) global-scale parameterization scheme to the regional scale, the study team found it necessary to increase the empirical coefficient, α. This change is in line with dimensional analysis for the scale of interest to this study. Also, a lower bound of 10^3 m^2 sec^{-1} was imposed on K_H; when deformation is weak, other dominant turbulent processes may take place that are responsible for the horizontal diffusivity at this magnitude. In a study of horizontal diffusion, Gelinas and Walton (1974) divided turbulent processes into two components. One of the terms, derived from similarity theory, proves to be a lower bound; on the scale of the present study, it is on the order of 10^3 m^2 sec^{-1}.

The field of horizontal eddy diffusivity in the three test cases is realistic in both magnitude and range. Thus, the study team proceeded to evaluate the effect of the diffusion algorithm on the Regional Air Pollution Model.

VI ANALYSIS OF THE RESULTS

To examine the effect of the new transport and diffusivity characterization scheme on the model's predictions, the study team exercised the Regional Air Pollution Model for the three meteorological patterns discussed in the previous chapter using the 1976 and 1986 emissions scenarios developed for the previous study under this contract. The sensitivity of SO_2 and SO_4 concentrations to the SO_2-to-SO_4 conversion rate were also studied. Table 2 lists the computer simulations performed under the contract extension.

TABLE 2. LIST OF THE COMPUTER SIMULATIONS

Case	Meteorological Scenario	Emissions Scenario	SO_2-to SO_4 Conversion Rate (percent per hour)
1	Spring, 4-7 April 1976	1976	0.3%
2	Spring, 4-7 April 1976	1986	0.3
3	Spring, 4-7 April 1976	1976	1.0
4	Spring, 4-7 April 1976	1986	1.0
5	Winter, 27-31 January 1976	1986	1.0
6	Summer, 9-11 July 1975	1986	1.0

Selected computed wind fields are shown in Figures 30 through 35. Wind fields for the winter case were shown earlier in Figures 24, 26, and 28. The resulting SO_2 concentration fields for Case 1 are compared with fields from the original study in Figures 36 through 38. The concentration fields are three-hour averages 27, 36, and 51 hours after the start of the simulations. A comparison at the same time for Case 2 is given in Figures 39 through 41. The main difference between the original and new meteorological data bases reflects the use of wind fields and horizontal diffusivities

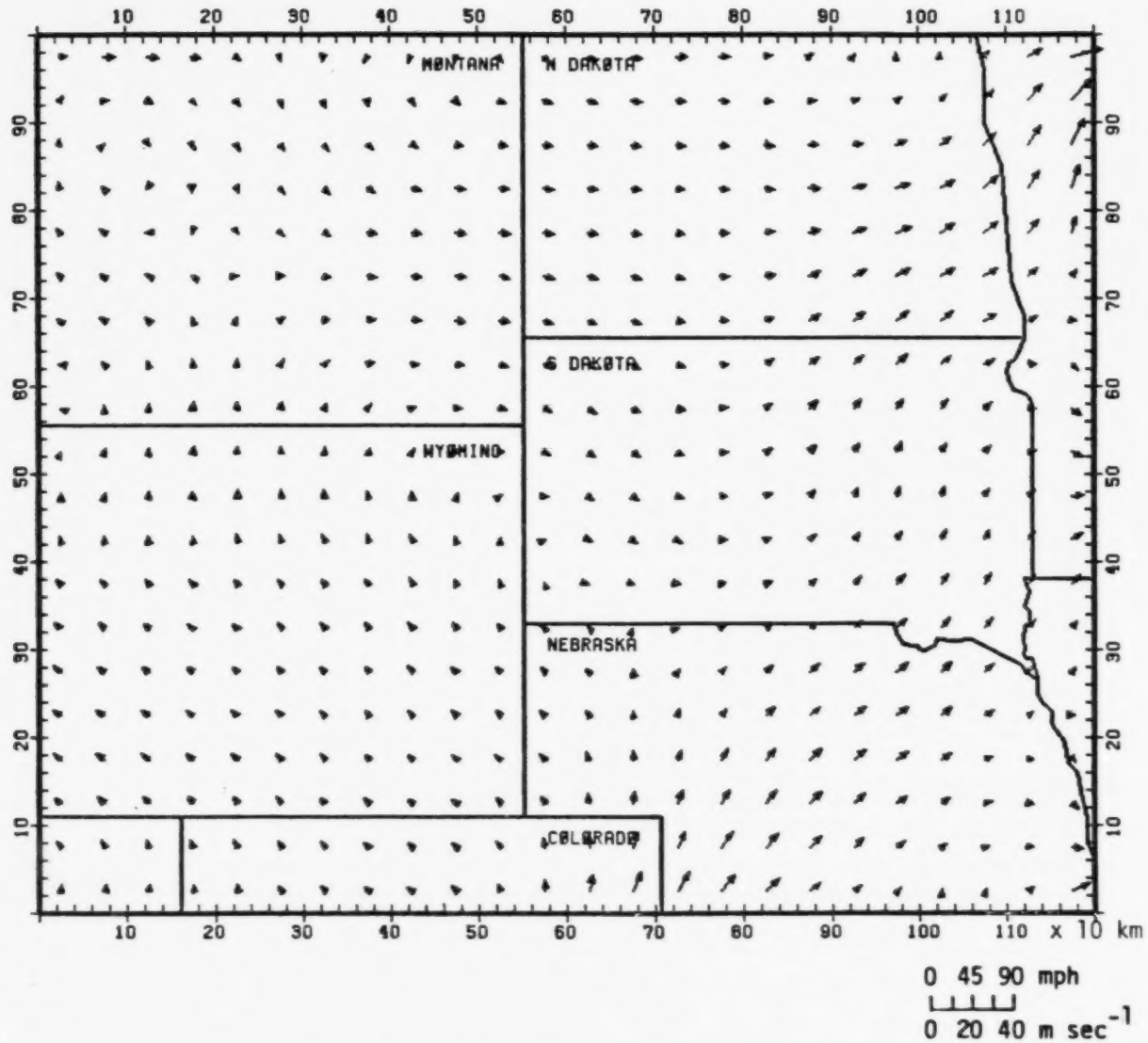

FIGURE 30. WIND VECTORS GENERATED BY A BICUBIC SPLINE FIT OF GEOPOTENTIAL HEIGHT DATA FOR 1700 MST ON 4 APRIL 1976

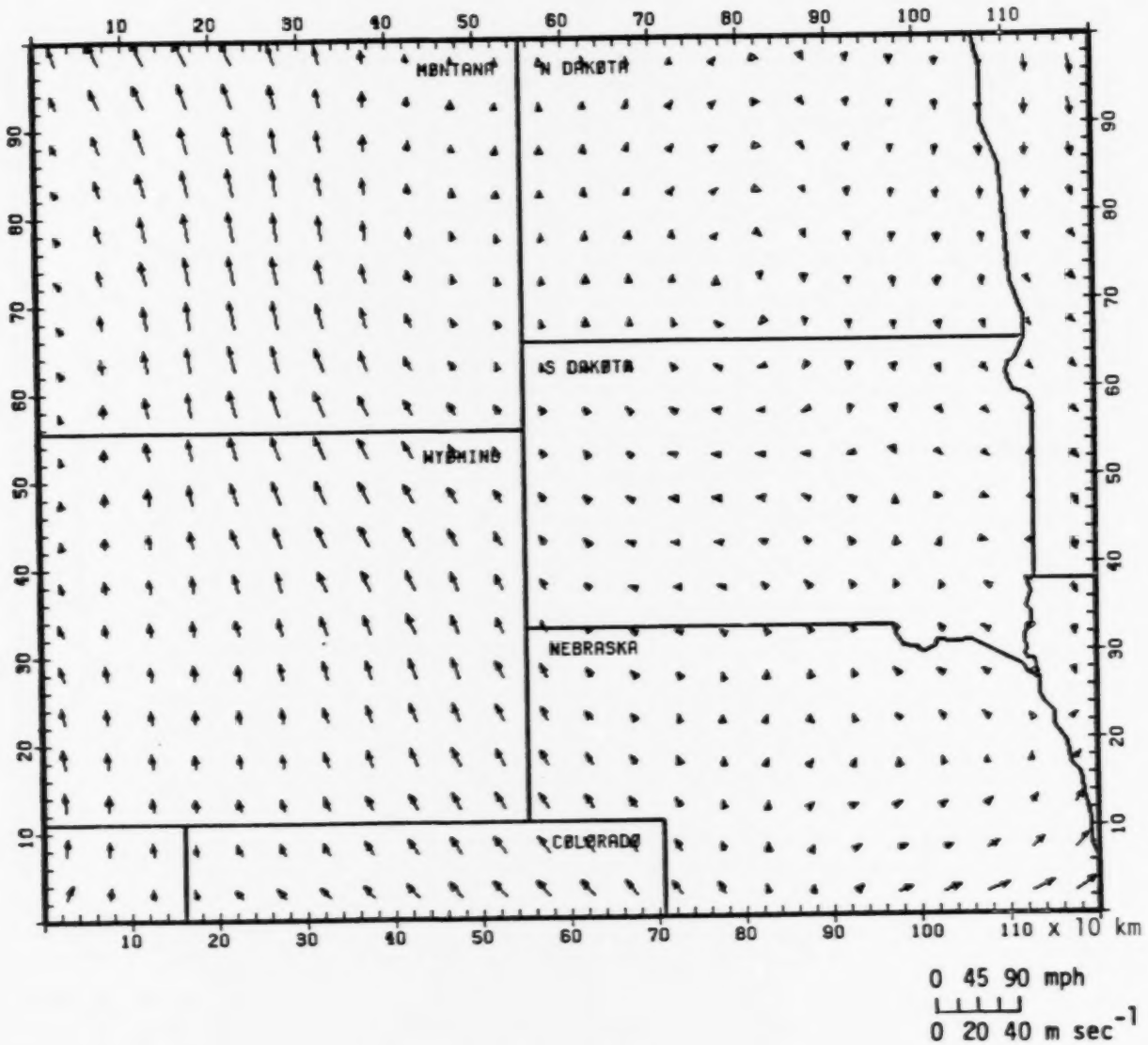

FIGURE 31. WIND VECTORS GENERATED BY A BICUBIC SPLINE FIT OF GEOPOTENTIAL HEIGHT DATA FOR 1700 MST ON 5 APRIL 1976

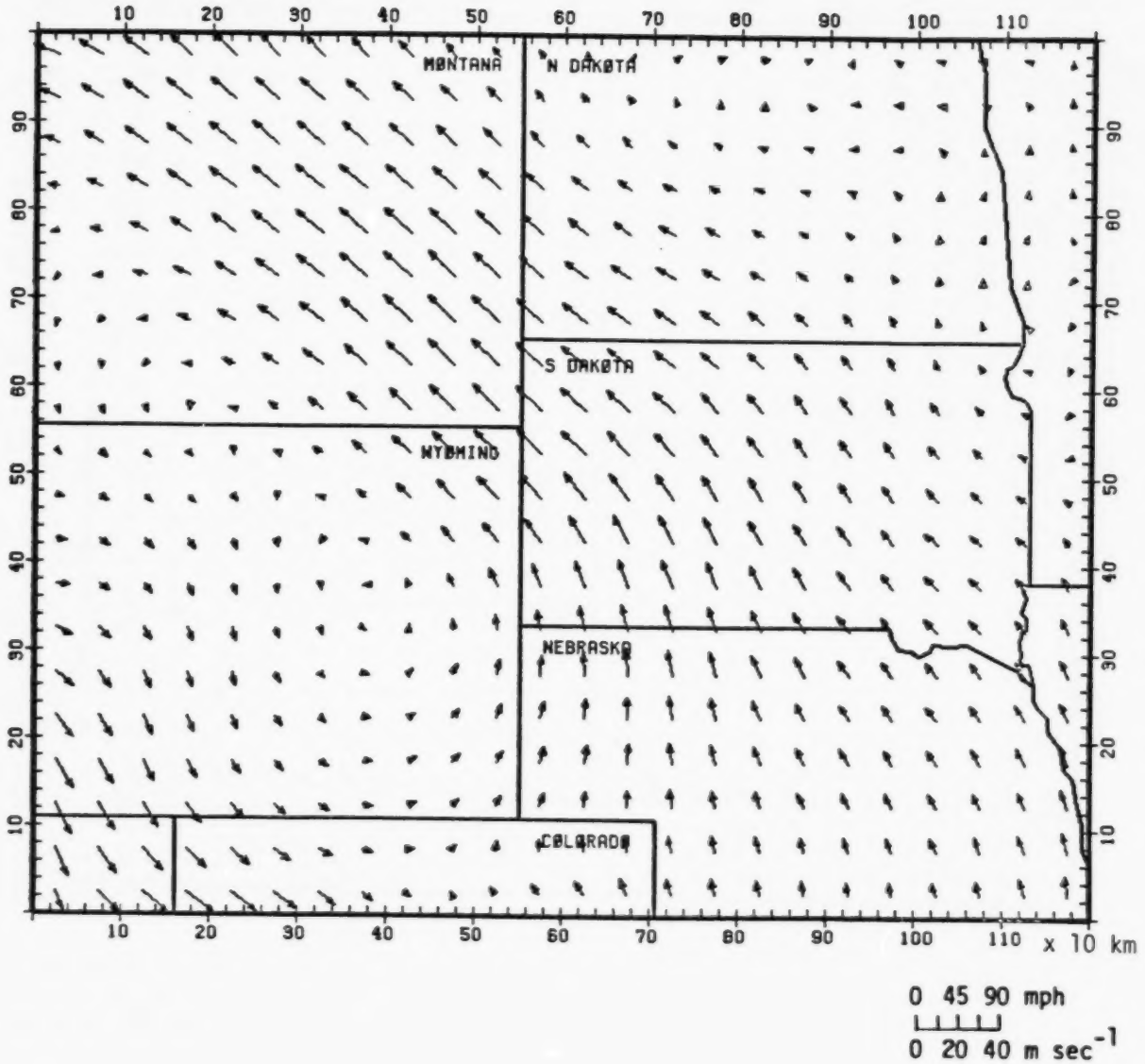

FIGURE 32. WIND VECTORS GENERATED BY A BICUBIC SPLINE FIT OF GEOPOTENTIAL HEIGHT DATA FOR 1700 MST ON 6 APRIL 1976

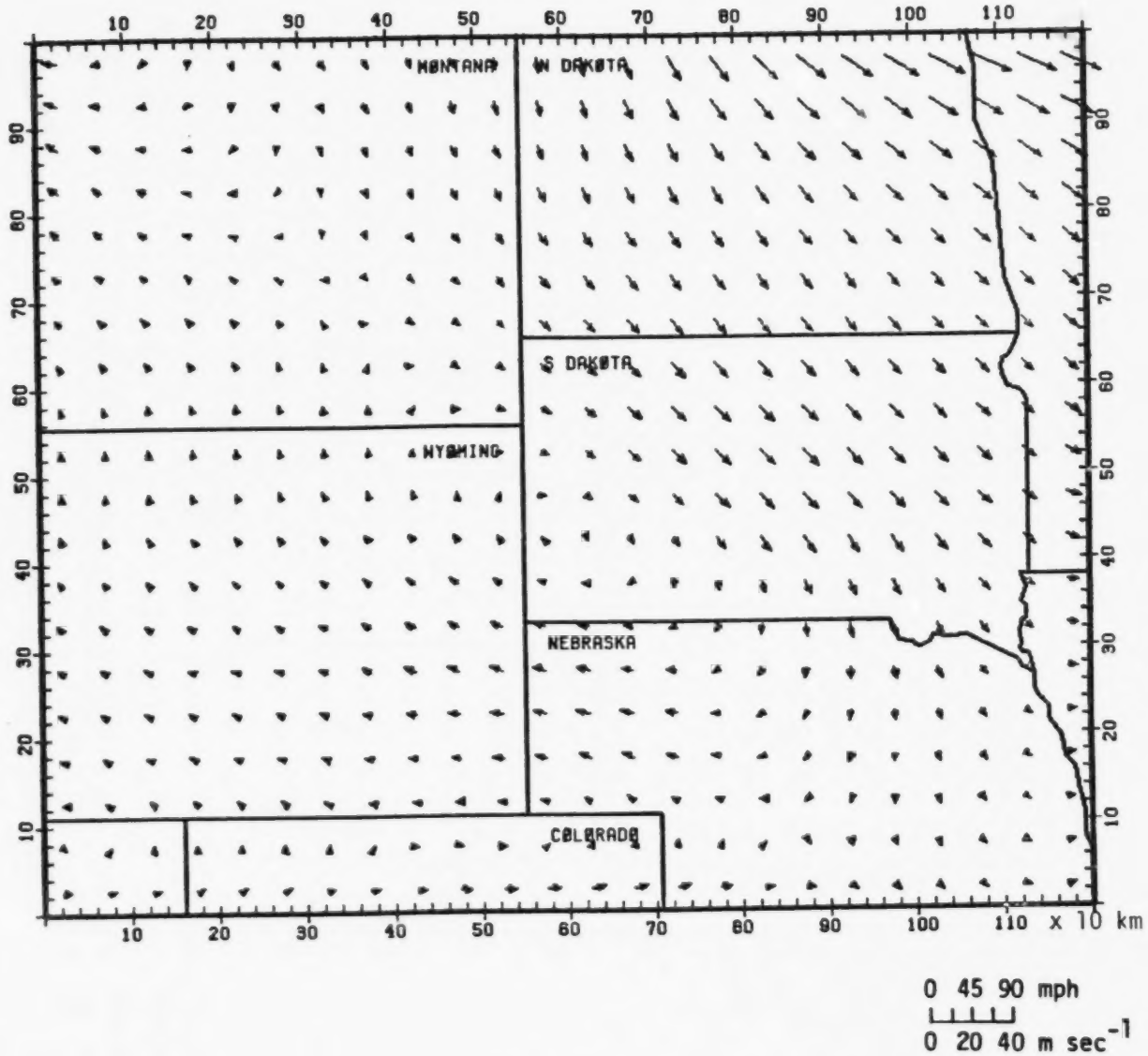

FIGURE 33. WIND VECTORS GENERATED BY A BICUBIC SPLINE FIT OF GEOPOTENTIAL HEIGHT DATA FOR 500 MST ON 9 JULY 1975

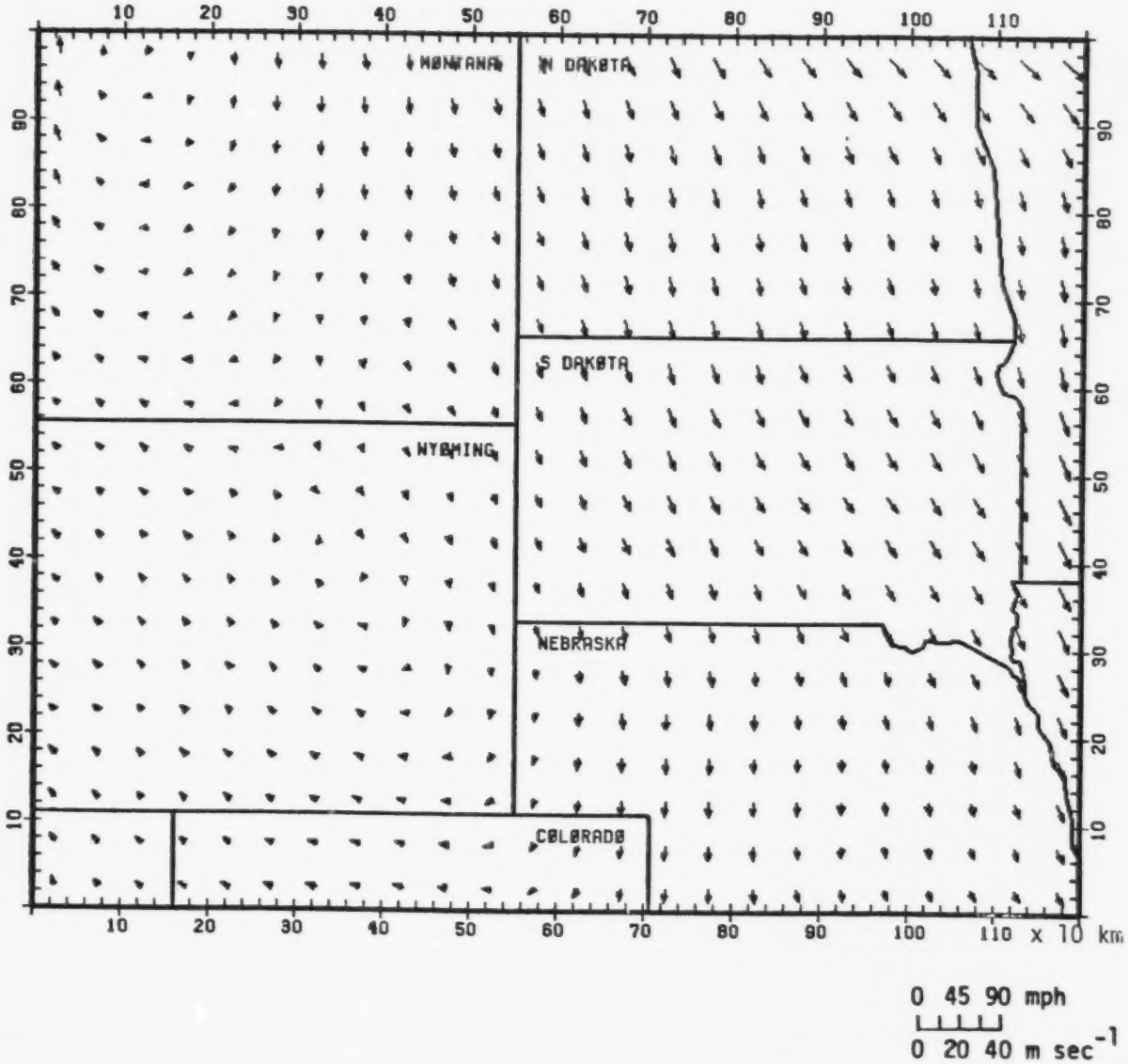

FIGURE 34. WIND VECTORS GENERATED BY A BICUBIC SPLINE FIT OF GEOPOTENTIAL HEIGHT DATA FOR 500 MST ON 10 JULY 1975

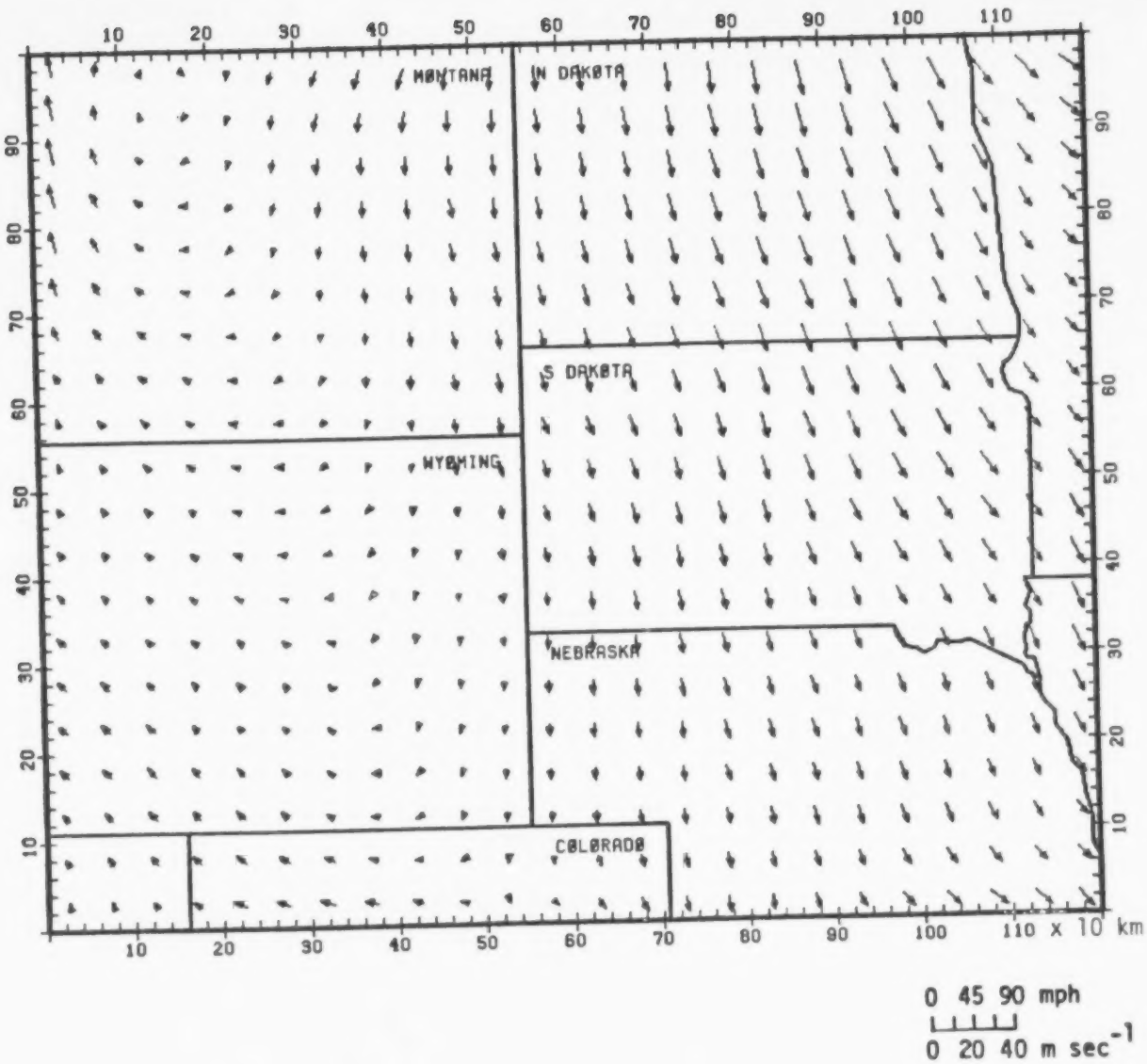

FIGURE 35. WIND VECTORS GENERATED BY A BICUBIC SPLINE FIT OF GEOPOTENTIAL HEIGHT DATA FOR 500 MST ON 11 JULY 1976

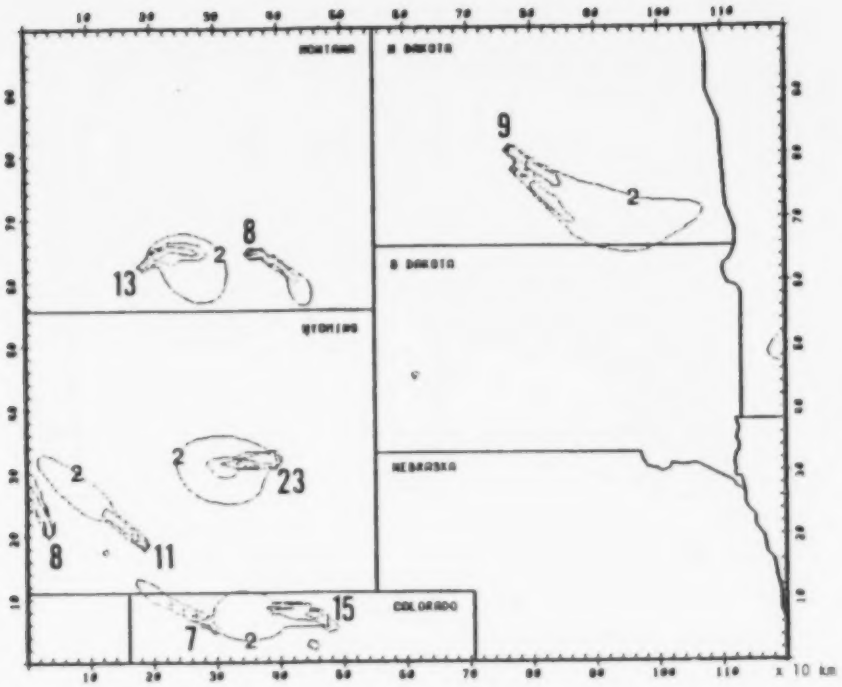

(a) Original Scheme

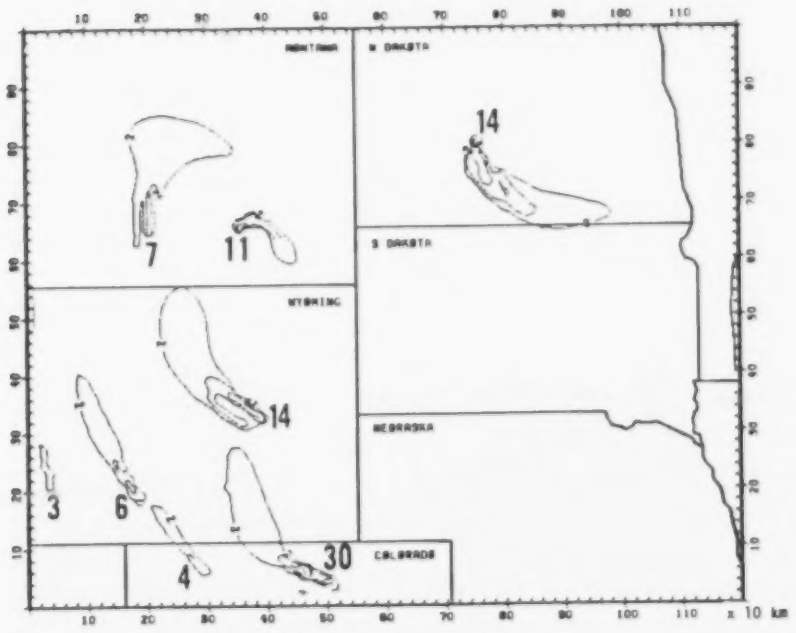

(b) Revised Scheme

FIGURE 36. COMPARISON OF SO_2 CONCENTRATION FIELDS ($\mu g\ m^{-3}$) FOR CASE 1: 500 TO 800 MST ON 5 APRIL 1976

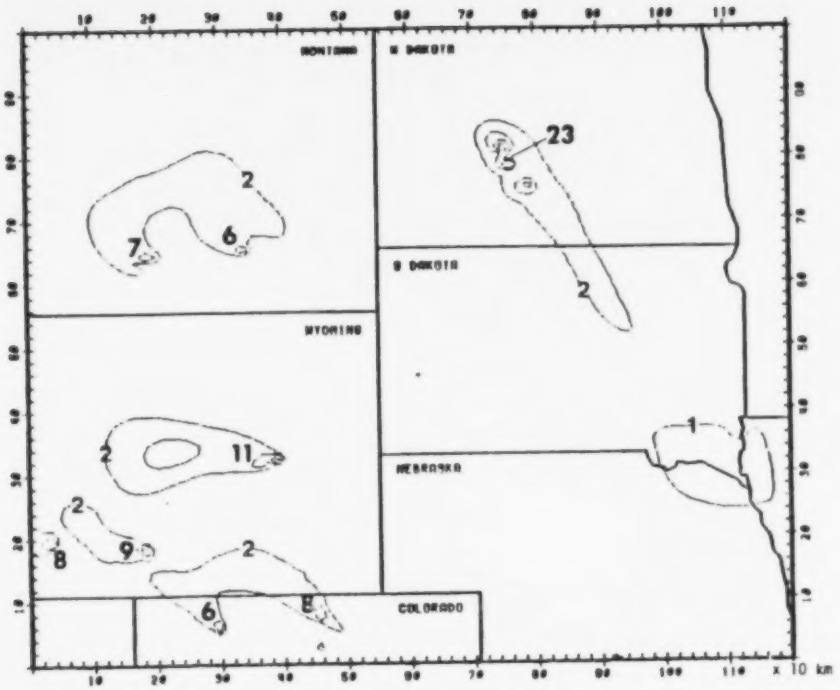

(a) Original Scheme

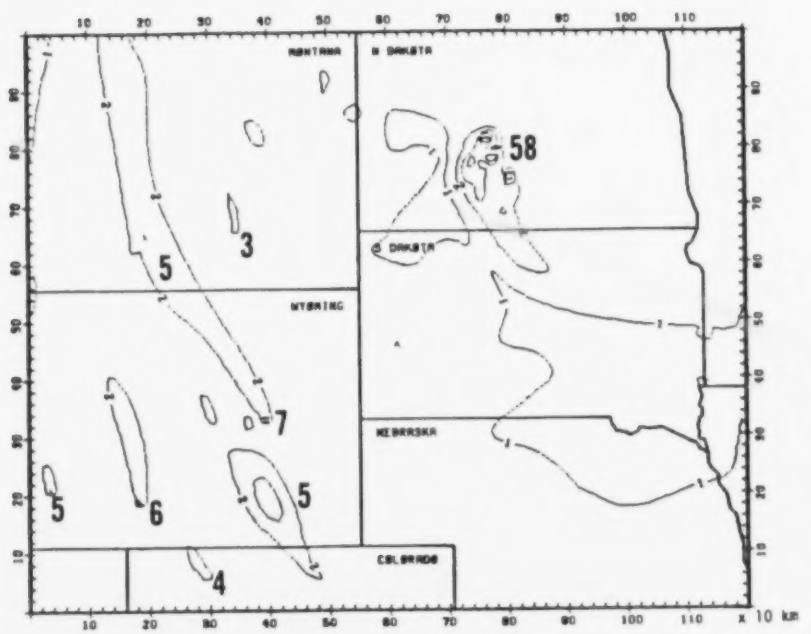

(b) Revised Scheme

FIGURE 37. COMPARISON OF SO_2 CONCENTRATION FIELDS ($\mu g\ m^{-3}$) FOR CASE 1: 1700 TO 2000 MST ON 5 APRIL 1976

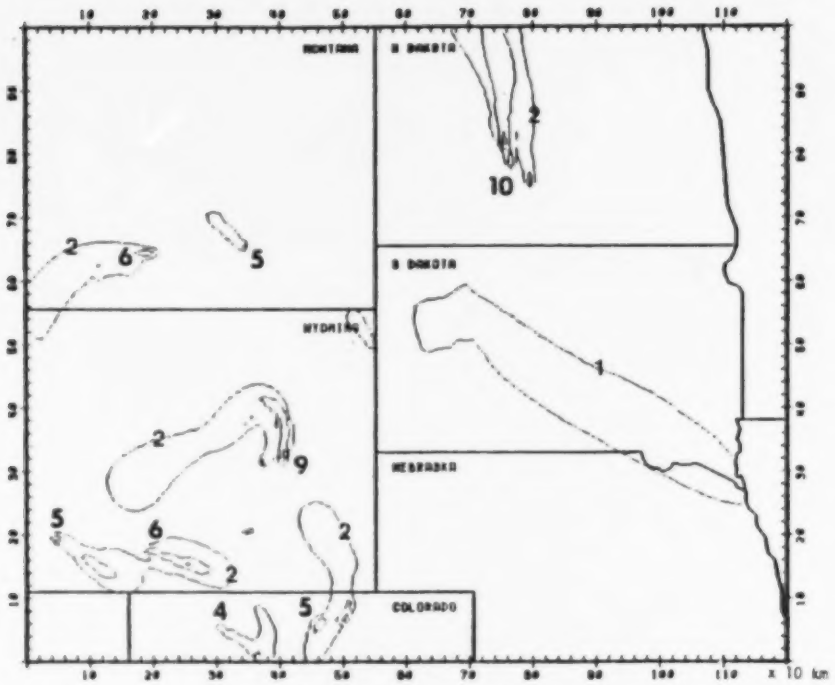

(a) Original Scheme

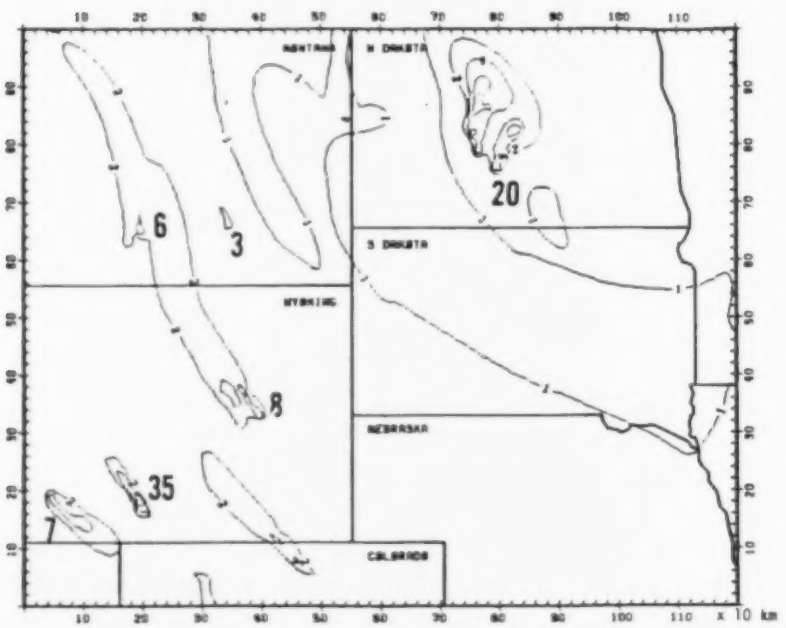

(b) Revised Scheme

FIGURE 38. COMPARISON OF SO_2 CONCENTRATION FIELDS ($\mu g\ m^{-3}$) FOR CASE 1: 800 TO 1100 MST ON 6 APRIL 1976

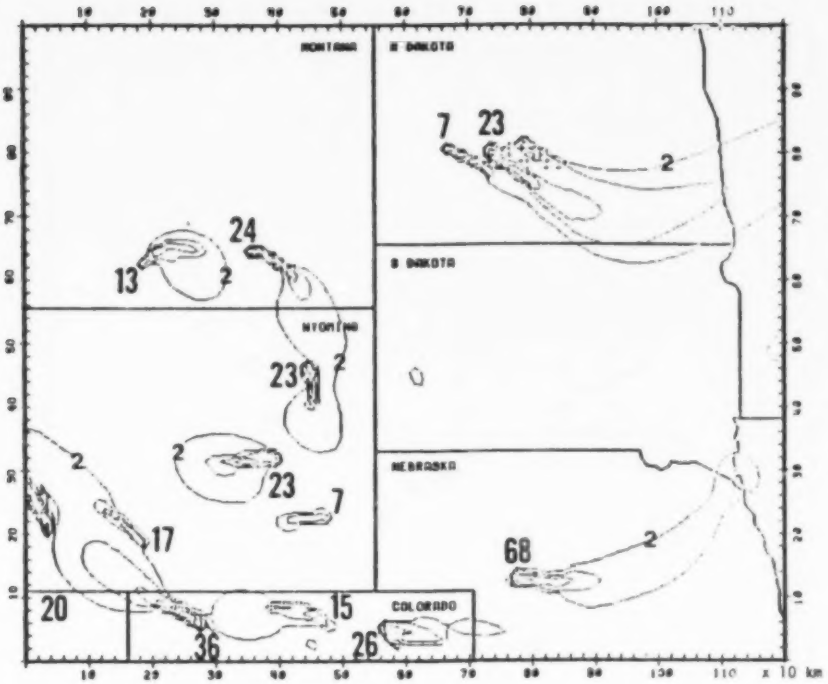

(a) Original Scheme

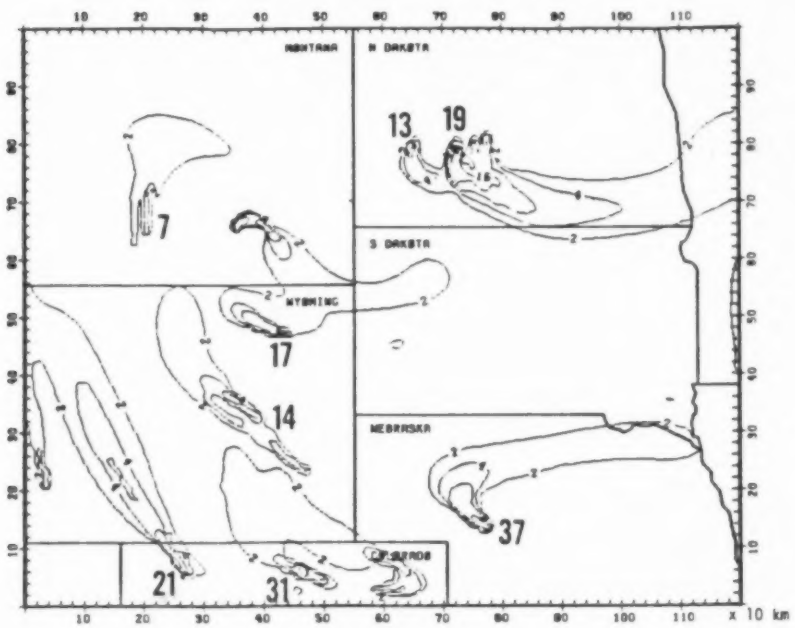

(b) Revised Scheme

FIGURE 39. COMPARISON OF SO_2 CONCENTRATION FIELDS ($\mu g\ m^{-3}$) FOR CASE 2: 500 TO 800 MST ON 5 APRIL 1976

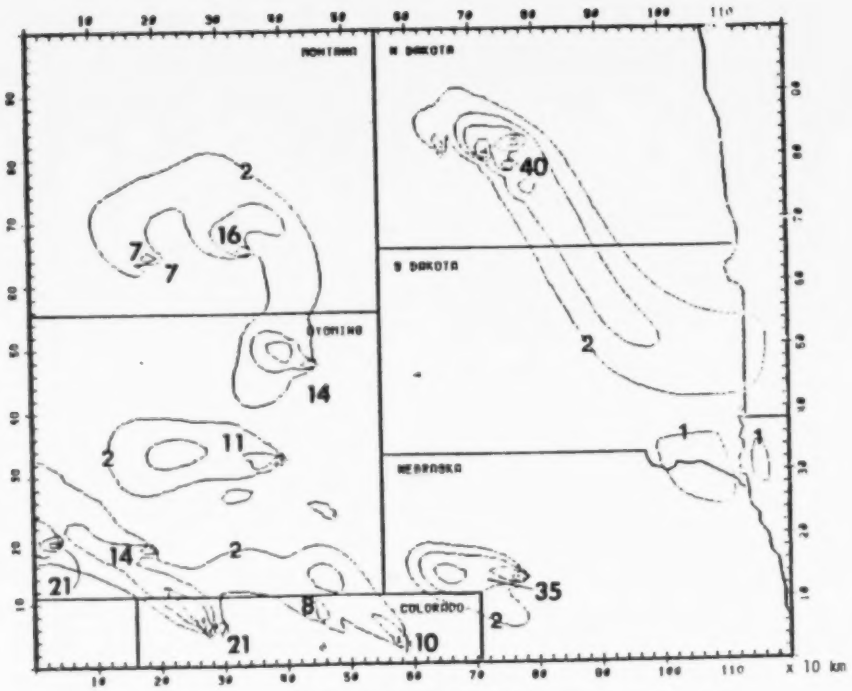

(a) Original Scheme

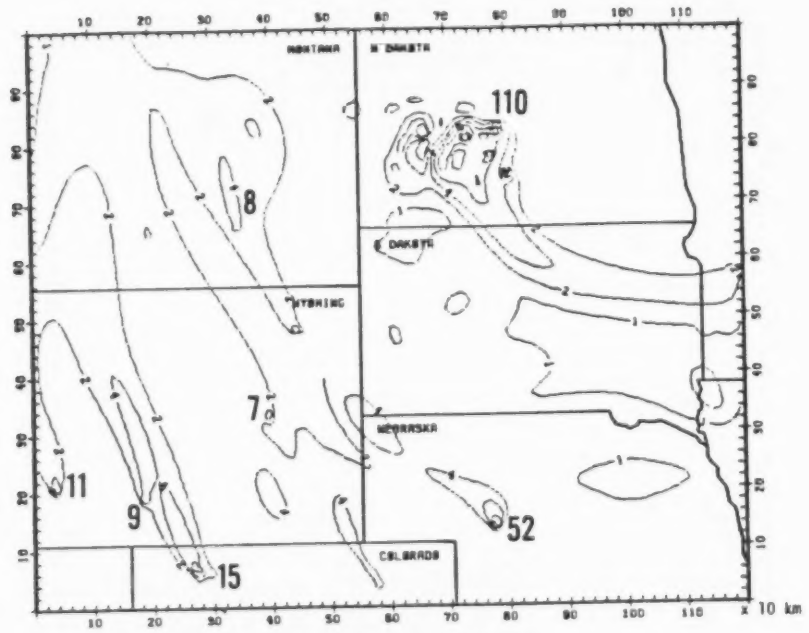

(b) Revised Scheme

FIGURE 40. COMPARISON OF SO_2 CONCENTRATION FIELDS ($\mu g\ m^{-3}$) FOR CASE 2: 1700 TO 2000 MST ON 5 APRIL 1976

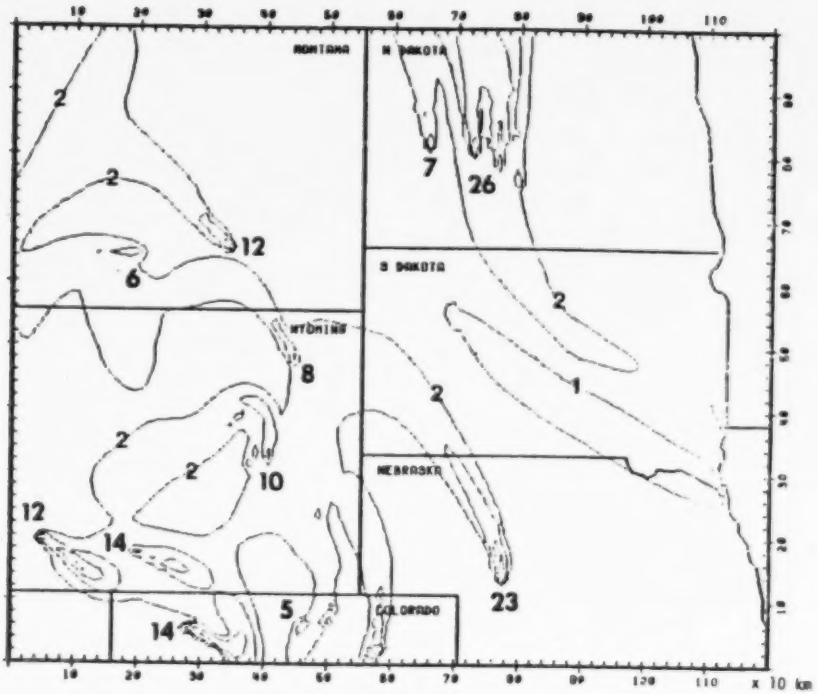

(a) Original Scheme

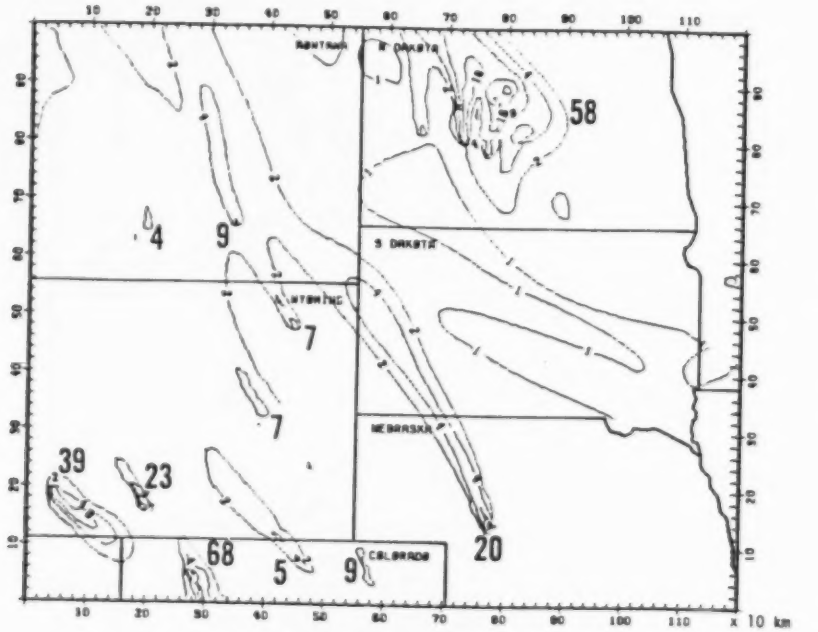

(b) Revised Scheme

FIGURE 41. COMPARISON OF SO_2 CONCENTRATION FIELDS ($\mu g\ m^{-3}$) FOR CASE 2: 800 TO 1100 MST ON 6 APRIL 1976

computed by the new scheme and the measured mixing height data. In the original simulations, the appropriate seasonally averaged mixing height data were used for the three meteorological scenarios. Measured mixing heights at 12-hour intervals for the period of time for each of the three scenarios were obtained. These data were interpolated to three-hour intervals. A constant value for horizontal diffusivity was used in the original simulation, whereas the newly developed algorithm for determining horizontal eddy diffusivity was used in the present study. Thus, in the new simulations, horizontal diffusivity is variable in time and space. The wind field in the mixed layer was also calculated, so that it now corresponds to the geostrophic wind on the 850-mb weather maps. The reader is reminded that meteorological scenarios are not climatologically representative of the given seasons.

A. ANALYSIS OF THE EFFECT OF THE NEW CHARACTERIZATION SCHEME

It was found that dispersion of pollutants on the mesoscale is sensitive to variation of the horizontal eddy diffusivity parameter. In particular, decreasing the horizontal diffusivity decreased the size of the plumes far downstream from the source. The horizontal diffusivity fields resulting from the new characterization scheme for the spring scenario have values ranging from 5×10^3 m^2 $sec^{-1} \leq K_H \leq 10^4$ m^2 sec^{-1}. Since a constant value of 10^4 m^2 sec^{-1} was used for horizontal diffusivity in the original simulations, the diffusivity field was not expected to change drastically the dispersion of pollutants in the worst case, i.e., the spring scenario.

The wind fields constructed using the new characterization scheme differ, however, considerably from those used in the original analysis. The effect of the new wind field is illustrated in Figure 37, which shows a significantly greater buildup of SO_2 near the sources in North Dakota. The diffusivity and mixing height have not varied enough to account for such a change. Owing to the weak geopotential height gradient in that region, the new mixing layer winds are weak, as shown in Figure 38. As a result, transport of pollutants to downwind areas is quite limited, and it causes a concentration buildup in the North Dakota region. The computed maximum concentration in that region is more than double that in the original simulation.

B. AIR QUALITY ANALYSIS

The following three subsections discuss the effect of the new scheme for characterizing wind and diffusivity fields on the computed concentration distributions.

1. Spring Scenario

The effect of the 1986 emissions on air quality in the spring scenario are presented in Figures 39 through 41. In general, pollutants are transported only a short distance in the southwest and northeast portions of the modeling region in the new simulations, resulting in greater pollutant buildup. They are transported a greater distance in the northwest to southeast strip of the region, which permits better mixing and lower concentrations of pollutants. In the northeast section, three-hour-average concentrations exceed 8 $\mu g\ m^{-3}$ at distances on the order of 100 km downwind of the sources. Elsewhere, SO_2 concentrations are greater than 2 $\mu g\ m^{-3}$, but since the pollutants are evenly dispersed, concentrations rarely exceed 4 $\mu g\ m^{-3}$ except near the source.

2. Winter Scenario

The winter scenario results after 12, 39, and 57 hours of simulation using 1986 emissions are presented in Figures 42 through 44. The mixing heights are approximately one-half their spring values during this winter simulation. In general, the horizontal diffusivity varies over an order of magnitude ranging from 1×10^3 to $1 \times 10^4\ m^2\ sec^{-1}$. The mixing layer winds vary over twice the range of their spring counterparts, reaching maximum speeds close to 30 $m\ sec^{-1}$. The increase in wind speed is the dominant factor in creating the difference between the spring and winter SO_2 concentration fields. After 12 hours, pollutants have traveled up to 500 km from their sources, and concentrations of 8 $\mu g\ m^{-3}$ occur 300 km from point sources in North Dakota. Note that because of the increased wind speeds the computed SO_2 concentrations on 29 January 1976 are significantly lower compared with

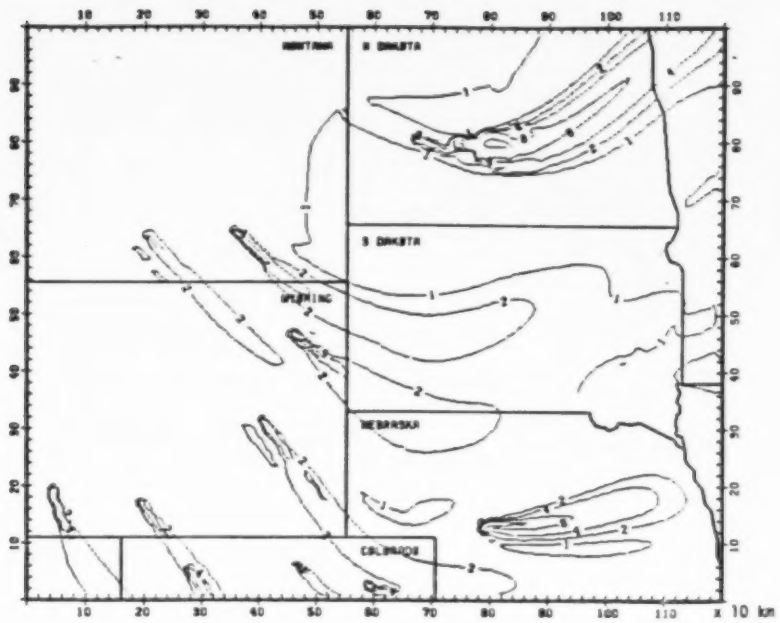

FIGURE 42. SO_2 CONCENTRATION FIELDS ($\mu g\ m^{-3}$) FOR CASE 5 (REVISED SCHEME): 1700 TO 2000 MST ON 27 JANUARY 1976

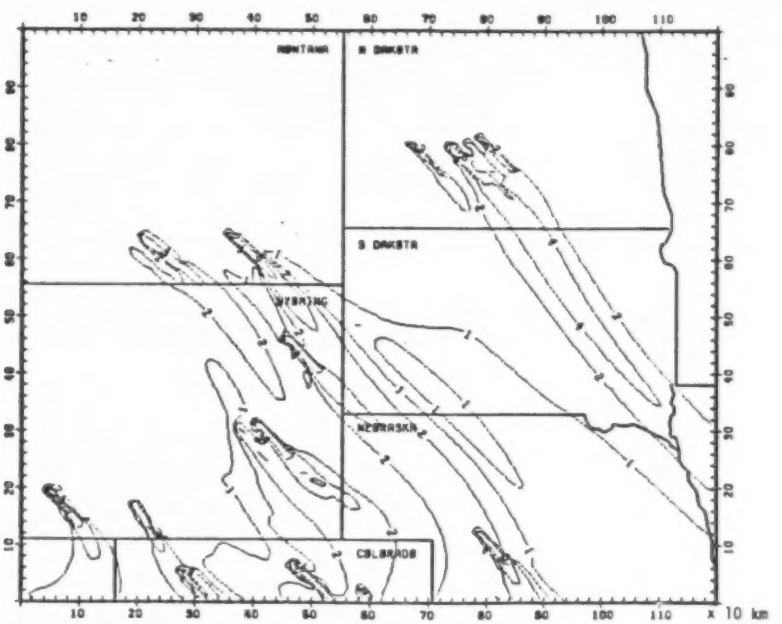

FIGURE 43. SO_2 CONCENTRATION FIELDS ($\mu g\ m^{-3}$) FOR CASE 5 (REVISED SCHEME): 2000 TO 2300 MST ON 28 JANUARY 1976

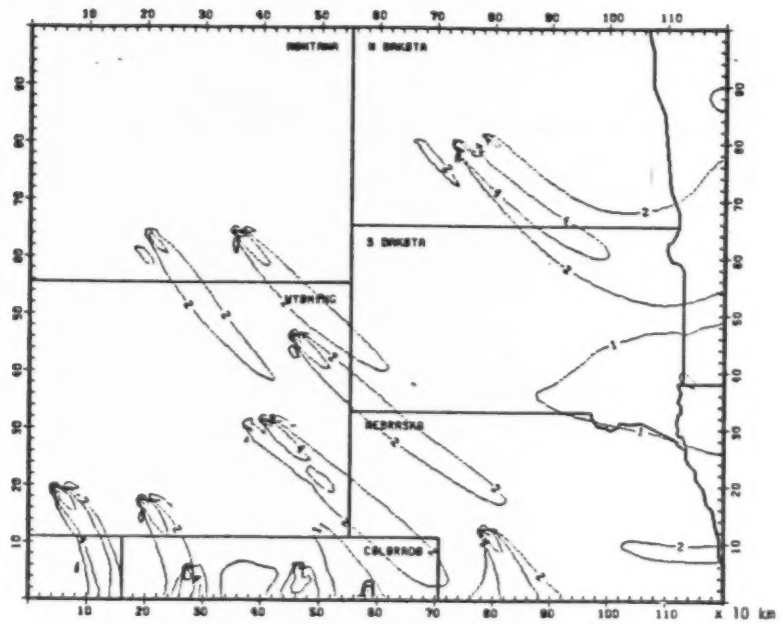

FIGURE 44. SO_2 CONCENTRATION FIELDS ($\mu g\ m^{-3}$) FOR CASE 5 (REVISED SCHEME): 1400 TO 1700 MST ON 29 JANUARY 1976

those on 27 January 1976 and 28 January 1976. After 57 hours of transport and diffusion, SO_2 concentrations are greater than 4 $\mu g\ m^{-3}$ in only a small area.

3. Summer Scenario

The summer scenario results in Figures 45 through 47 show that SO_2 concentrations in that season can reach the spring levels under the proper meteorological conditions. The summer season characteristically has the greatest mixing heights (approximately twice the spring heights) because of the increased surface heating. The mixing heights for the summer scenario are generally above the seasonal average values in the northwest portion of the Great Plains region. Consequently, the summer mixing heights tend to prevent pollution buildup in this area. The diffusivities, however, are slightly lower than the corresponding spring values because of more uniform wind fields. The winds are generally moderate and greater than the spring winds in the eastern half of the region. In the western half of the region, the winds are weak. Unlike the winter winds, the summer mixing layer winds can favor poor transport and therefore high pollutant concentrations. The SO_2 three-hour-average concentrations as a result of the wind field were uniform in the eastern portion of the region and were equal to their spring scenario counterparts in the western portion of the region. Again, because of the increase in wind speeds, pollutant concentrations remained below 4 $\mu g\ m^{-3}$ through most of the region after 57 hours of simulation.

C. SENSITIVITY STUDY OF THE SO_2/SO_4 CONVERSION RATE

The concentrations of SO_2 and SO_4 after 51 hours of simulation for the spring scenario with a 1 percent SO_2/SO_4 conversion rate are shown in Figures 48 and 49 for 1976 and 1986 emissions. When a 0.3 percent conversion rate was used in the original model, the resulting SO_4 values were not much higher than background concentrations. As shown in Figure 48, SO_4 pollutant concentrations were generally on the order of 4 $\mu g\ m^{-3}$ for

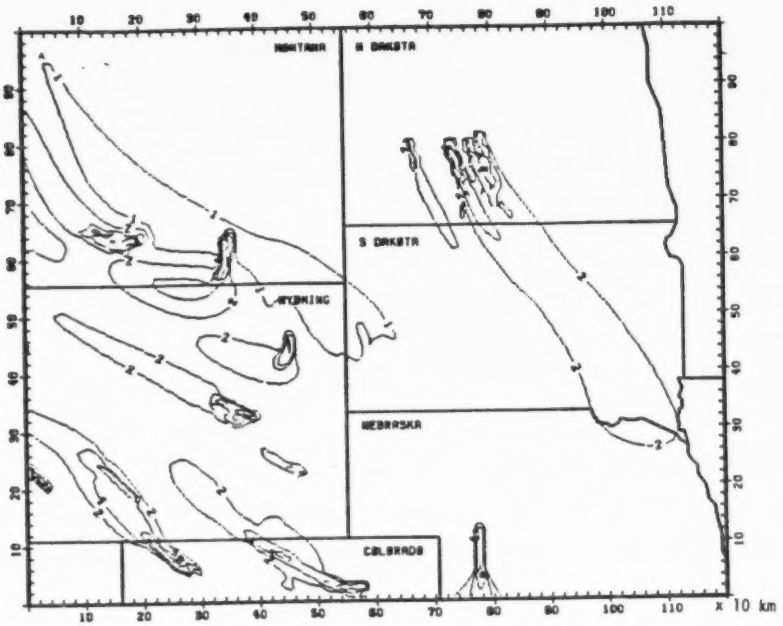

FIGURE 45. SO_2 CONCENTRATION FIELDS ($\mu g\ m^{-3}$) FOR CASE 6 (REVISED SCHEME): 200 TO 500 MST ON 10 JULY 1975

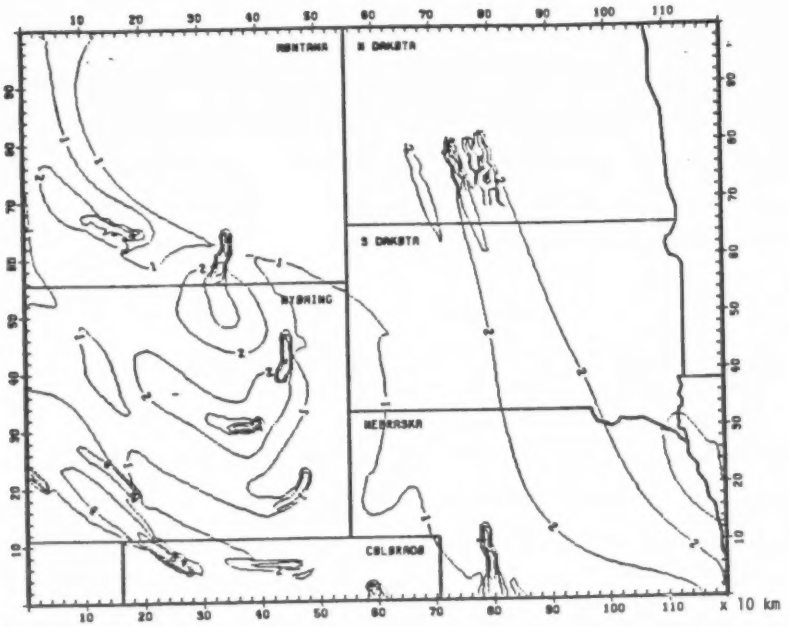

FIGURE 46. SO_2 CONCENTRATION FIELDS ($\mu g\ m^{-3}$) FOR CASE 6 (REVISED SCHEME): 500 TO 800 MST ON 11 JULY 1975

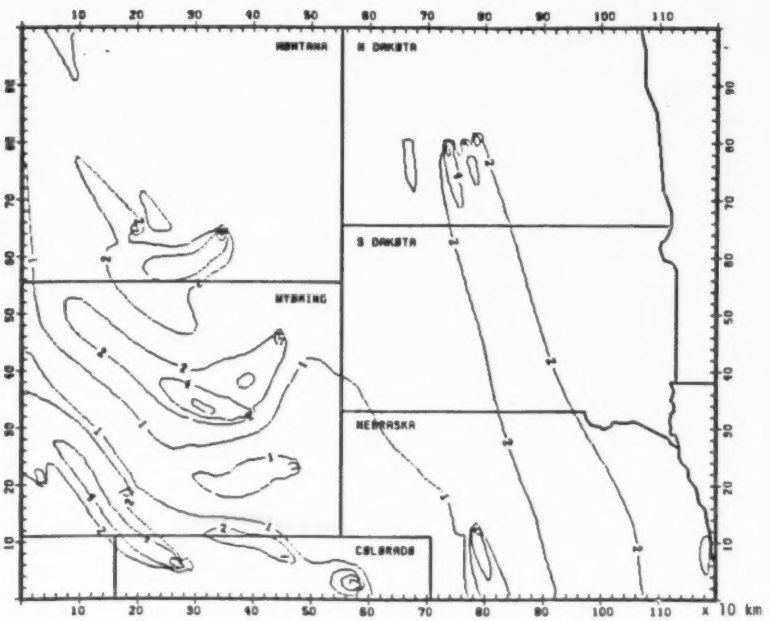

FIGURE 47. SO_2 CONCENTRATION FIELDS ($\mu g\ m^{-3}$) FOR CASE 6 (REVISED SCHEME): 1400 TO 1700 MST ON 11 JULY 1975

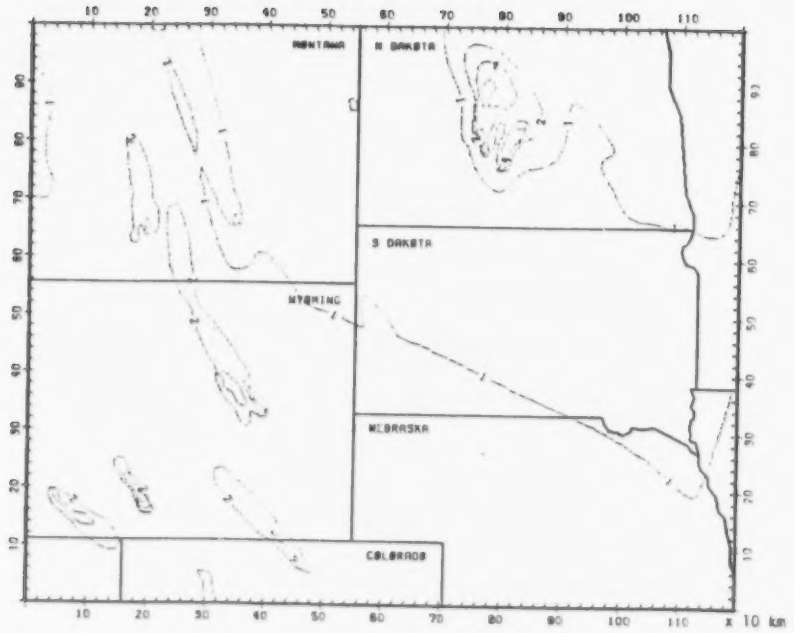

(a) SO_2 Concentration Field

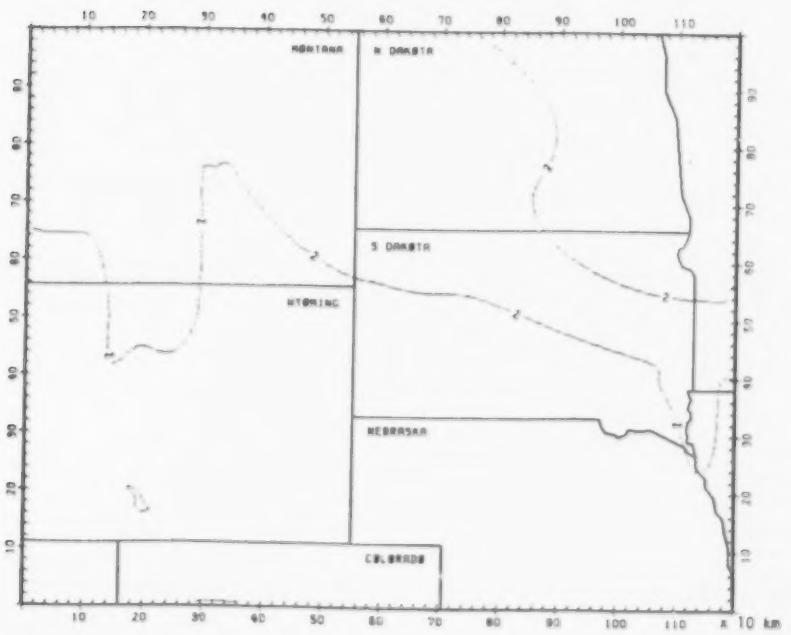

(b) SO_4 Concentration Field

FIGURE 48. CONCENTRATION FIELDS ($\mu g\ m^{-3}$) FOR CASE 3 (REVISED SCHEME): 800 TO 1100 MST ON 6 APRIL 1976

1976 emissions with the higher conversion rate. The effects of the increased conversion rate are more noticeable in the 1986 emissions simulations; the SO_4 concentrations exceed 6 $\mu g\ m^{-3}$ in a small portion of North Dakota, as shown in Figure 49, and are higher than 3 $\mu g\ m^{-3}$ over most of the region. In weak circulations, such as that over North Dakota in the spring scenario, SO_2 conversion to SO_4 is a significant process if the conversion rate is on the order of 1 percent or more because 200 km from the source 30 percent of the SO_2 has been converted to SO_4.

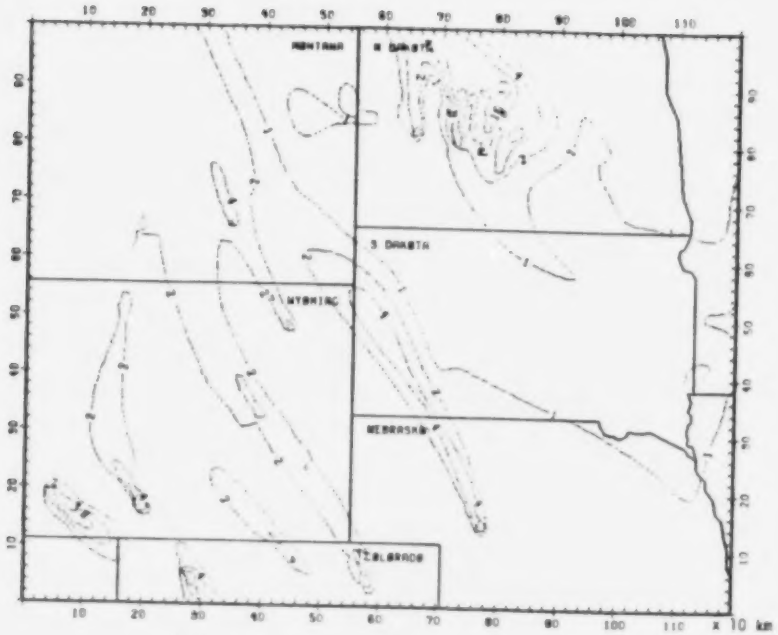

(a) SO_2 Concentration Field

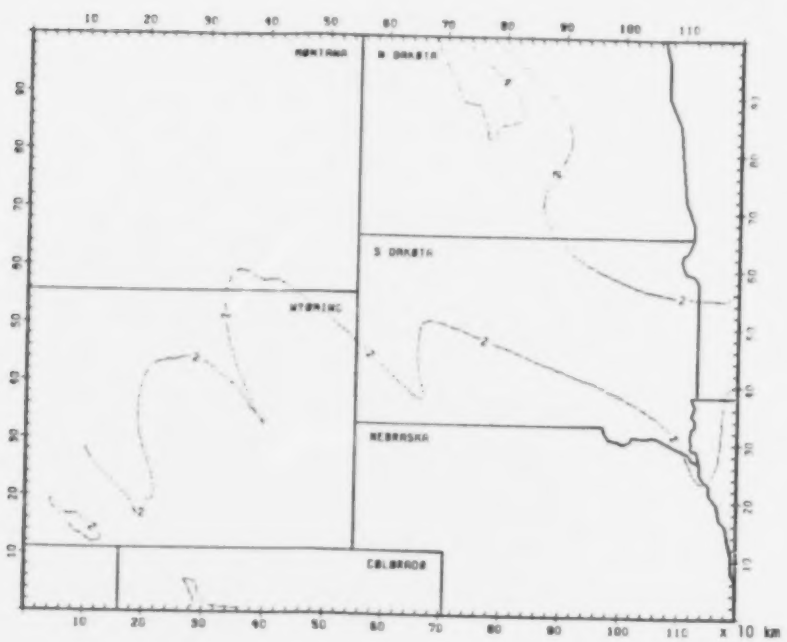

(b) SO_4 Concentration Field

FIGURE 49. CONCENTRATION FIELDS ($\mu g\ m^{-3}$) FOR CASE 4 (REVISED SCHEME): 800 TO 1100 MST ON 6 APRIL 1976

APPENDIX
SIMULATION RESULTS

APPENDIX
SIMULATION RESULTS

This appendix presents the complete set of simulation results summarized in the main report. The long range air pollution model with temporally and spatially varying horizontal diffusivity, geostrophic mixing layer winds, and improved mixing depth data was used in six sets of simulations, which are identified in the following tabulation:

Case	Meteorology Scenario	Emissions Scenario	SO_2-to-SO_4 Conversion Rate (percent per hour)	Figure Numbers
1	4-7 April 1975	1976	0.3%	A-1 through A-6
2	4-7 April 1976	1986	0.3	A-7 through A-12
3	4-7 April 1976	1976	1.0	A-13 through A-18
4	4-7 April 1976	1986	1.0	A-19 through A-24
5	27-31 January 1976	1986	1.0	A-25 through A-30
6	9-11 July 1975	1986	1.0	A-31 through A-36

The isopleth maps show predicted three-hour-average SO_2 concentrations and the accompanying SO_4 concentrations (both in $\mu g\ m^{-3}$). Isopleths were drawn for concentrations of 1, 2, 4, 8, ..., $\mu g\ m^{-3}$. In these maps, the axes are in units of tens of kilometers; thus, the region of 100 x 120 grid cells is 1000 x 1200 km.

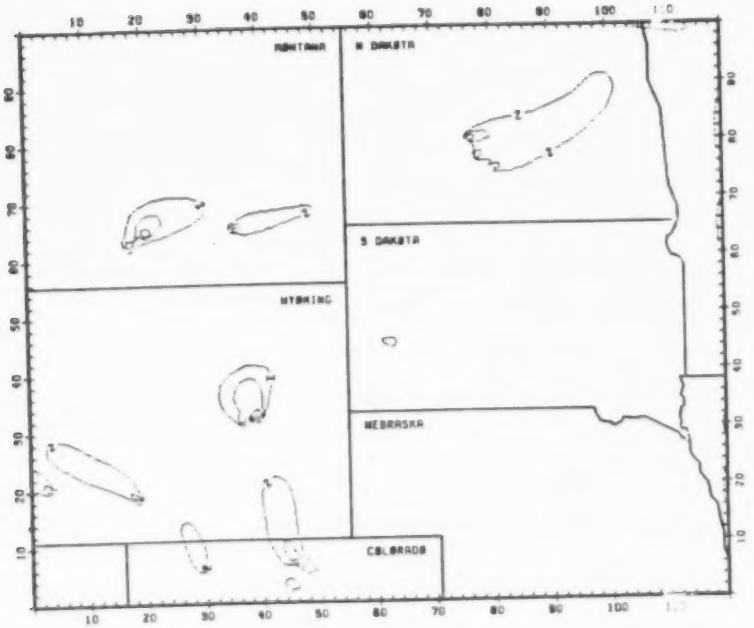

(a) SO_2

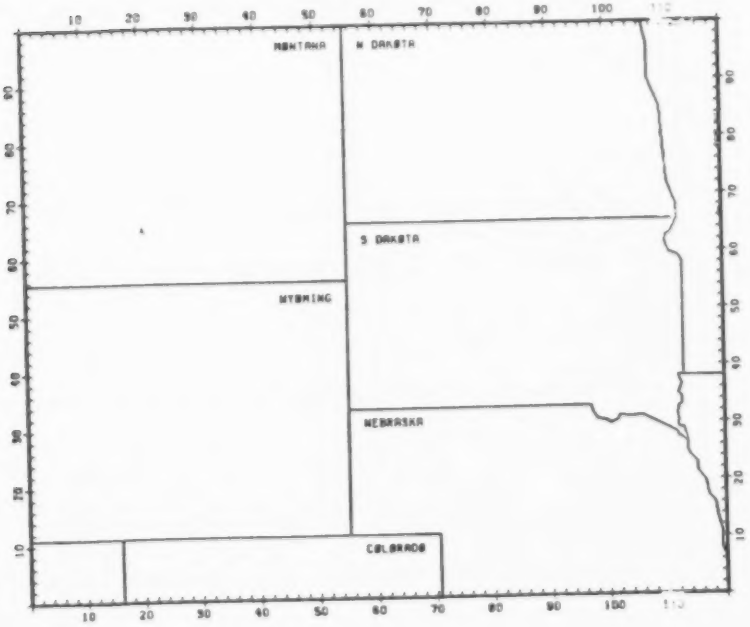

(b) SO_4

FIGURE A-1. SO_2 AND SO_4 CONCENTRATIONS FOR CASE 1: 1700 TO 2000 MST ON 4 APRIL 1976

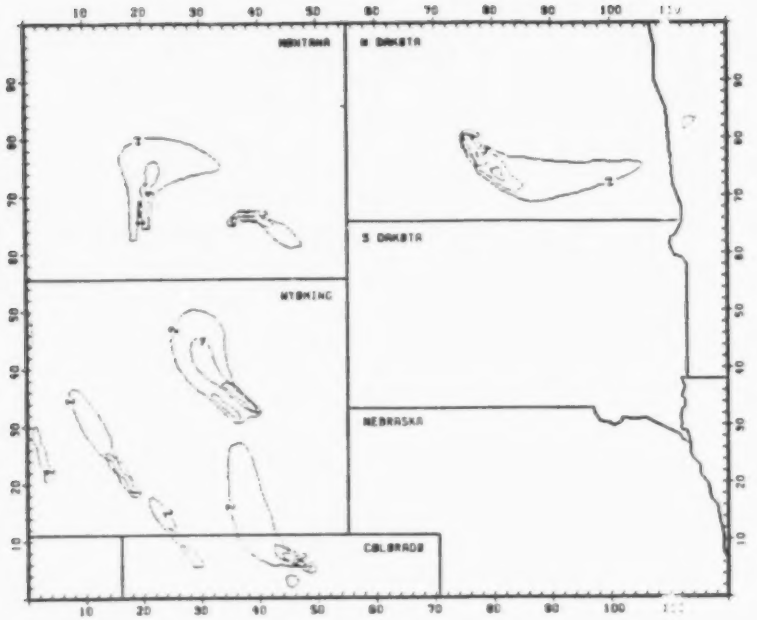

(a) SO_2

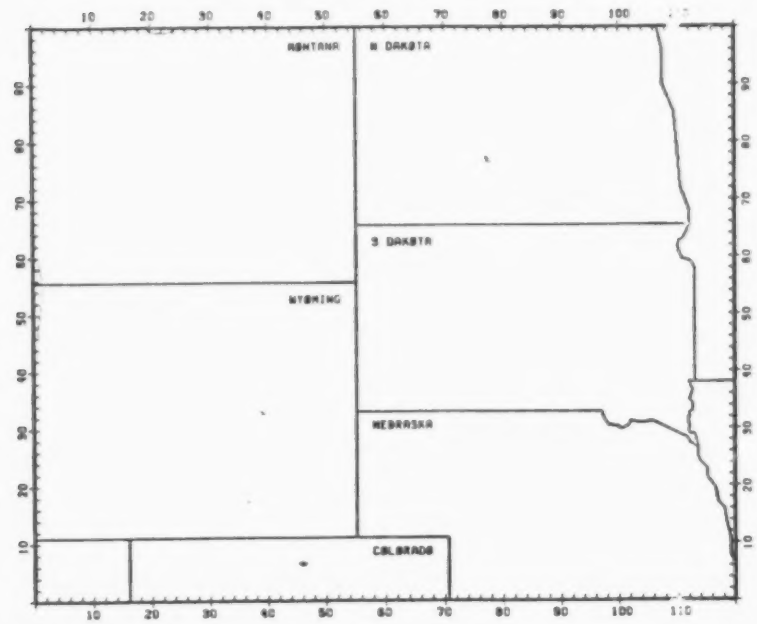

(b) SO_4

FIGURE A-2. SO_2 AND SO_4 CONCENTRATIONS FOR CASE 1: 200 TO 500 MST ON 5 APRIL 1976

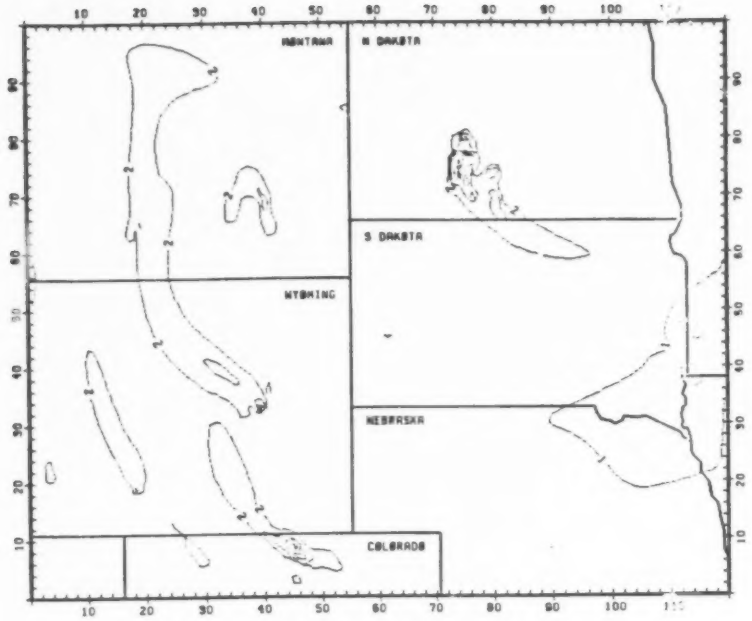

(a) SO_2

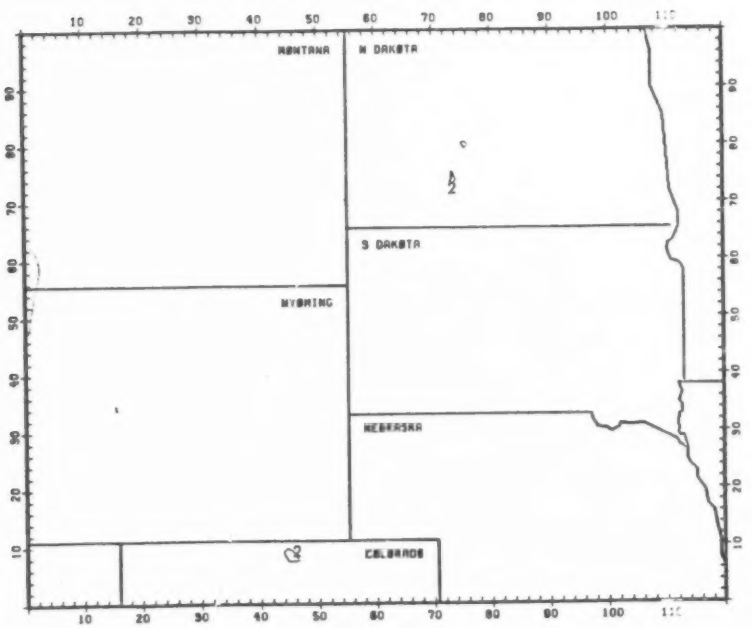

(b) SO_4

FIGURE A-3. SO_2 AND SO_4 CONCENTRATIONS FOR CASE 1: 1100 TO 1400 MST ON 5 APRIL 1976

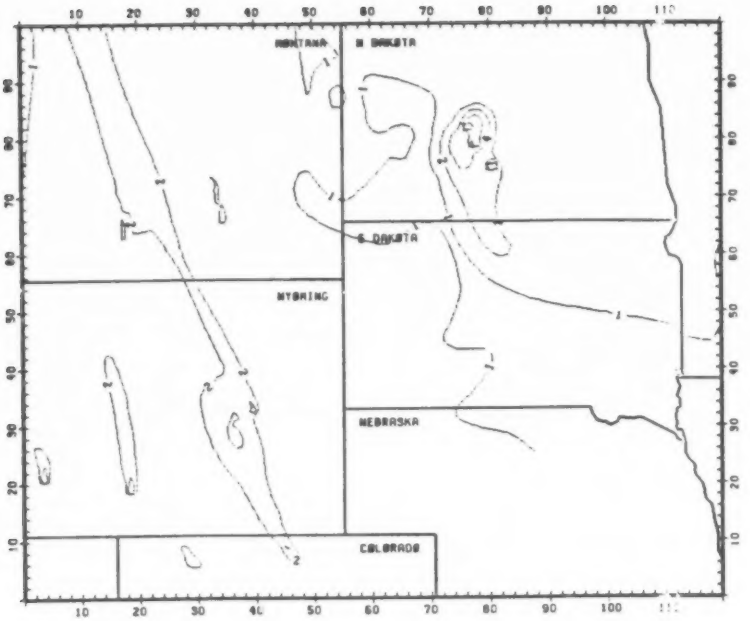

(a) SO_2

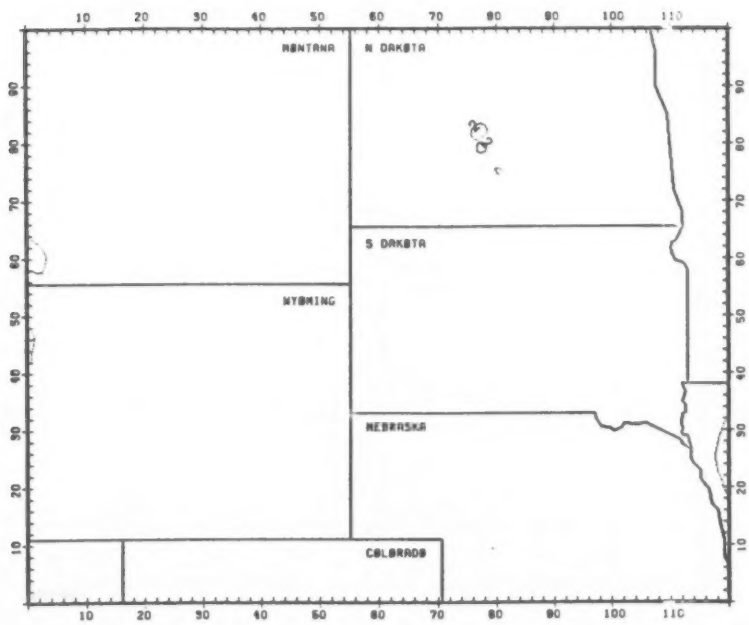

(b) SO_4

FIGURE A-4. SO_2 AND SO_4 CONCENTRATIONS FOR CASE 1: 2000 TO 2300 MST ON 5 APRIL 1976

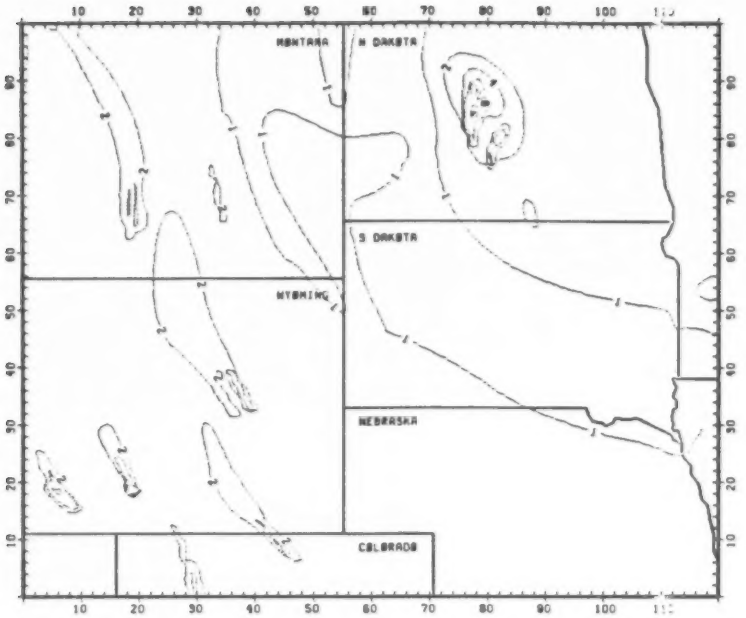

(a) SO_2

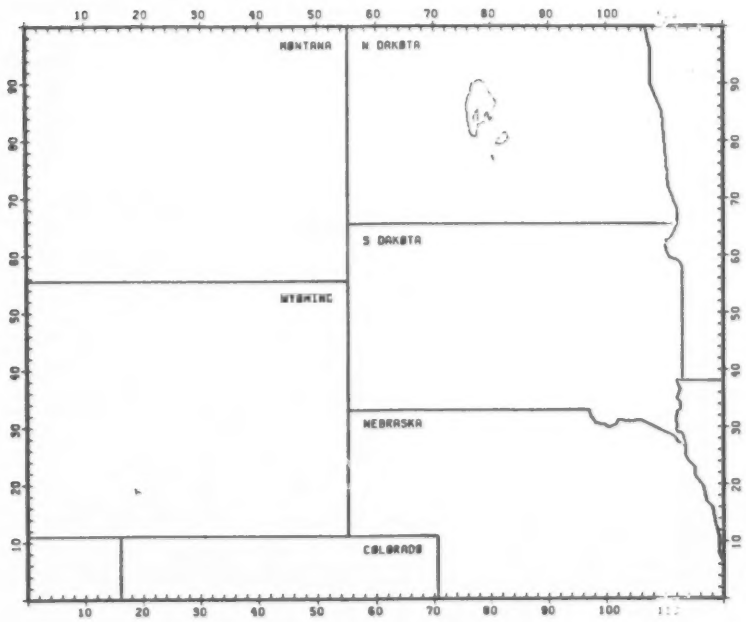

(b) SO_4

FIGURE A-5. SO_2 AND SO_4 CONCENTRATIONS FOR CASE 1: 500 TO 800 MST ON 6 APRIL 1976

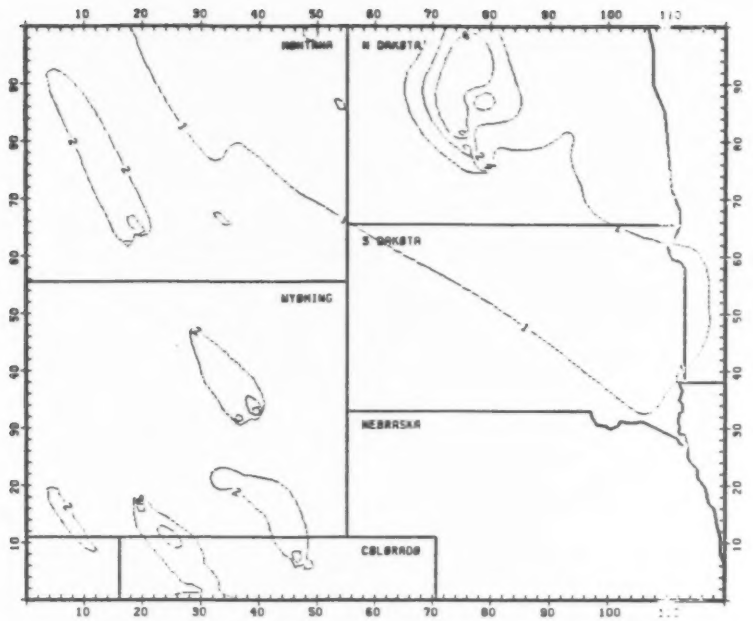

(a) SO_2

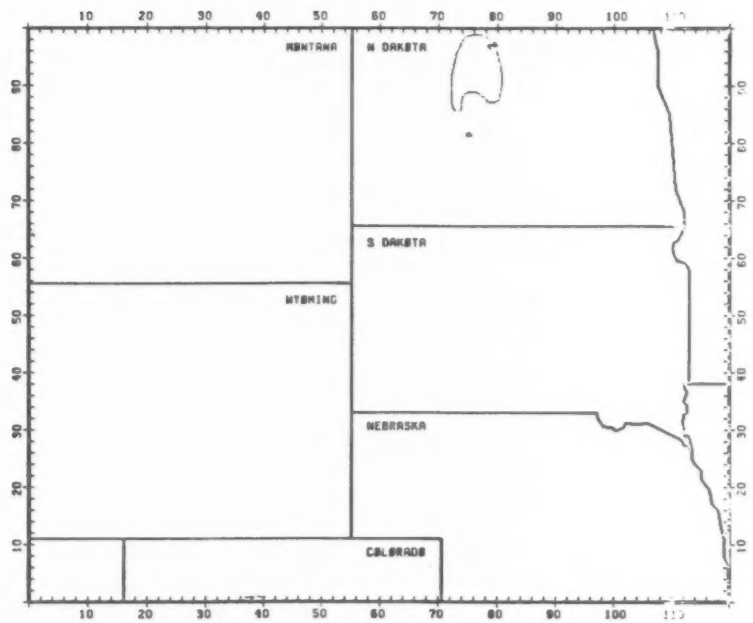

(b) SO_4

FIGURE A-6. SO_2 AND SO_4 CONCENTRATIONS FOR CASE 1: 1400 TO 1700 MST ON 6 APRIL 1976

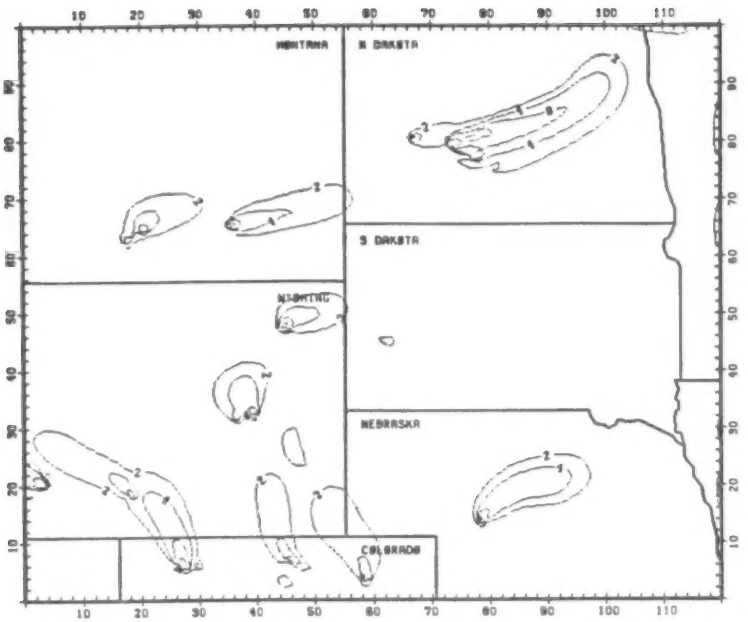

(a) SO_2

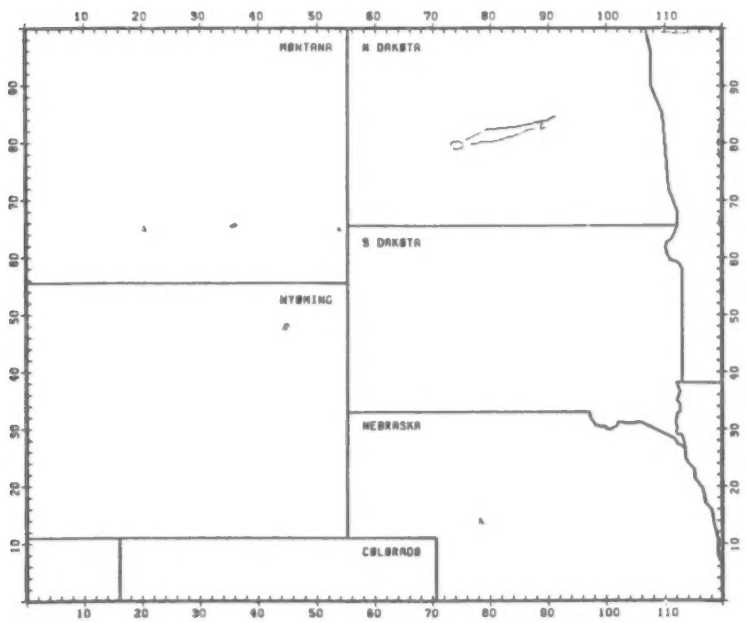

(b) SO_4

FIGURE A-7. SO_2 AND SO_4 CONCENTRATIONS FOR CASE 2: 1700 TO 2000 MST ON 4 APRIL 1976

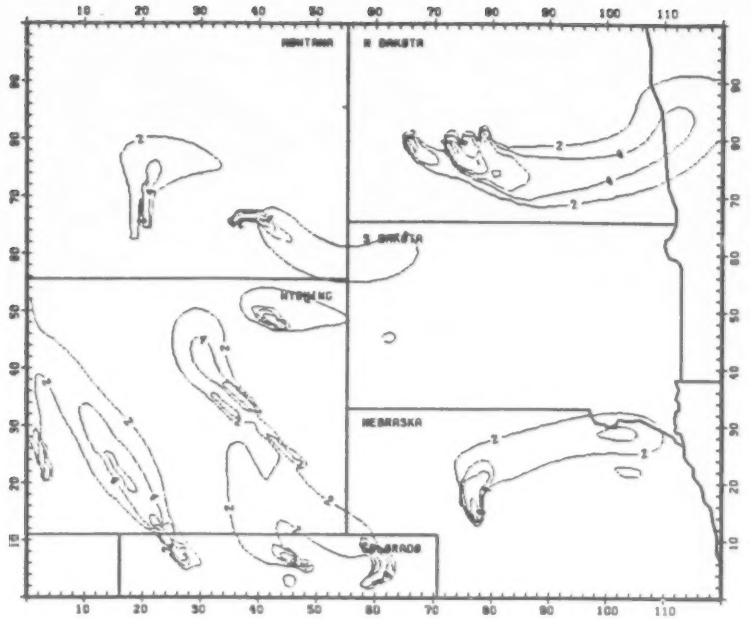

(a) SO_2

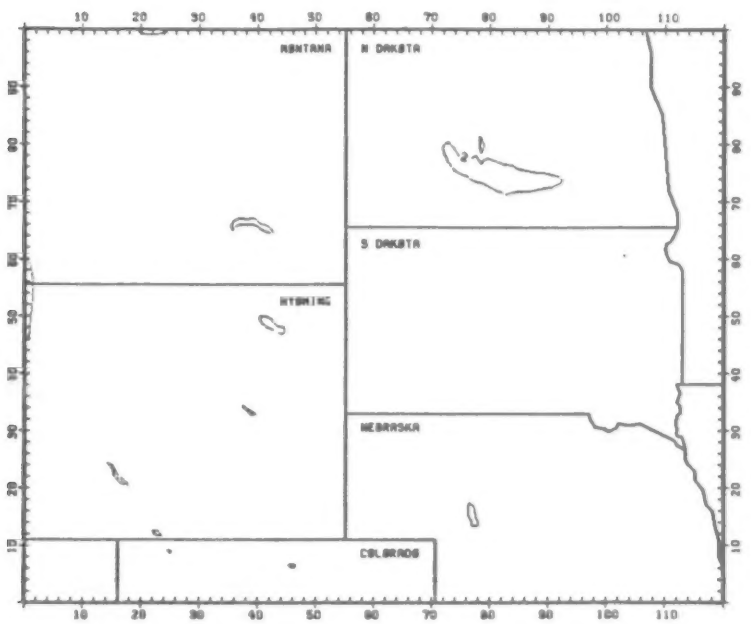

(b) SO_4

FIGURE A-8. SO_2 AND SO_4 CONCENTRATIONS FOR CASE 2: 200 TO 500 MST ON 5 APRIL 1976

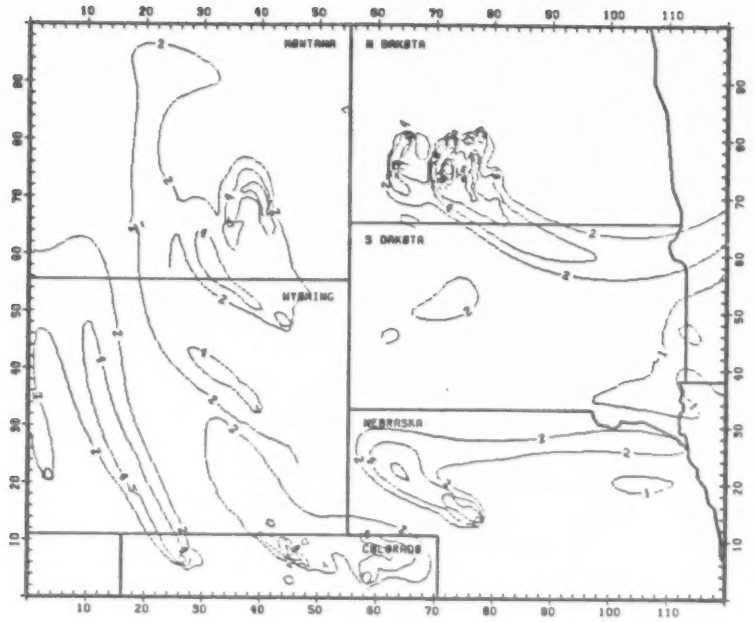

(a) SO_2

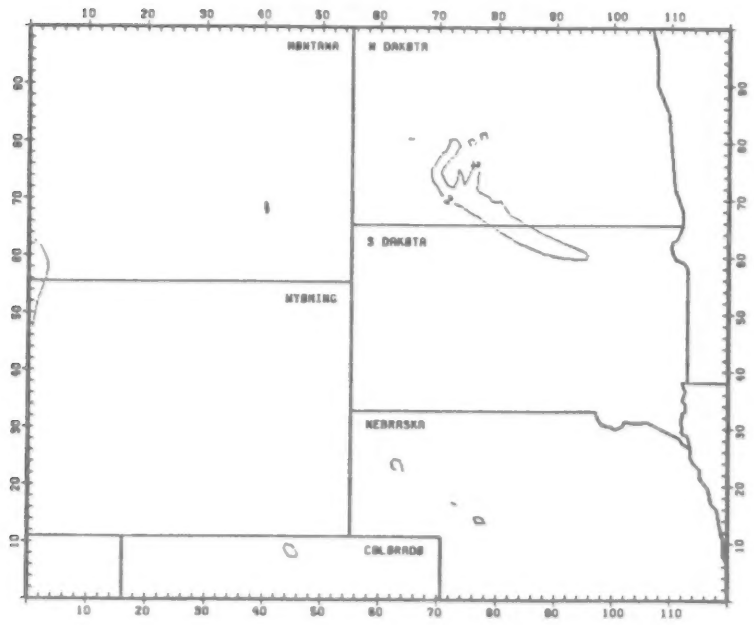

(b) SO_4

FIGURE A-9. SO_2 AND SO_4 CONCENTRATIONS FOR CASE 2: 1100 TO 1400 MST ON 5 APRIL 1976

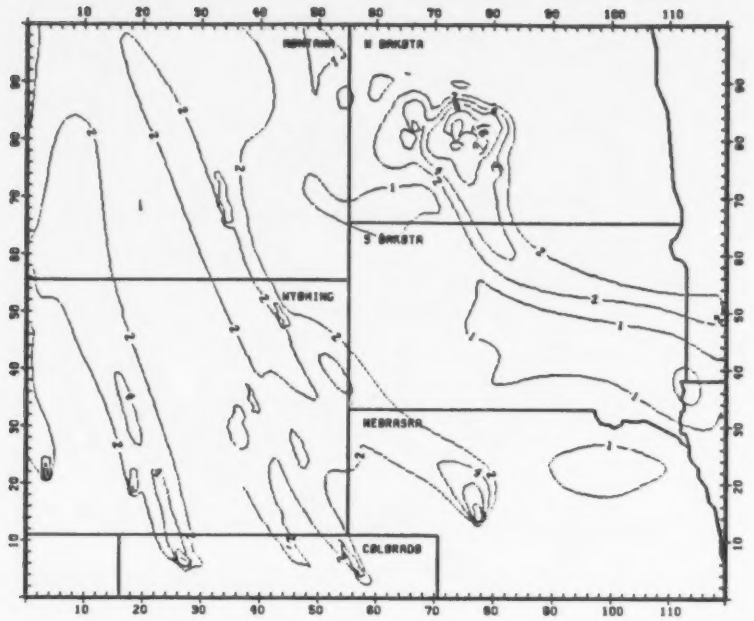

(a) SO_2

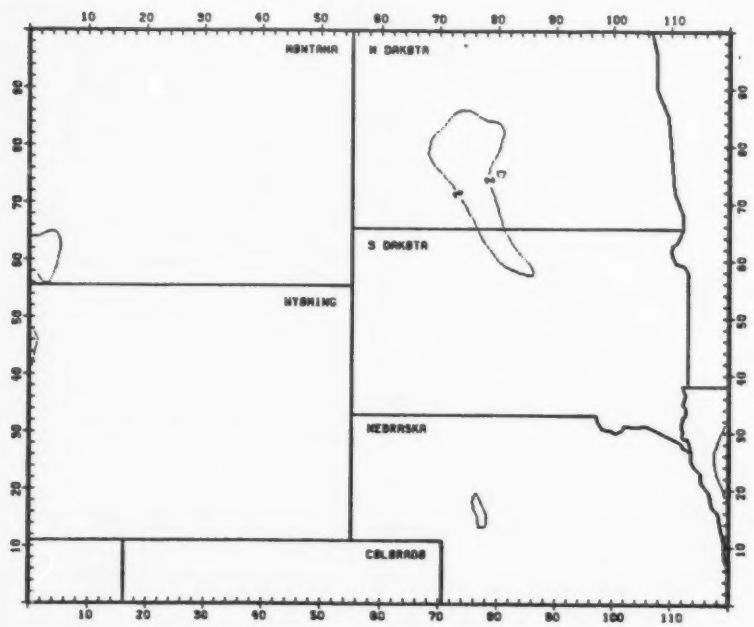

(b) SO_4

FIGURE A-10. SO_2 AND SO_4 CONCENTRATIONS FOR CASE 2: 2000 TO 2300 MST ON 5 APRIL 1976

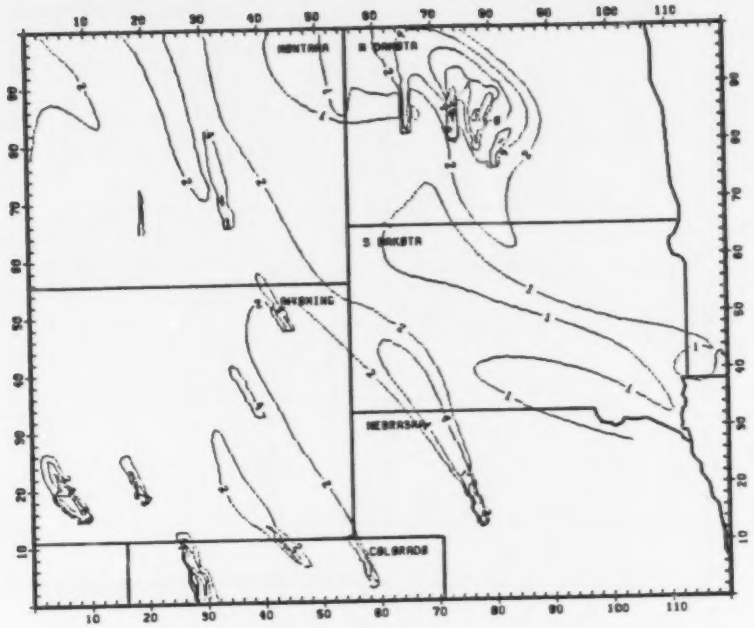

(a) SO_2

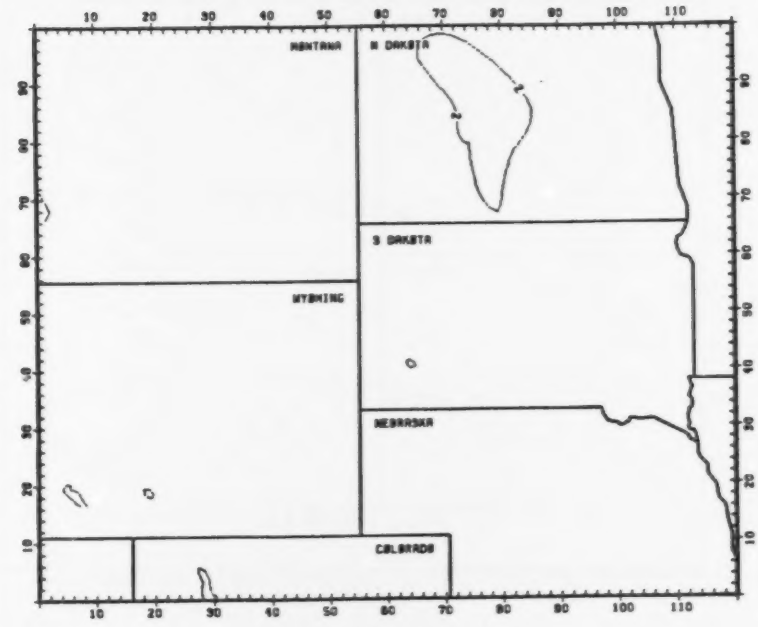

(b) SO_4

FIGURE A-11. SO_2 AND SO_4 CONCENTRATIONS FOR CASE 2: 500 TO 800 MST ON 6 APRIL 1976

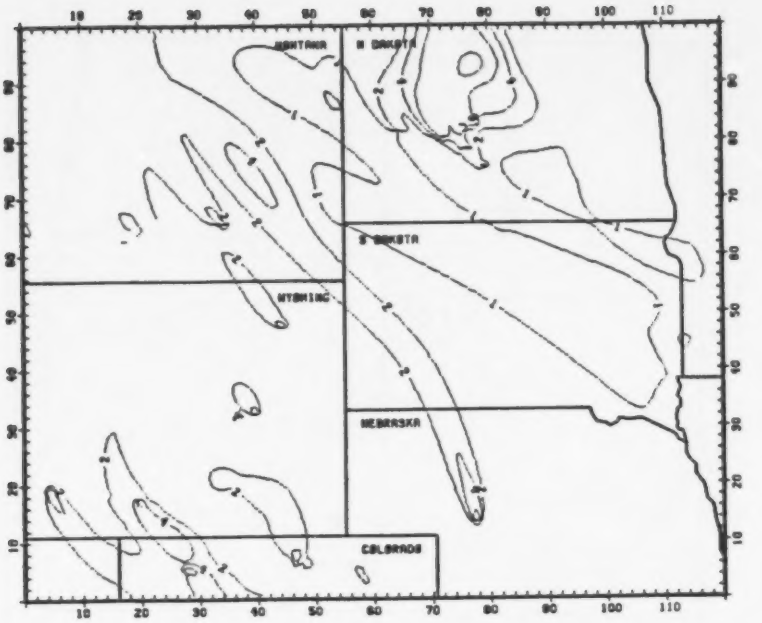

(a) SO_2

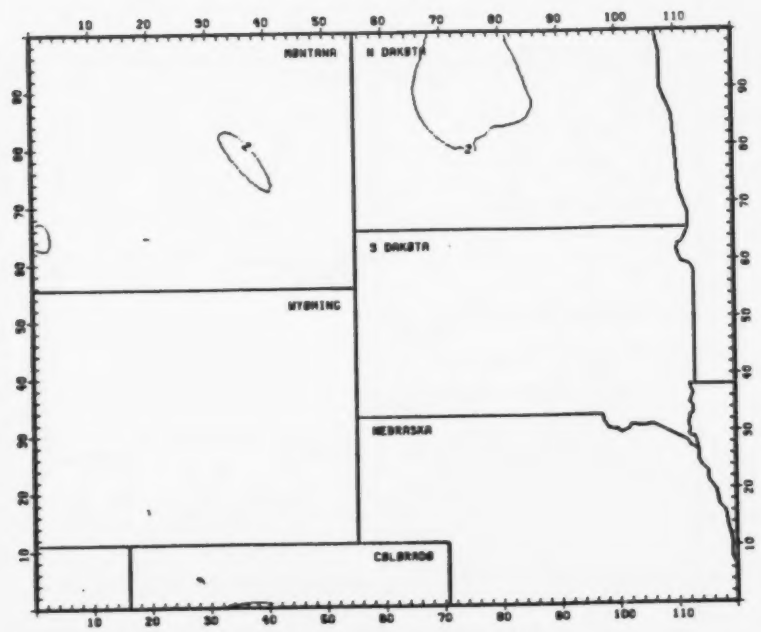

(b) SO_4

FIGURE A-12. SO_2 AND SO_4 CONCENTRATIONS FOR CASE 2: 1400 TO 1700 MST ON 6 APRIL 1976

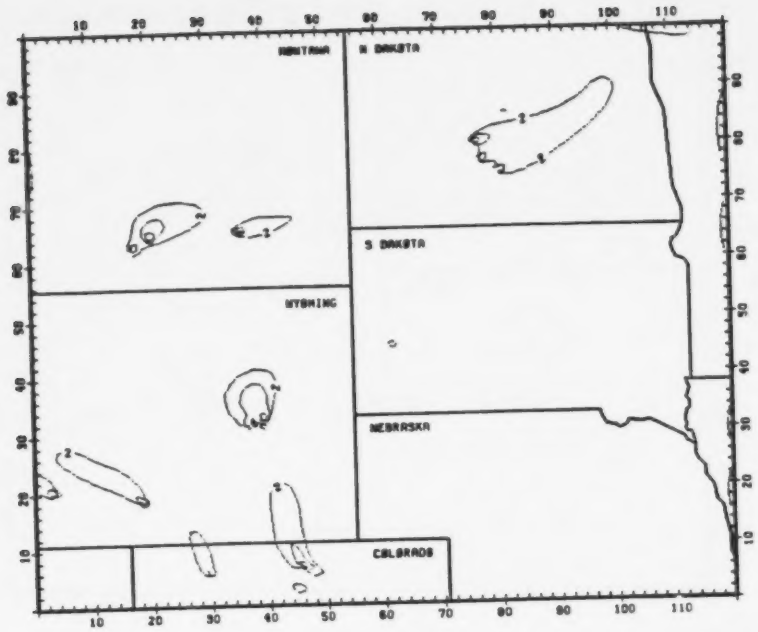

(a) SO_2

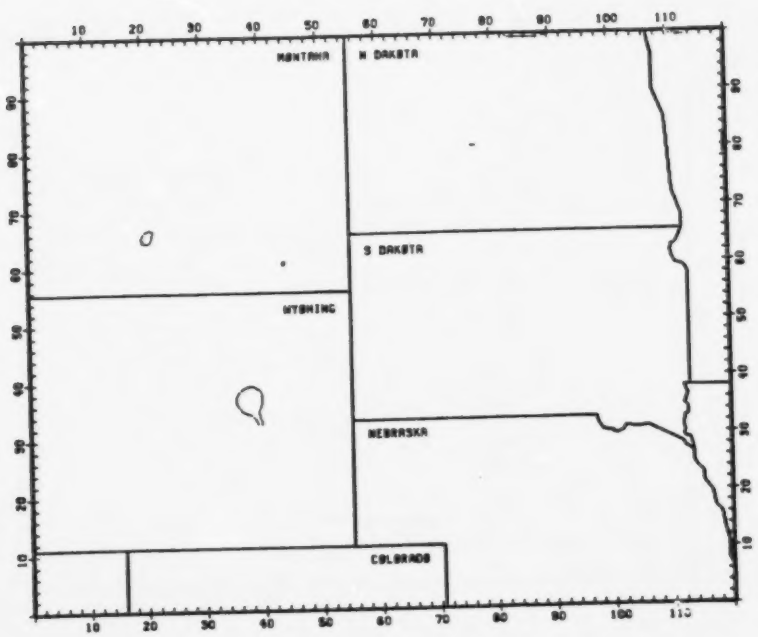

(b) SO_4

FIGURE A-13. SO_2 AND SO_4 CONCENTRATIONS FOR CASE 3: 1700 TO 2000 MST ON 4 APRIL 1976

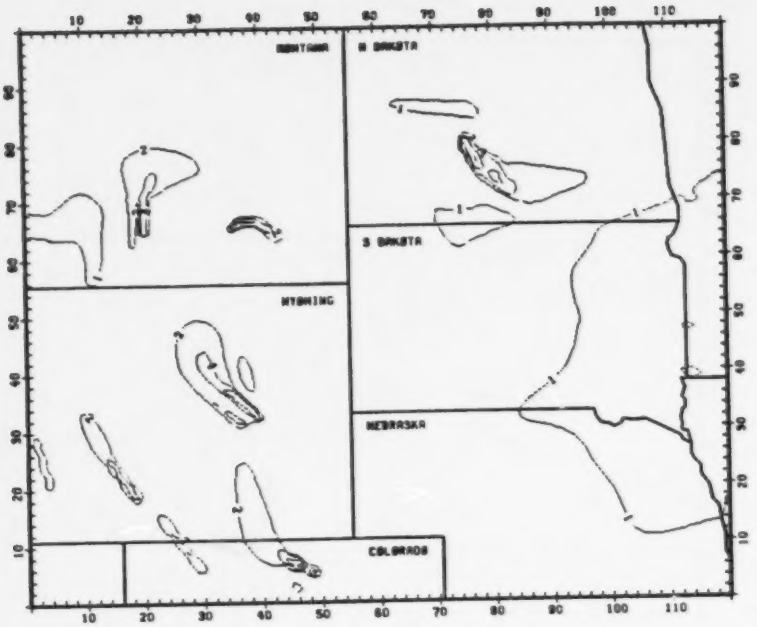

(a) SO_2

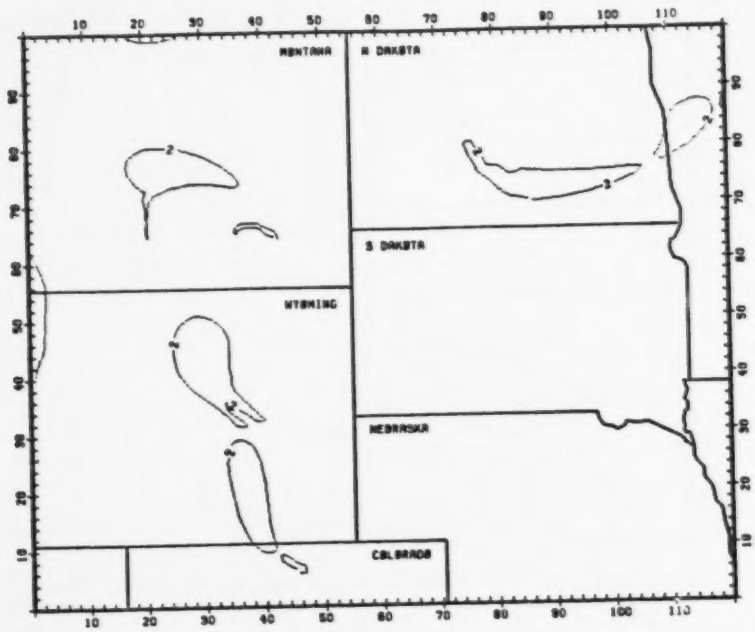

(b) SO_4

FIGURE A-14. SO_2 AND SO_4 CONCENTRATIONS FOR CASE 3: 200 TO 500 MST ON 5 APRIL 1976

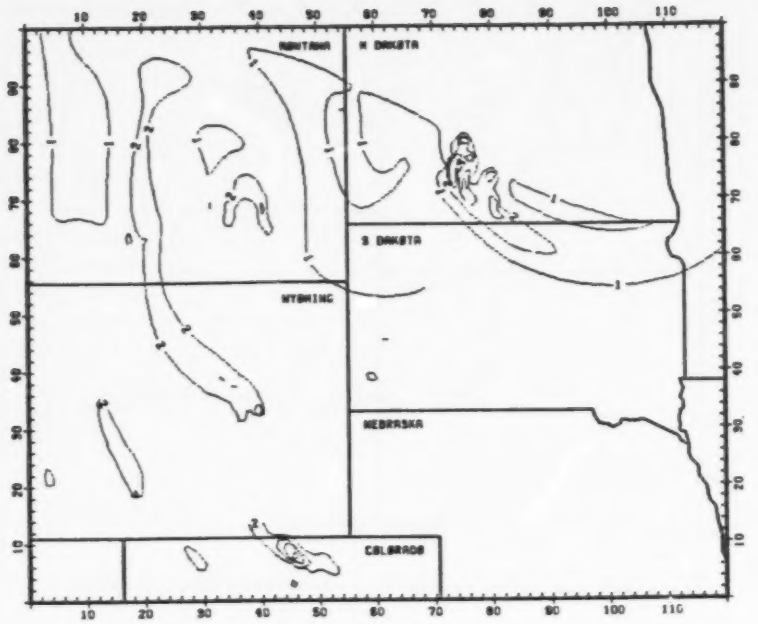

(a) SO_2

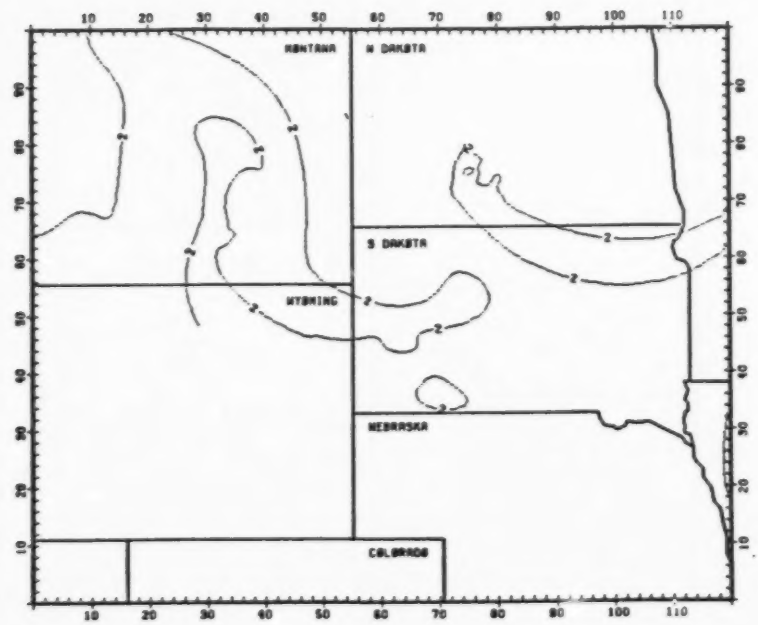

(b) SO_4

FIGURE A-15. SO_2 AND SO_4 CONCENTRATIONS FOR CASE 3: 1100 TO 1400 MST ON 5 APRIL 1976

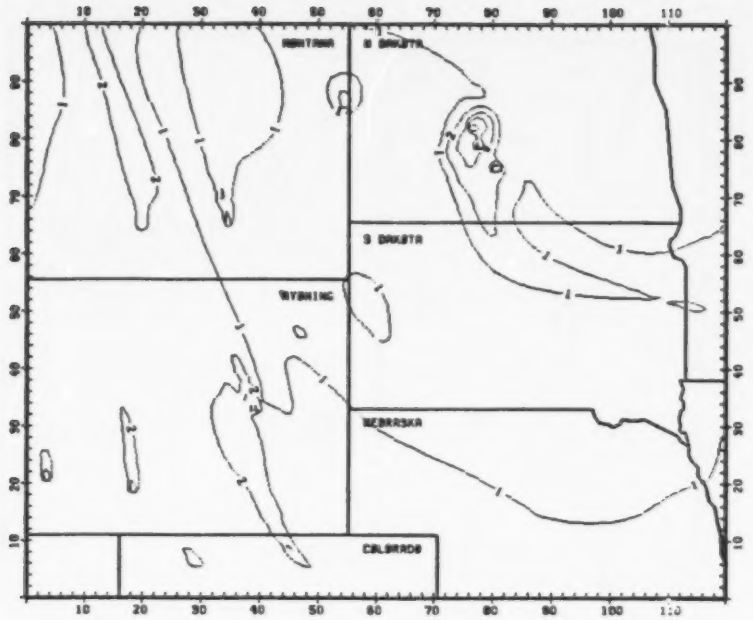

(a) SO_2

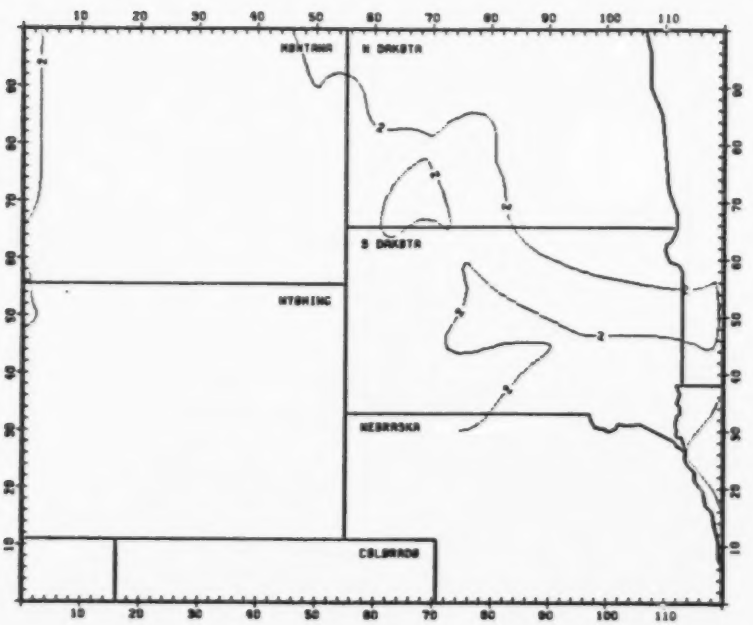

(b) SO_4

FIGURE A-16. SO_2 AND SO_4 CONCENTRATIONS FOR CASE 3: 2000 TO 2300 MST ON 5 APRIL 1976

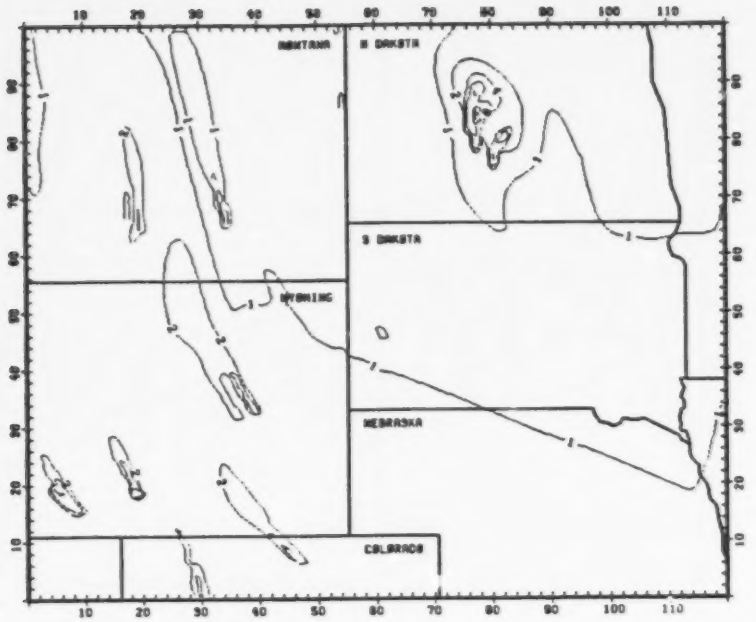

(a) SO_2

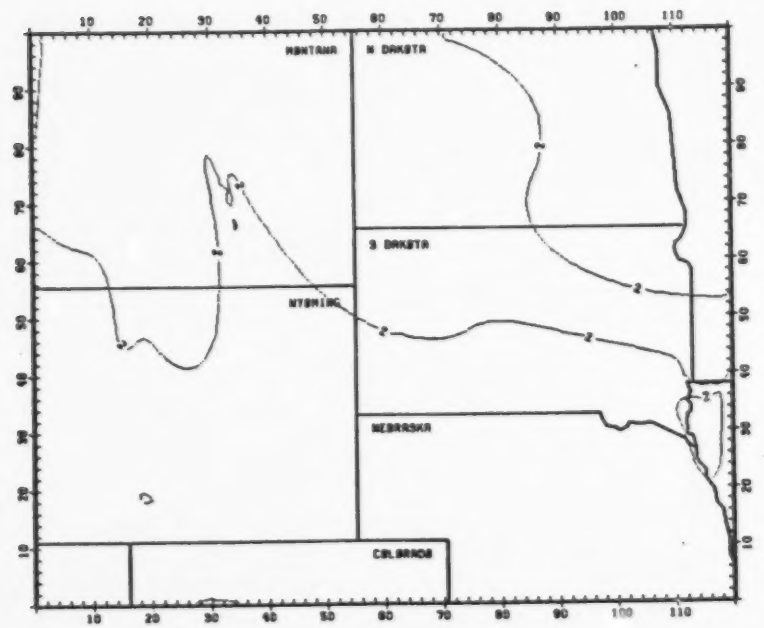

(b) SO_4

FIGURE A-17. SO_2 AND SO_4 CONCENTRATIONS FOR CASE 3: 500 TO 800 MST ON 6 APRIL 1976

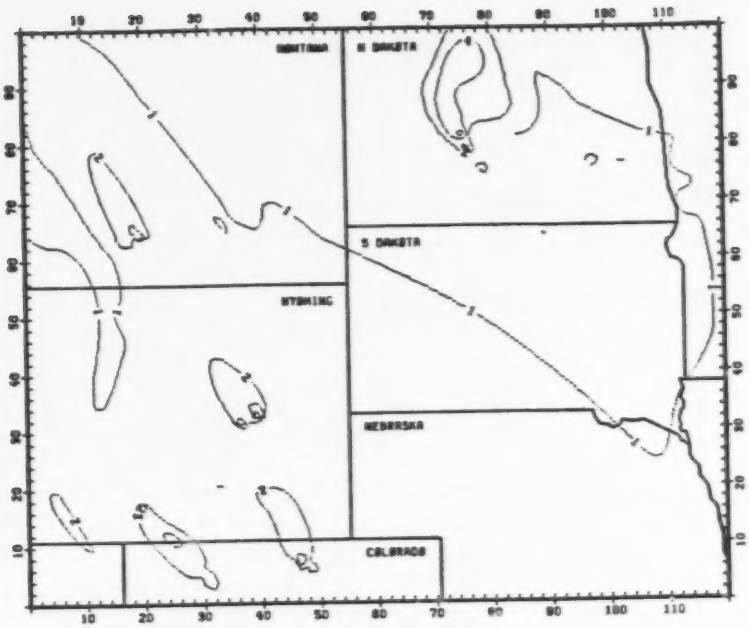

(a) SO_2

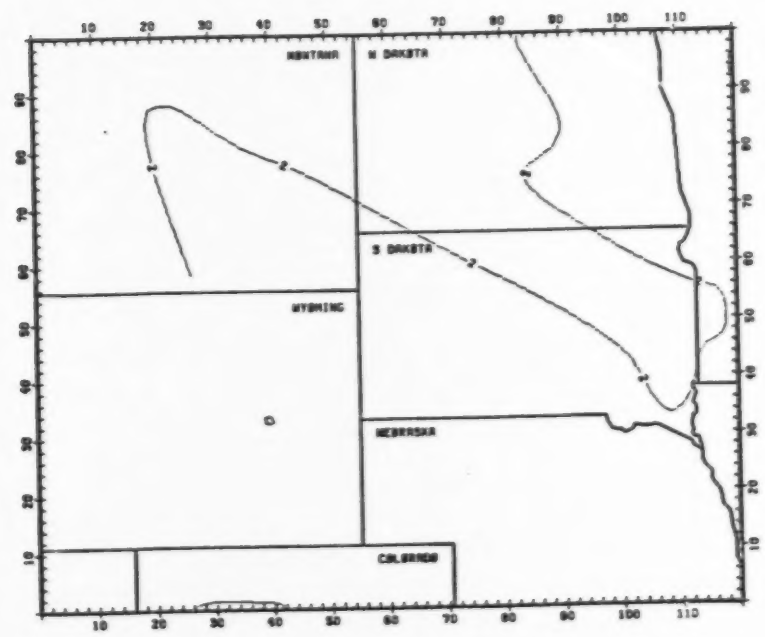

(b) SO_4

FIGURE A-18. SO_2 AND SO_4 CONCENTRATIONS FOR CASE 3: 1400 TO 1700 MST ON 6 APRIL 1976

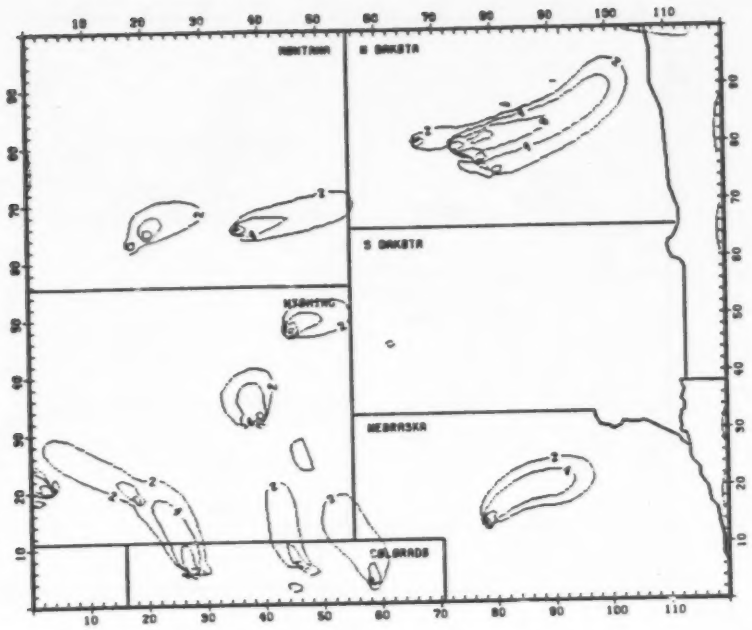

(a) SO_2

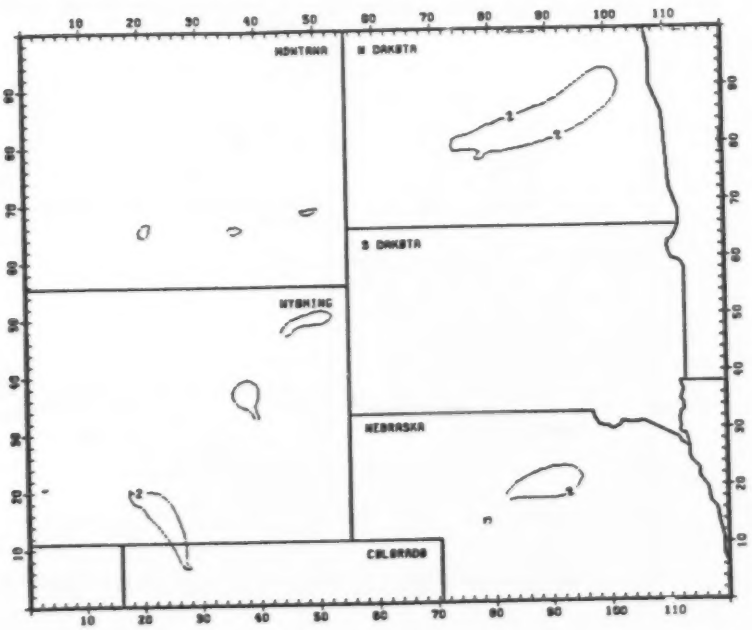

(b) SO_4

FIGURE A-19. SO_2 AND SO_4 CONCENTRATIONS FOR CASE 4: 1700 TO 2000 MST ON 4 APRIL 1976

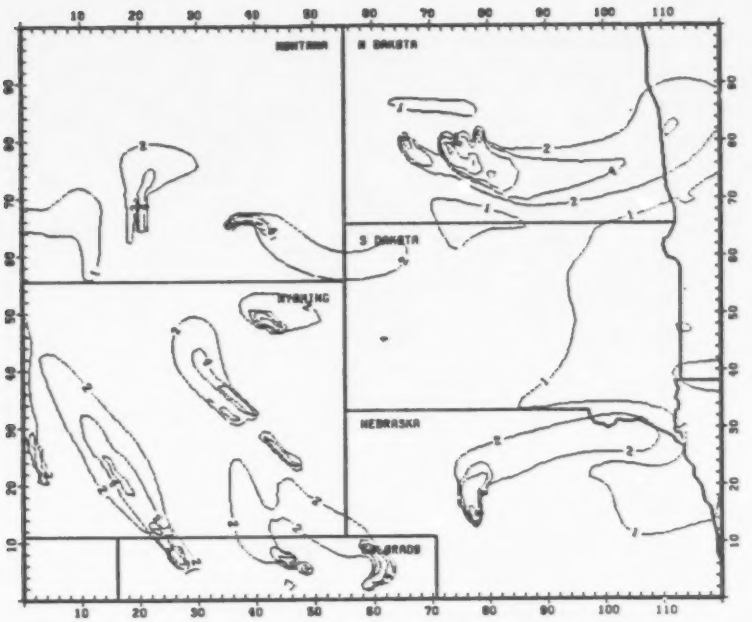

(a) SO_2

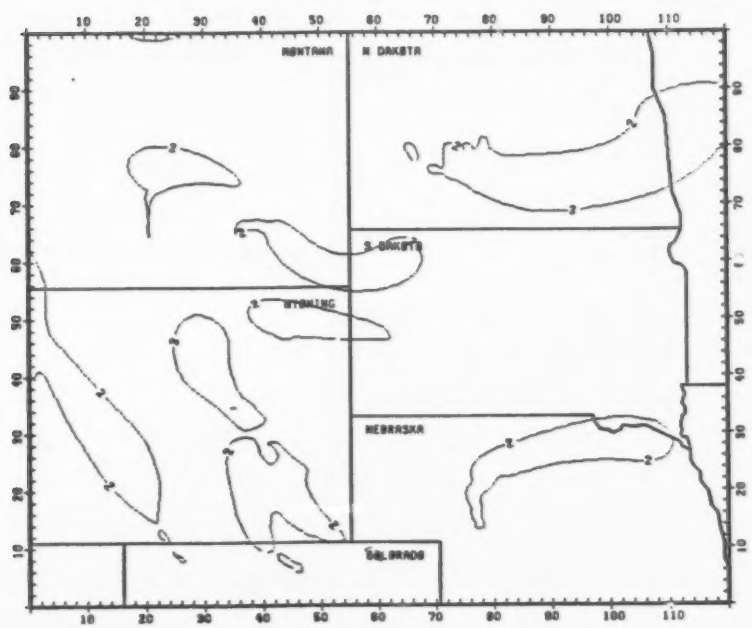

(b) SO_4

FIGURE A-20. SO_2 AND SO_4 CONCENTRATIONS FOR CASE 4: 200 TO 500 MST ON 5 APRIL 1976

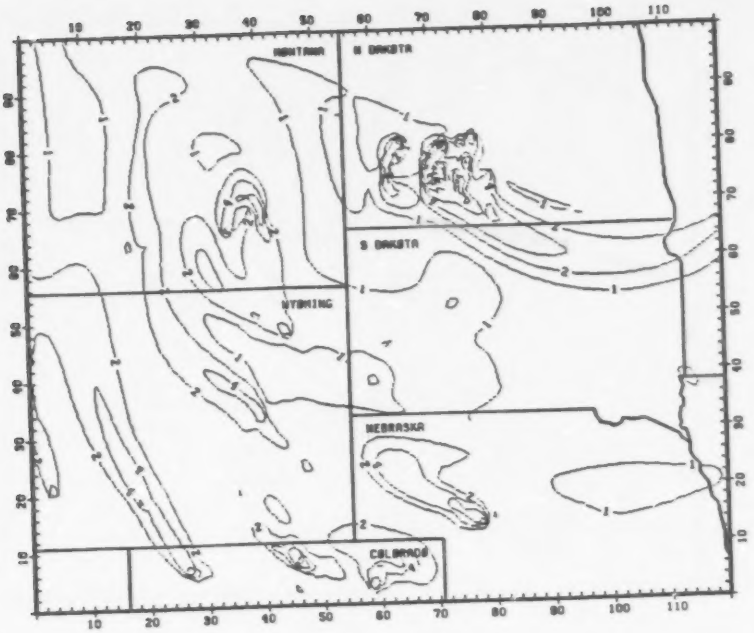

(a) SO_2

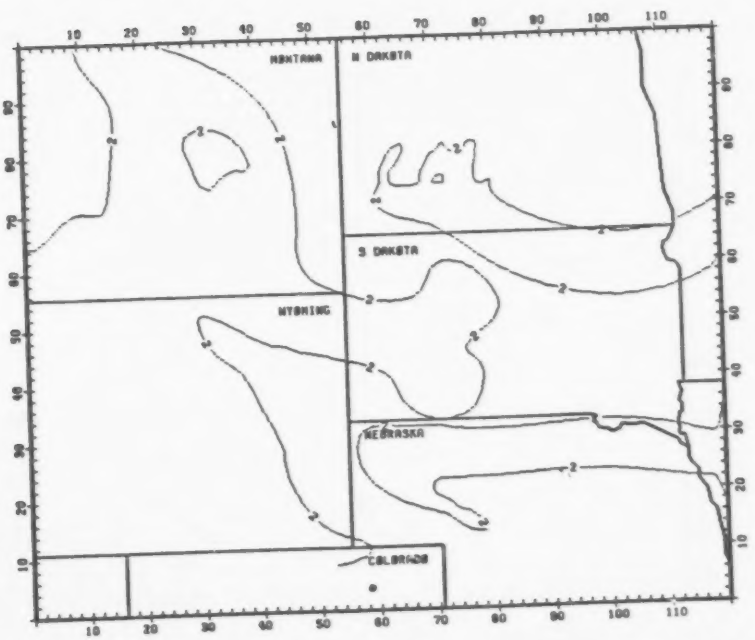

(b) SO_4

FIGURE A-21. SO_2 AND SO_4 CONCENTRATIONS FOR CASE 4: 1100 TO 1400 MST ON 5 APRIL 1976

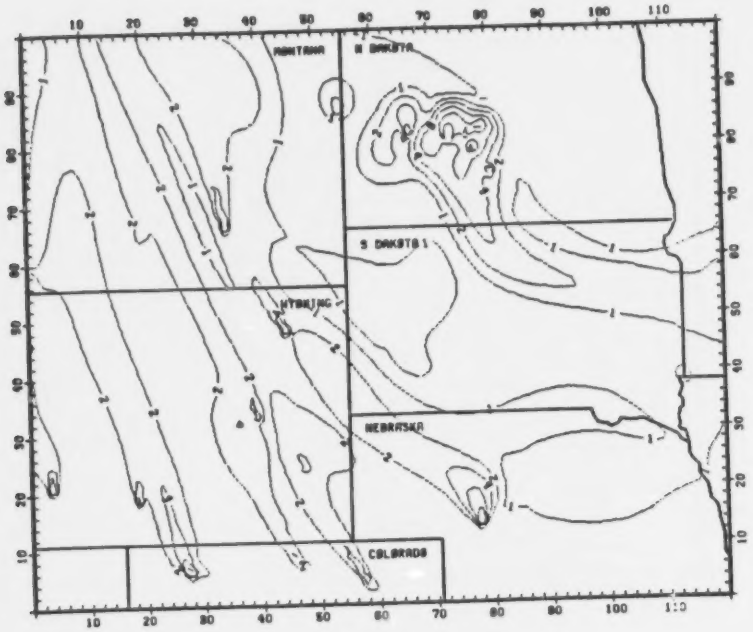

(a) SO_2

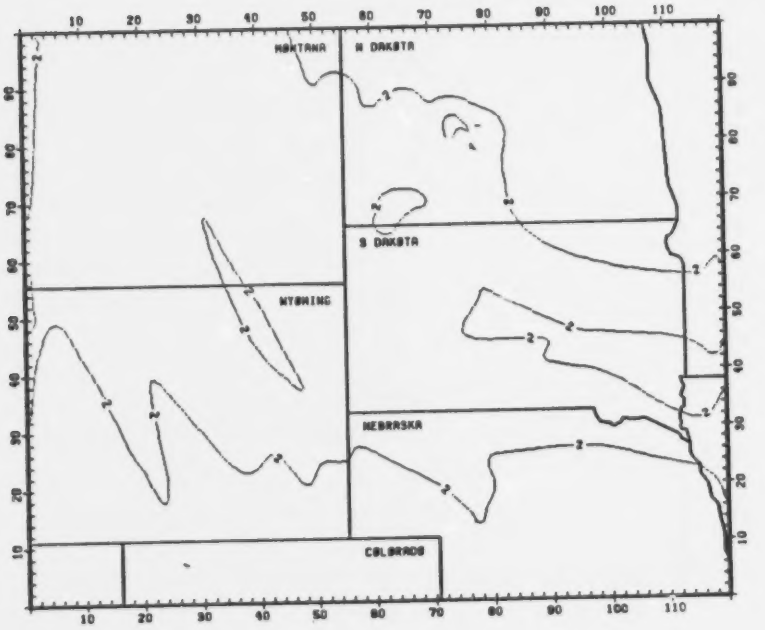

(b) SO_4

FIGURE A-22. SO_2 AND SO_4 CONCENTRATIONS FOR CASE 4: 2000 TO 2300 MST ON 5 APRIL 1976

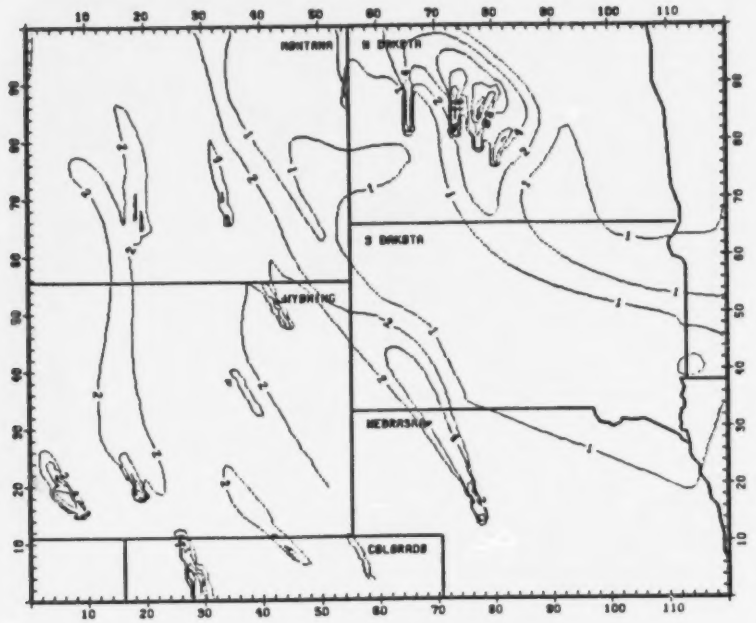

(a) SO_2

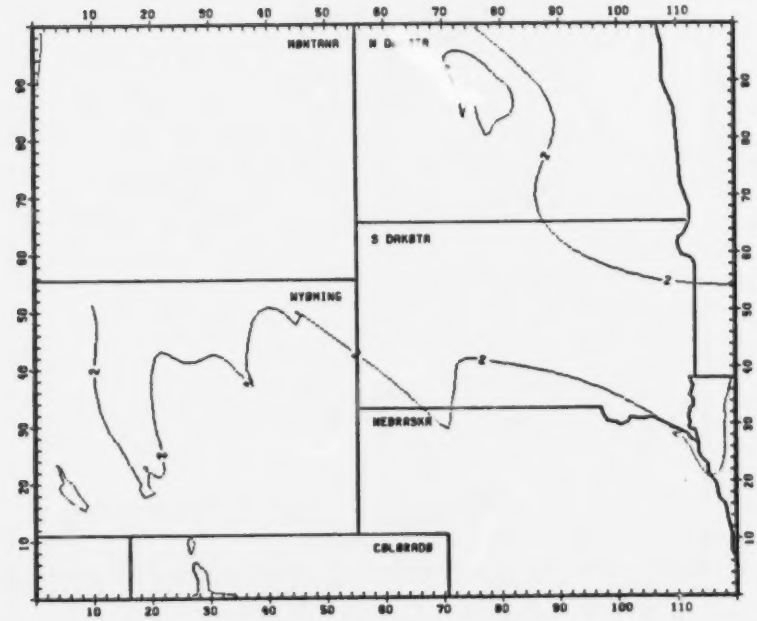

(b) SO_4

FIGURE A-23. SO_2 AND SO_4 CONCENTRATIONS FOR CASE 4: 500 TO 800 MST ON 6 APRIL 1976

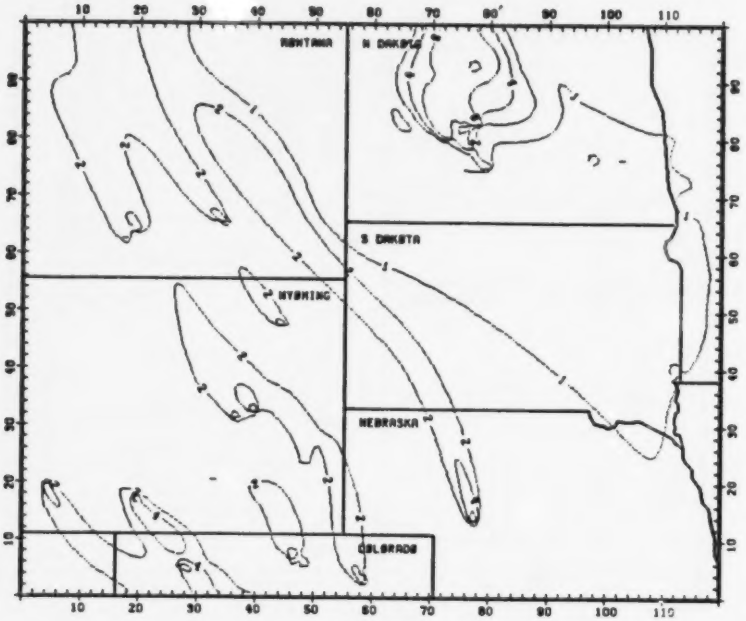

(a) SO_2

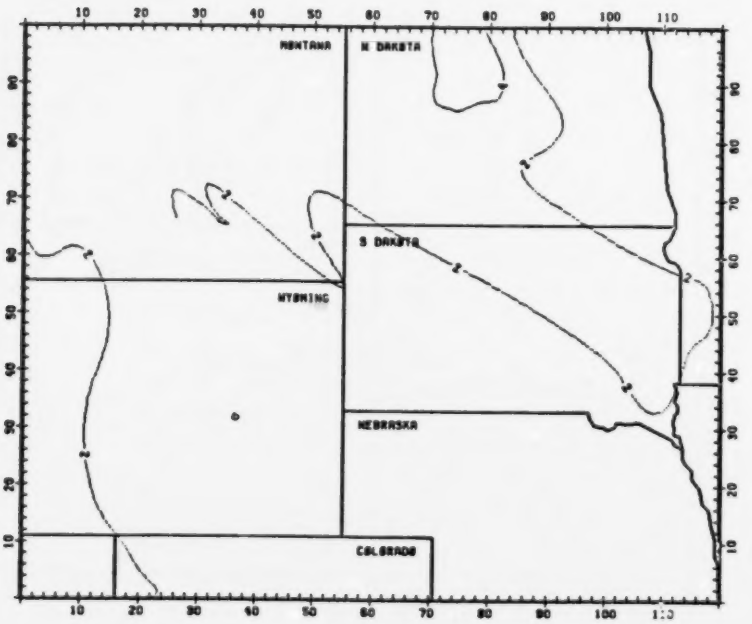

(b) SO_4

FIGURE A-24. SO_2 AND SO_4 CONCENTRATIONS FOR CASE 4: 1400 TO 1700 MST ON 6 APRIL 1976

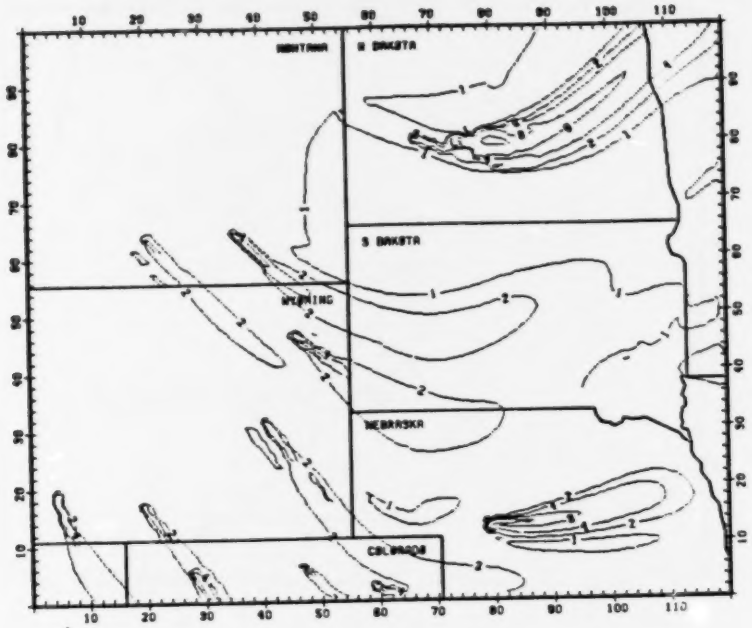

(a) SO_2

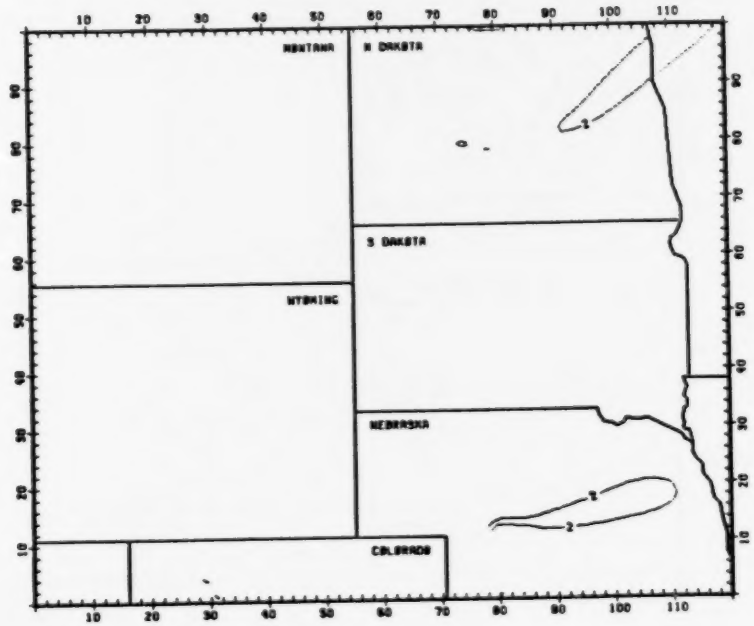

(b) SO_4

FIGURE A-25. SO_2 AND SO_4 CONCENTRATIONS FOR CASE 5: 1700 TO 2000 MST ON 27 JANUARY 1976

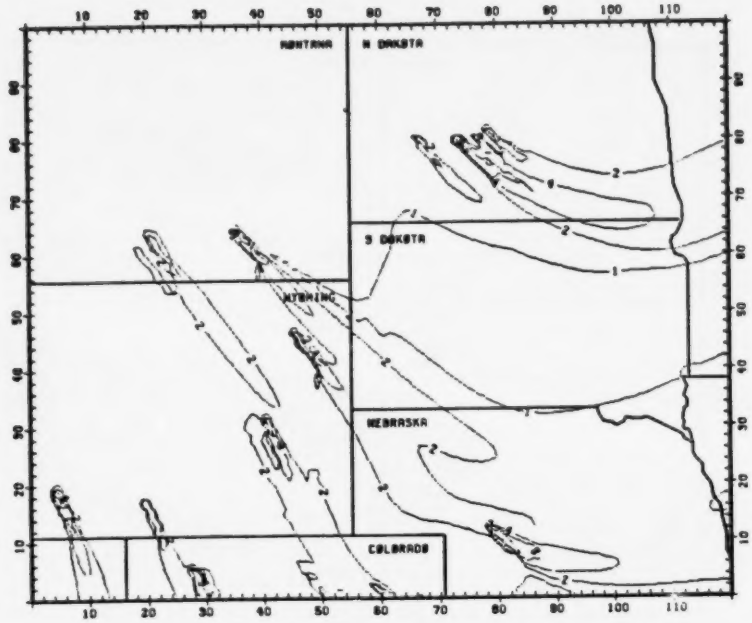

(a) SO_2

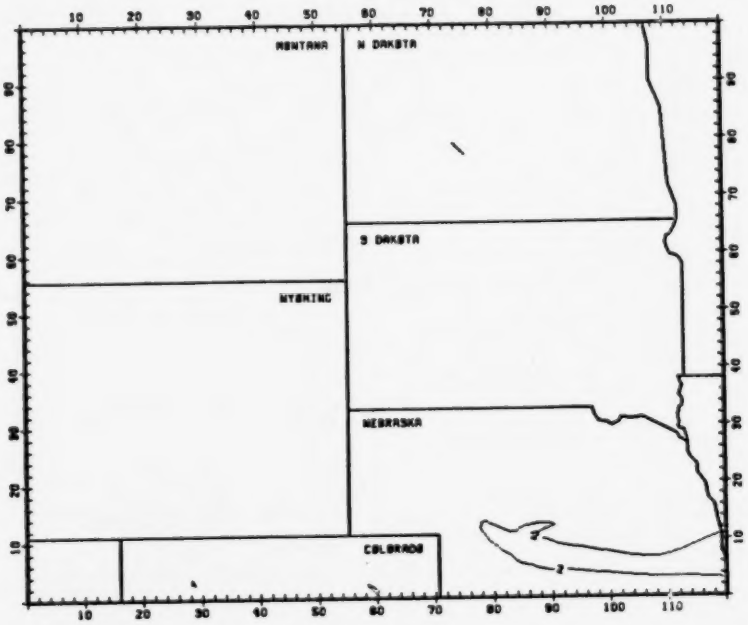

(b) SO_4

FIGURE A-26. SO_2 AND SO_4 CONCENTRATIONS FOR CASE 5: 200 TO 500 MST ON 28 JANUARY 1976

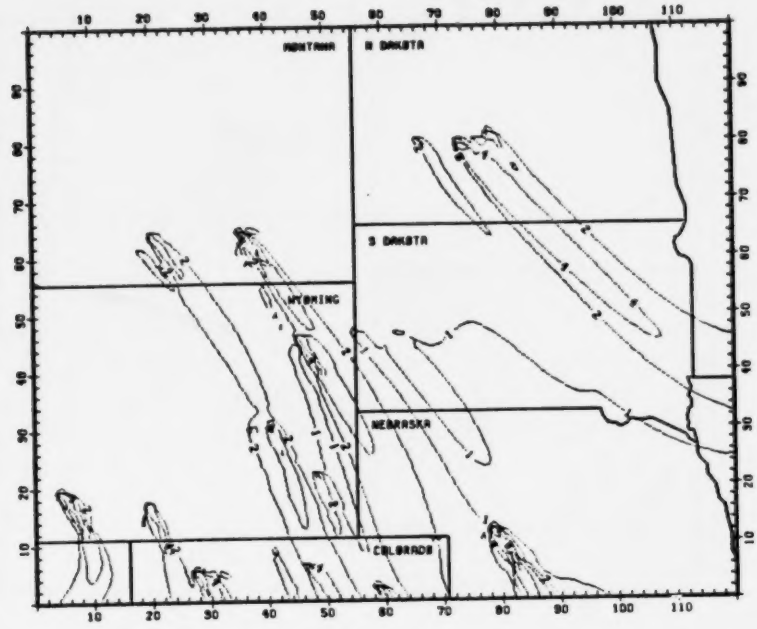

(a) SO_2

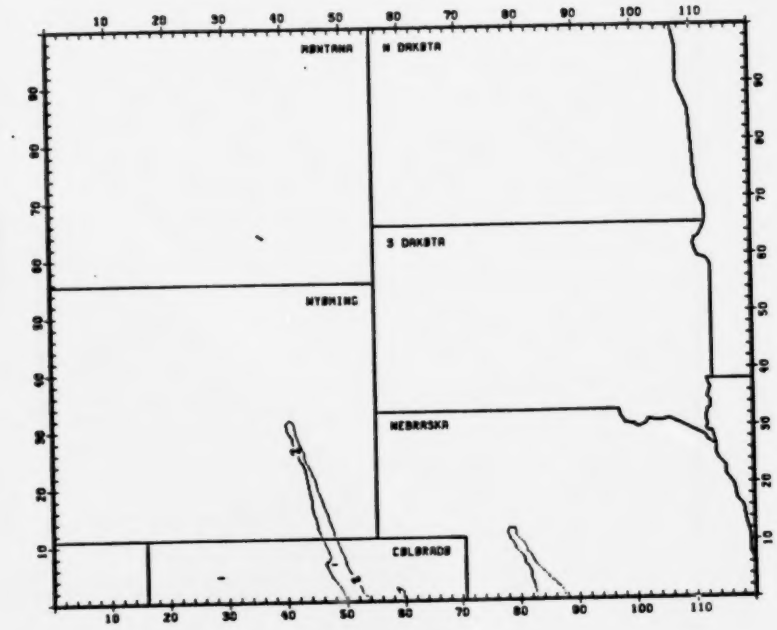

(b) SO_4

FIGURE A-27. SO_2 AND SO_4 CONCENTRATIONS FOR CASE 5: 1100 TO 1400 MST ON 28 JANUARY 1976

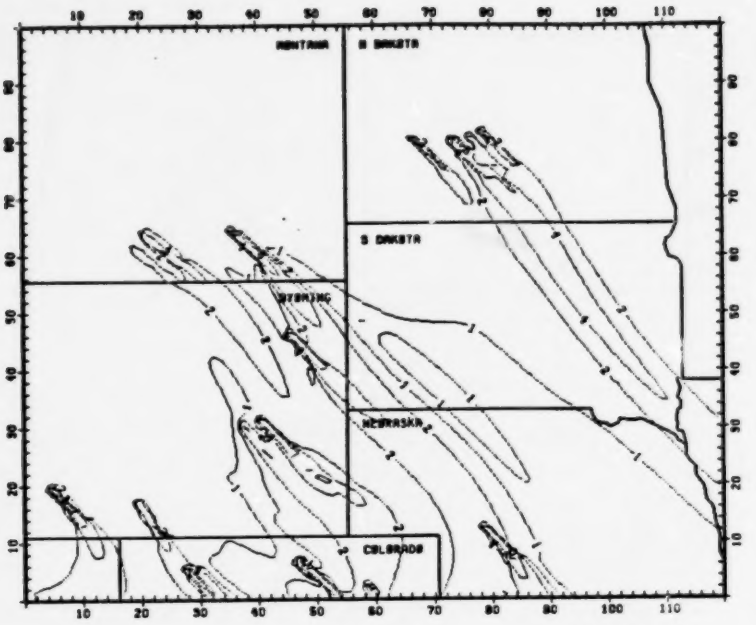

(a) SO_2

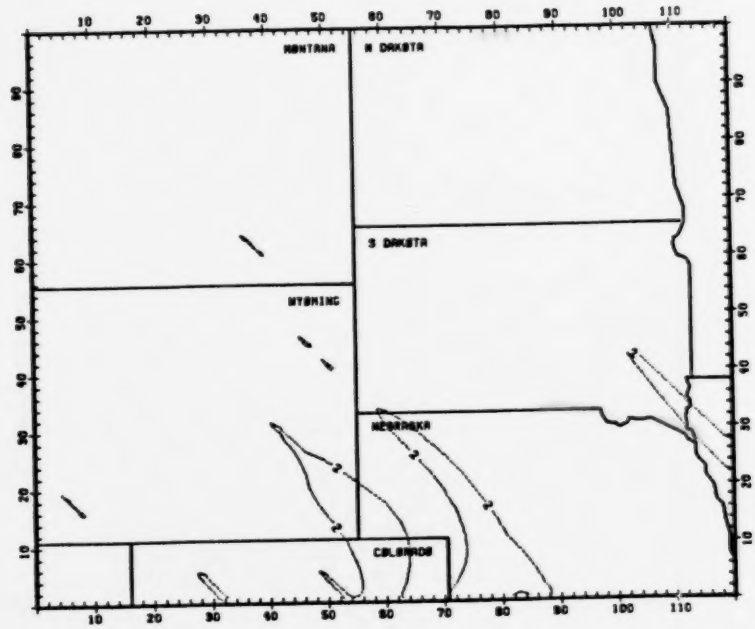

(b) SO_4

FIGURE A-28. SO_2 AND SO_4 CONCENTRATIONS FOR CASE 5: 2000 TO 2300 MST ON 28 JANUARY 1976

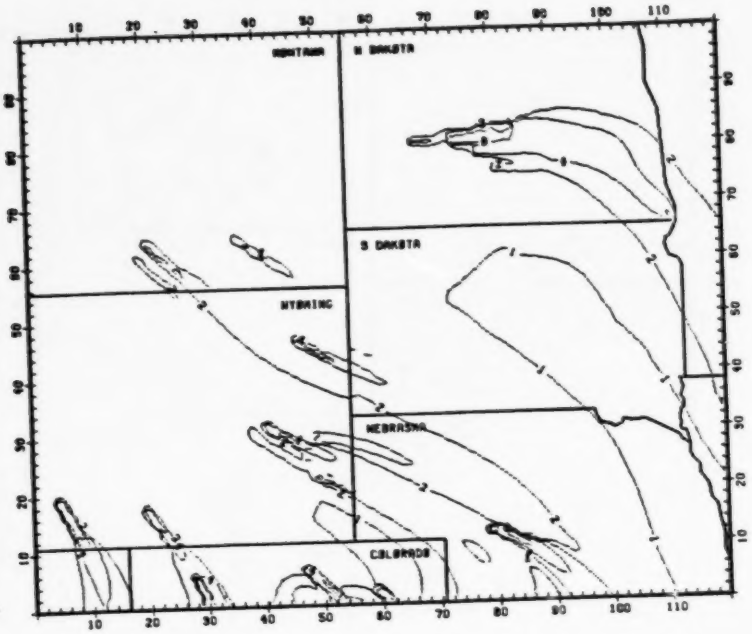

(a) SO_2

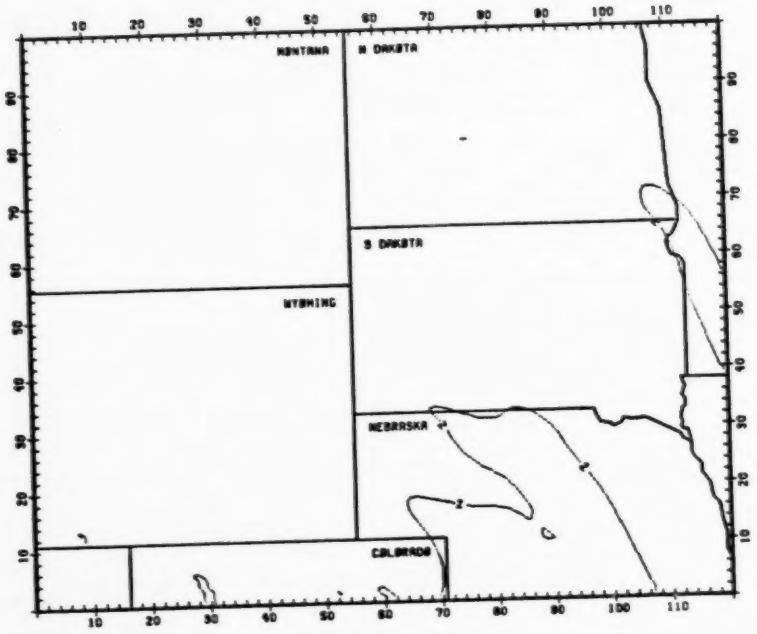

(b) SO_4

FIGURE A-29. SO_2 AND SO_4 CONCENTRATIONS FOR CASE 5: 500 TO 800 MST ON 29 JANUARY 1976

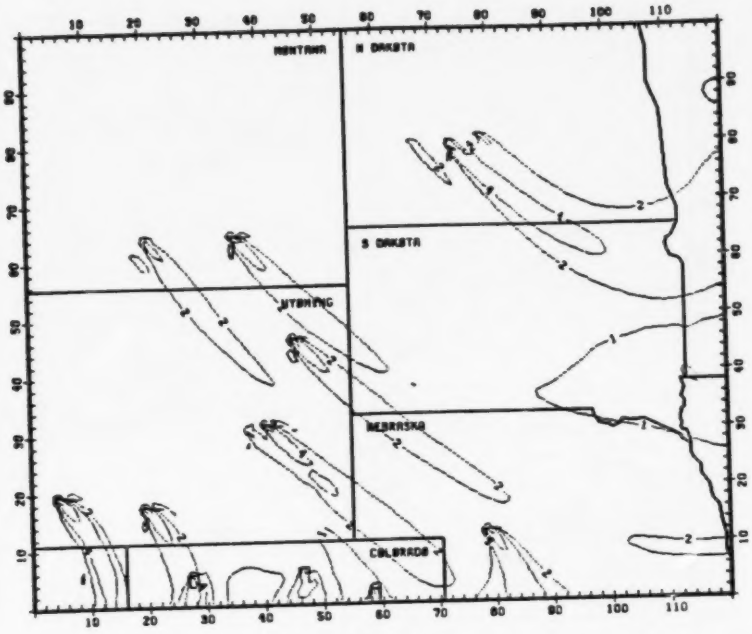

(a) SO_2

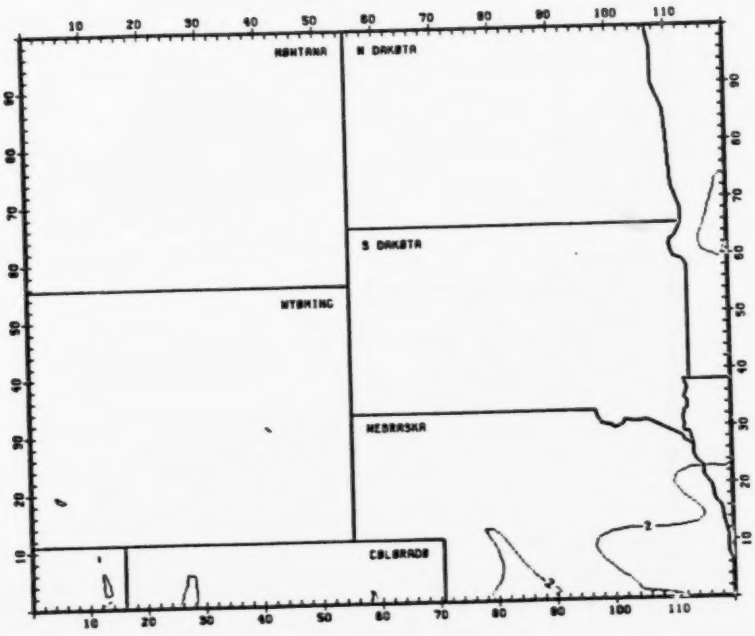

(b) SO_4

FIGURE A-30. SO_2 AND SO_4 CONCENTRATIONS FOR CASE 5: 1400 TO 1700 MST ON 29 JANUARY 1976

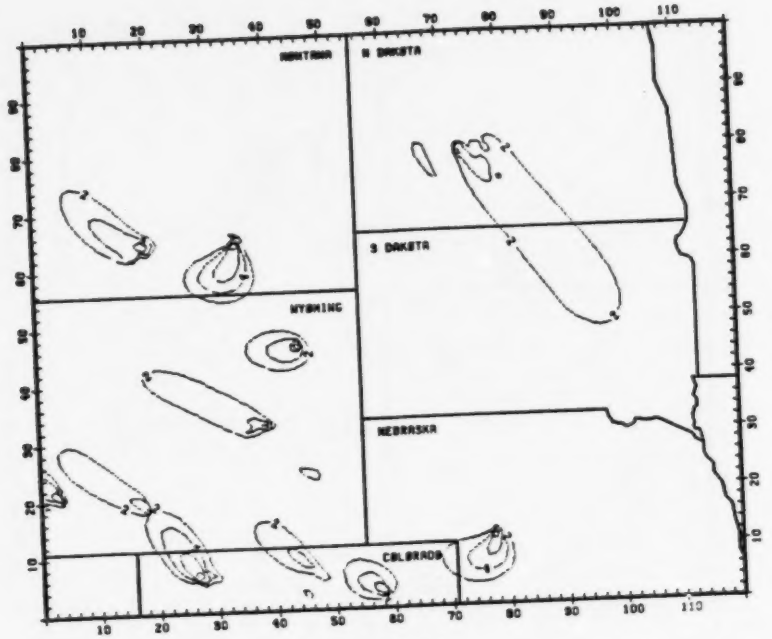

(a) SO_2

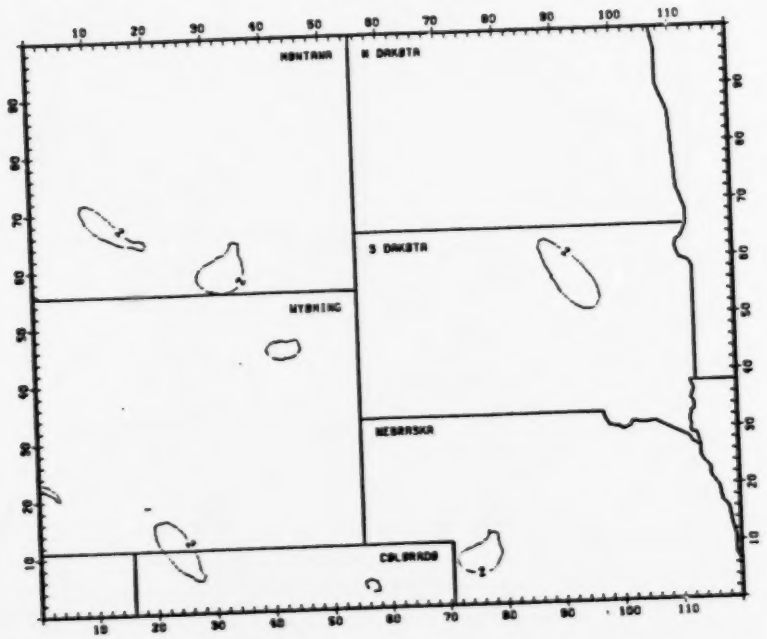

(b) SO_4

FIGURE A-31. SO_2 AND SO_4 CONCENTRATIONS FOR CASE 6: 1700 TO 2000 MST ON 9 JULY 1975

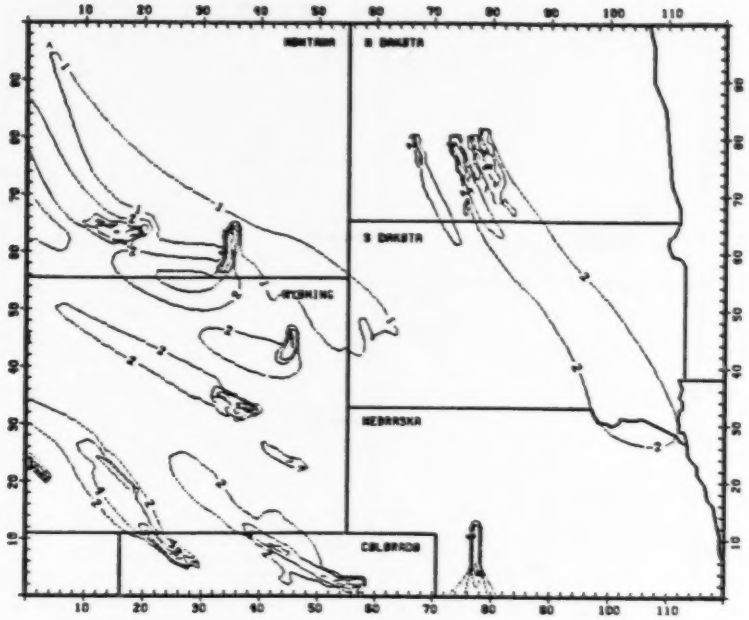

(a) SO_2

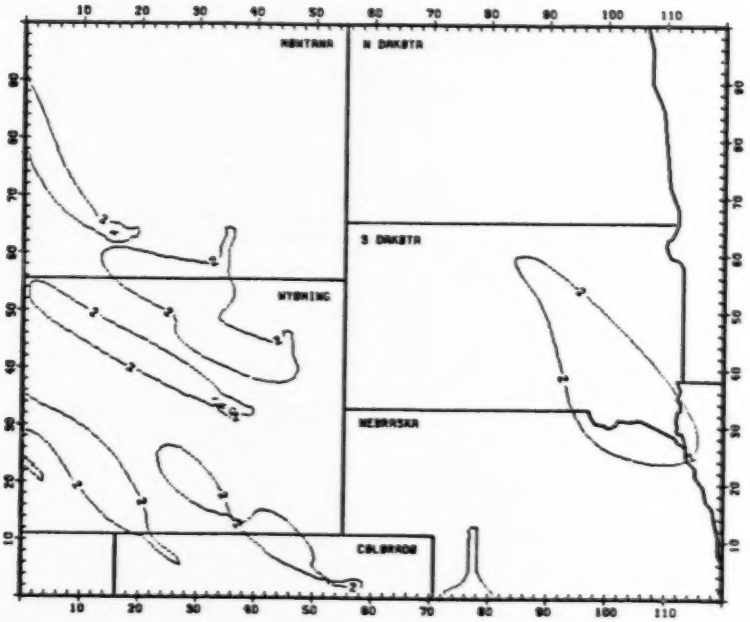

(b) SO_4

FIGURE A-32. SO_2 AND SO_4 CONCENTRATIONS FOR CASE 6: 200 TO 500 MST ON 10 JULY 1975

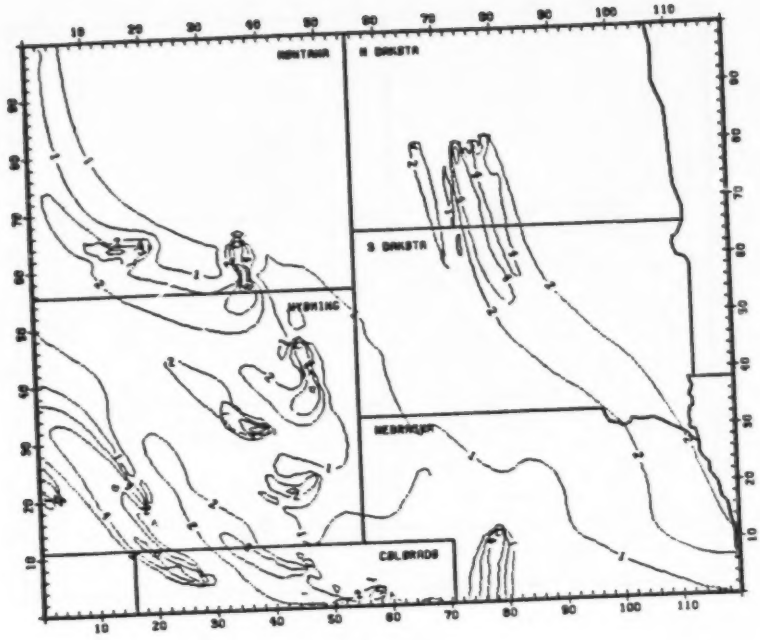

(a) SO_2

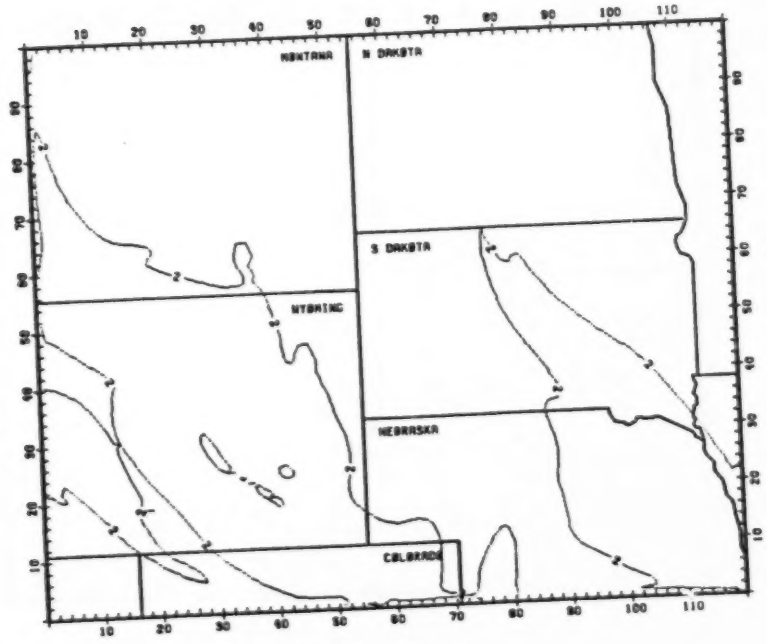

(b) SO_4

FIGURE A-33. SO_2 AND SO_4 CONCENTRATIONS FOR CASE 6: 1100 TO 1400 MST ON 10 JULY 1975

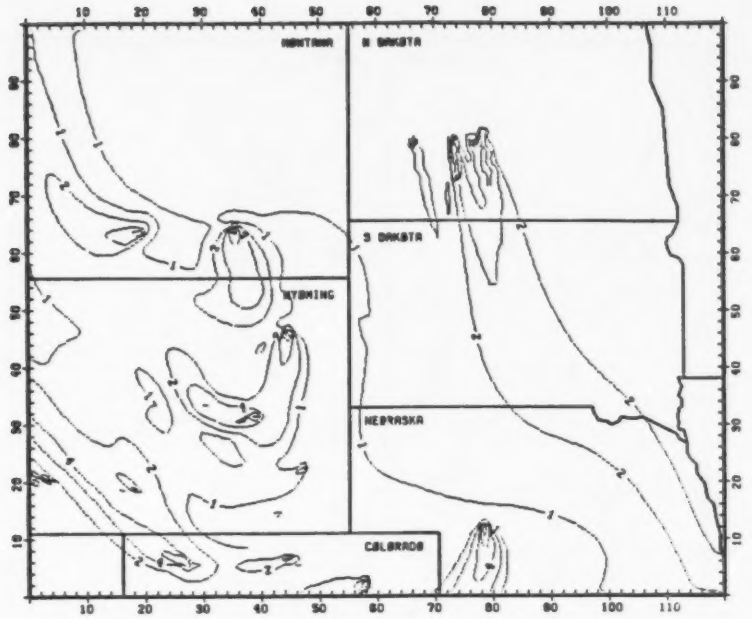

(a) SO_2

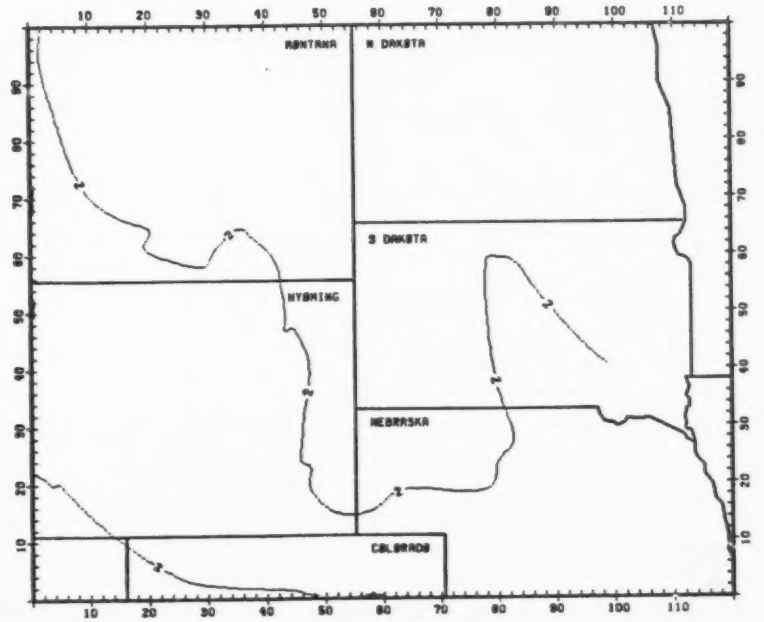

(b) SO_4

FIGURE A-34. SO_2 AND SO_4 CONCENTRATIONS FOR CASE 6: 2000 TO 2300 MST ON 10 JULY 1975

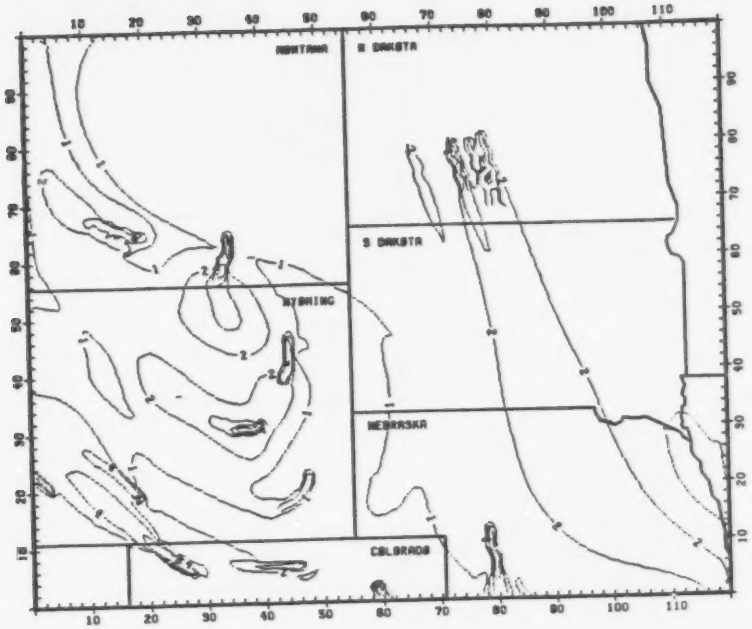

(a) SO_2

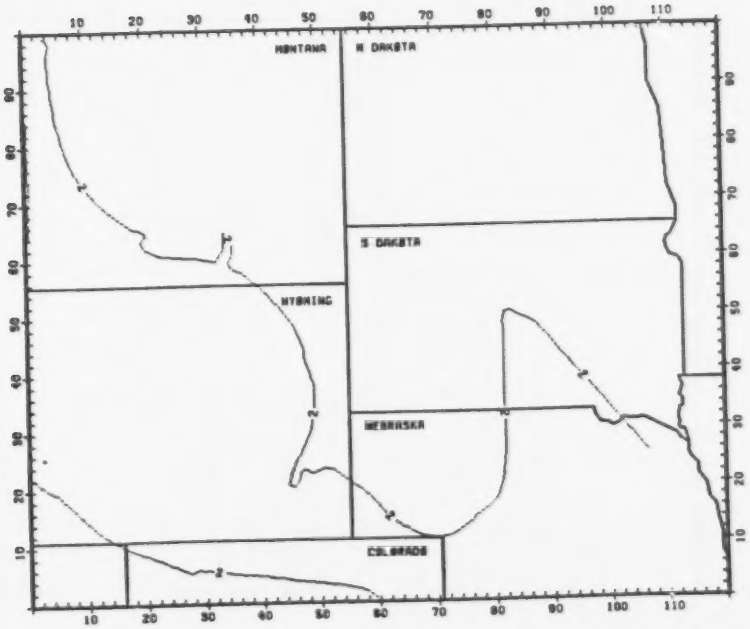

(b) SO_4

FIGURE A-35. SO_2 AND SO_4 CONCENTRATIONS FOR CASE 6: 500 TO 800 MST ON 11 JULY 1975

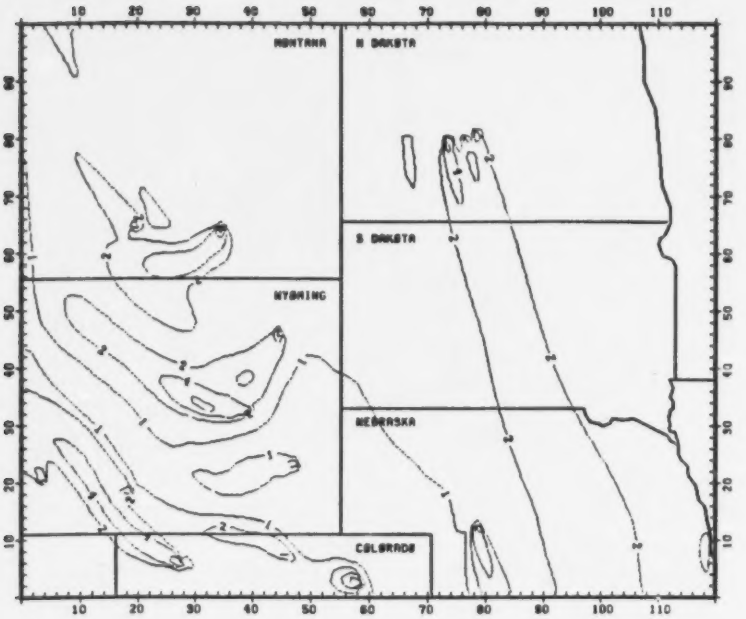

(a) SO_2

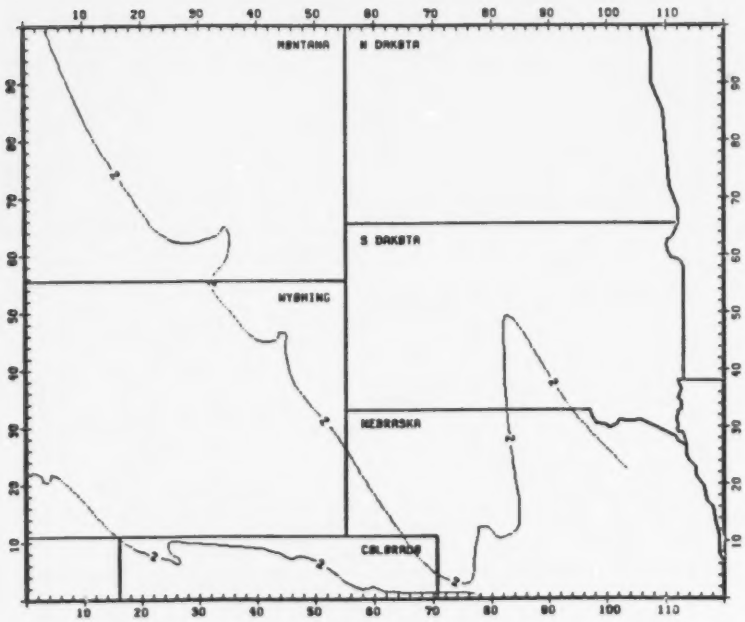

(b) SO_4

FIGURE A-36. SO_2 AND SO_4 CONCENTRATIONS FOR CASE 6: 1400 TO 1700 MST ON 11 JULY 1975

REFERENCES

Bauer, E. (1973), "Dispersion of Tracers in the Atmosphere: Survey of Meteorological Data," AD-760 694, National Technical Information Service, U.S. Department of Commerce, Washington, D.C.

Charlson, R., A. Waggoner, and J. Thielke (1979), Visibility Protection for Class I Areas: The Theoretical Basis, NTIS publication No. PB-288-842.

DeBoor, C. (1962), "Bicubic Spline Interpolation," J. Math. and Physics, Vol. 41, pp. 212-218.

Federal Register (1975), Vol. 40, No. 33, pp. 7042-7070, 18 February 1975.

_____ (1974), "Air Quality Implementation Plans--Prevention of Significant Air Quality Deterioration," Vol. 39, No. 235, Part III, pp. 42510-42517, 5 December 1974.

Gelinas, R. J., and J. J. Walton (1974), "Dynamic-Kinetic Evolution of a Single Plume of Interacting Species," J. Atmos. Sci., Vol. 31, pp. 1807-1813.

Hage, K. D., et al. (1966), "Particle Fallout and Dispersion in the Atmosphere," SC-CR-66-2031, Aerospace Nuclear Safety, Sandia Corporation, Los Alamos, New Mexico.

Harris, R. G., A. Thomasell, and J. G. Welsh (1966), "Studies of Techniques for Analysis and Prediction of Temperature in the Ocean: Part 3--Automated Analysis and Prediction," Interim Report, Travelers Research Center, Incorporated, Wethersfield, Connecticut.

Heisenberg, W. (1948), "Zur Statistischen Theorie der Turbulenz," Z. Phys., Vol. 124, p. 614.

Kao, S. K. (1968), "Relative Dispersion of Particles in a Stratified, Rotating Atmosphere," J. Atmos. Sci., Vol. 25, pp. 481-487.

Kao, S. K., and W. S. Bullock (1964), "Lagrangian and Eulerian Correlations and the Energy Spectra of Geostrophic Velocities," Quart. J. Roy. Meteorol. Soc., Vol. 90, pp. 166-174.

Kao, S. K., and A. A. Gain (1968), "Large-Scale Dispersion of Clusters of Particles in the Atmosphere," J. Atmos. Sci., Vol. 25, pp. 214-221.

Kao, S. K., and D. Henderson (1970), "Large-Scale Dispersion of Clusters of Particles in Various Flow Patterns," J. Geophys. Res., Vol. 75, pp. 3104-3113.

Liu, M. K., and D. Durran (1977), "The Development of a Regional Air Pollution Model and Its Application to the Northern Great Plains," EPA-908/1-77-001, Systems Applications, Incorporated, San Rafael, California.

Murgatroyd, R. J. (1969), "The Dispersion of Pollutants in the Free Atmosphere by the Large Scale Wind Systems," Trans. Roy. Soc. Lond. A., Vol. 265, pp. 273-294.

Randerson, D. (1972), "Temporal Changes in Horizontal Diffusion Parameters of a Single Nuclear Debris Cloud," J. Appl. Meteor., Vol. 11, pp. 670-673.

Smagorinsky, J. (1963), "General Circulation Experiments with the Primitive Equations: I. The Basic Experiment," Mon. Wea. Review, Vol. 91, pp. 99-164.

Taylor, G. I. (1921), "Diffusion by Continuous Movements," Proc. London Mathematical Society, Vol. A20, pp. 196-212.

Trijonis, J., and K. Yuan (1978), "Visibility in the Northeast: Visibility Trends and Visibility/Pollutant Relationships," Technology Service Corporation, Santa Monica, California.

van der Hoven, I. (1957), "Power Spectrum of Horizontal Wind Speed in the Frequency Range from 0.007 to 900 Cycles per Hour," J. Meteor., Vol. 14, p. 160.

Walton, J. J. (1973), "Scale-Dependent Diffusion," J. Appl. Meteor., Vol. 12, pp. 547-549.